

## ABSTRACT

SO, JU-HEE. Controlling the Shape and Interfacial Properties of Eutectic Gallium Indium.  
(Under the direction of Michael David Dickey.)

This dissertation describes the fabrication and characterization of electronic and microfluidic devices composed of a liquid metal alloy, eutectic gallium indium (EGaIn), utilizing its rheological and electrical properties. EGaIn is a low viscosity liquid at room temperature with metallic conductivity. The metal forms a surface oxide skin under ambient conditions. This oxide skin allows the metal to maintain shapes that would normally be energetically unfavorable due to surface tension. The chapters of this thesis describe new approaches to study and utilize this skin to shape the metal, control its interfacial electronic properties, and integrate the metal into new types of electronics that are soft or stretchable. We fabricated and characterized fluidic dipole and patch antennas that consist of the liquid metal injected into microfluidic channels comprising a silicone elastomer. The resonant frequency can be tuned by reconfiguring the shape of the antenna mechanically without any hysteresis; the antennas are therefore sensors of strain. We also present the fabrication and characterization of highly stretchable and electrically conductive fibers. The fibers consist of the liquid metal injected into stretchable hollow fibers composed of styrene ethylene-butylene styrene (SEBS) resin. Mechanical measurements prove that the liquid core has negligible impact on the mechanical properties of the fibers. The electrical measurements show the fibers maintain metallic conductivity up to nearly 1000% strain, which may be useful for stretchable wires or electronics integrated into clothing. We describe a new class of memristors composed entirely of soft, liquid-based materials formed by combining the liquid metal and hydrogel doped with polyelectrolytes. The oxide skin of the metal is a wide band-gap semiconductor

and the electrical resistance depends on its thickness, which can be controlled using electrical bias and/or pH of the gel which interfaces with the liquid electrodes. The direction and the magnitude of the electric bias pre-applied to the electrodes controls the anisotropy of current conductance. The pre-programmed anisotropy is preserved for more than three hours, which enables the fabrication of memory storage devices (i.e., memristors). The mechanical stability of the liquid metal enables fabrication of microelectrodes for integrated microfluidic devices. The metal can be injected into microfluidic channels in a single fabrication step to produce structures that are self-aligned with adjacent microfluidic channels. The liquid metal microelectrodes also span from the bottom to the top of the channel, and can thus generate an effective electric field in micro-electro systems. We utilized a thin oxide skin of the liquid metal to develop a new method to pattern the liquid into three dimensional free standing microstructures in spite of the destabilizing effects of surface tension. Extruding the liquid metal through a capillary or removing molds after injection of the metal into microchannels produced free standing liquid microstructures. Lastly, we analyzed the rheological properties of the liquid metal with the oxide skin in different chemical environments by using a rheometer with a parallel plate geometry. The results suggest that certain environments (water, acid) weaken the oxide corresponding with changes in the modulus and the yield stress.

© Copyright 2012 by Ju-Hee So

All Rights Reserved

Controlling the Shape and Interfacial Properties of Eutectic Gallium Indium

by  
Ju-Hee So

A dissertation submitted to the Graduate Faculty of  
North Carolina State University  
in partial fulfillment of the  
requirements for the degree of  
Doctor of Philosophy

Chemical Engineering

Raleigh, North Carolina

2012

APPROVED BY:

---

Michael D. Dickey  
Chair of Advisory Committee

---

Orlin D. Velev

---

Saad Khan

---

John F. Muth

---

Veena Misra

## **DEDICATION**

This thesis is dedicated to my family for their lifelong support and encouragement.

## **BIOGRAPHY**

Ju-Hee So was born to Jongsik So and Sunhee Kim in Seoul, Korea and she grew up with her older brother, Youngmin. After graduating from high school, she got her bachelor and master degree in Chemical and Biomolecular Engineering at Seoul National University. After working at Korea Institute of Science and Technology for one and half years, she decided to pursue her doctoral degree at North Carolina State University in Raleigh, NC, USA. Under the guidance of Michael D. Dickey, she pursued research on microfabrication, electronic and microfluidic applications of liquid metal alloys, surface chemistry and rheology.

## ACKNOWLEDGEMENTS

First, I acknowledge my advisor Prof. Michael D. Dickey. I am thankful for all of the great discussions, encouragement, advice and trust in me. I cannot dream of a better advisor. To the Dickey research group members, thank you for your support throughout this epic journey, I can only hope that I contributed as much to your careers as you did to mine. I would like to thank Dr. Velev, Dr. Lazzi, Dr. Pourdeyhimi, Dr. Muth, Hyung-Jun, Rashed, Jacob, Gerry, Amit, Sharvil, Shu and Collin for their hard work on the collaborated projects. Dr. Khan and Dr. Parsons were generous enough to allow for me to use instruments in their lab. I really appreciate their help. Thanks to Dr. Velev, Dr. Khan, Dr. Muth and Dr. Misra for serving as my committee members. Thanks to the staff in the Chemical and Biomolecular Engineering Department. You helped me navigate smoothly the road through the department.

I am deeply thankful for the time with my Korean friends at NC state university. It has always been joyful and fun to get together with them and their support helped me to get over hard times. I will remember the times we shared by traveling together, going picnics, having parties, playing tennis and games, and having lunch with small talks.

I would like to acknowledge my parents and parents in law whose sacrifices, teachings, and counsel made this achievement possible. Thank you for all you have done. Thanks to my lovely daughter Minseo. Life with you has been amazing happiness and full of unforgettable moments that will remain with me forever. My deepest gratitude is for my husband Hyung-Jun. You have been my partner throughout this journey and your support and love are a big part of this achievement.

# TABLE OF CONTENTS

<b>List of Tables .....</b>	<b>viii</b>
<b>List of Figures.....</b>	<b>ix</b>
<b>Chapter 1. Introduction .....</b>	<b>1</b>
1.1 General Information on Low Melting Temperature Metals and their Applications .....	2
1.2 Properties of Eutectic Gallium Indium .....	13
1.3 Surface Oxide of Eutectic Gallium Indium .....	14
1.4 Eutectic Gallium Indium on the Micro-scale .....	17
1.5 Motivation and Layout of this Dissertation .....	20
1.6 References .....	24
<b>Chapter 2. Reversibly Deformable and Mechanically Tunable Fluidic Antennas ....</b>	<b>30</b>
2.1 Introduction .....	31
2.2 Background .....	32
2.3 Experimental Design .....	34
2.4 Fabrication and Characterization of Dipole Antennas .....	36
2.5 Fabrication and Characterization of Microstrip Patch Antennas .....	43
2.6 Advantages of Fluidic Antennas .....	46
2.7 Limitations .....	47
2.8 Conclusions .....	47
2.9 References .....	49
<b>Chapter 3. Ultrastretchable Fibers with Metallic Conductivity Using a Liquid Metal Alloy Core .....</b>	<b>52</b>
3.1 Introduction .....	53
3.2 Experimental .....	55
3.2.1 Fabrication of hollow fibers .....	55
3.2.2 Injection of liquid metal .....	56

3.2.3 Mechanical Characterization .....	56
3.2.4 Electrical Characterization .....	57
3.3 Results and Discussion .....	57
3.4 Conclusion .....	66
3.5 References .....	68
<b>Chapter 4. Towards All-Soft Matter Circuits: Prototypes of Quasi-Liquid Devices with Memristor Characteristics .....</b>	<b>70</b>
4.1 Introduction .....	71
4.2 Experimental .....	73
4.3 Fabrication and Characterization of Soft Matter Based Memristors .....	74
4.4 Conclusion .....	87
4.5 References .....	88
<b>Chapter 5. Inherently Aligned Microfluidic Electrodes Composed of Liquid Metal .....</b>	<b>90</b>
5.1 Introduction .....	91
5.2 Fabrication and Characterization of the Liquid Metal Microelectrodes .....	95
5.3 Advantages and Limitations .....	107
5.4 Conclusions .....	108
5.5 References .....	110
<b>Chapter 6. Three-dimensional Printing of Free Standing Liquid Metal Microstructures .....</b>	<b>113</b>
6.1 Introduction .....	114
6.2 Result and Discussion .....	118
6.3 Conclusion .....	125
6.4 References .....	126

<b>Chapter 7. Tuning the Interfacial Rheological Properties of Eutectic Gallium</b>	
<b>Indium .....</b>	<b>130</b>
7.1 Introduction .....	131
7.2 Mathematical relationships .....	132
7.3 Experimental .....	134
7.4 Results and Discussion .....	136
7.5 Conclusion .....	139
7.6 References .....	141
<b>Chapter 8. Summary and Outlook .....</b>	<b>143</b>
8.1 Summary .....	144
8.2 Future Outlook .....	146

## LIST OF TABLES

<b>Table 1.1</b>	Physical parameters of gallium and gallium based alloys in comparison with mercury and water <sup>[30-33, 38]</sup> .....	8
------------------	---	---

## LIST OF FIGURES

<b>Figure 1.1</b>	(a) Schematic illustration and photo of a self assembled monolayer junction between gold and mercury electrodes. <sup>[3]</sup> (b) Microfluidic splitting resonator. Mercury flows into and out of a microchannel in the device. <sup>[4]</sup> (c) Surface tension driven microactuation of a mercury droplet based on continuous electrowetting. <sup>[5]</sup> .....	3
<b>Figure 1.2</b>	(a) Scanning electron microscopy (SEM) and optical microscopy images of inorganic structures on elastomeric substrates. The structures show different approaches to stretchable inorganic materials. <sup>[17]</sup> (b) Optical microscopy images and maximum strain distributions for serpentine interconnects composed of gold thin films. <sup>[17]</sup> .....	4
<b>Figure 1.3</b>	(a) SEM image of a gold network with microcracks at 20% strain. The applied strain is along the x-axis. <sup>[18]</sup> (b) The resistance of 50 nm thick gold stripe on a silicone elastomer increases with applied strain more than 3% and generates cracks perpendicular to the stretch direction. <sup>[19]</sup> ....	5
<b>Figure 1.4</b>	(a) Surface tension driven self-folding of patterned polyhedral. Two dimensional templates fold when solder hinges between adjacent faces melts. <sup>[26]</sup> (b) Injection of liquid solder into microchannels produces deformable metallic structures. <sup>[21]</sup> .....	6
<b>Figure 1.5</b>	(a) Photographs of a stretchable loop antenna. The antenna is stretched, folded, and twisted. <sup>[39]</sup> (b) The resonance frequency of a stretchable dipole antenna shifts as a function of applied strain. The mechanical deformation and the resulting frequency are reversible. <sup>[42]</sup> .....	9
<b>Figure 1.6</b>	(a) Photograph of a prototype of capacitive microfluidic device formed by embedding Galinstan within PDMS elastomer (top left), and a layout of microchannels (top right). Sensitivity of pixels to direct and indirect loading (bottom). <sup>[48]</sup> (b) Multilayered soft artificial skin sensor with embedded EGaIn microchannels. <sup>[46]</sup> .....	10
<b>Figure 1.7</b>	The electrically insulating oxide skin on the EGaIn electrode is reduced or oxidized further depending on the direction of the bias, thereby allowing unidirectional ionic current. (a) A schematic depiction of the soft-matter diode with asymmetrically configured polyelectrolyte gels under forward and backward biases. (b) Current rectification of an EGaIn/electrolyte solution/Pt diode. The negative bias reduces the insulating oxide layer at the interface of the liquid metal. The positive	

	bias oxidizes the liquid metal resulting in a resistive barrier for electrical current. <sup>[57]</sup> .....	12
<b>Figure 1.8</b>	(a) A series of side-view snapshots of EGaln between the two parallel plates of the rheometer. The plate rotated to the right of the center position (top), returned to its initial center position (middle), and the relaxed skin appeared crumpled after being stretched. The plate rotated to the left of the center position, and the creases of the skin slanted accordingly (bottom). (b) A plot of elastic and viscous modulus as a function of stress for EGaln. The data shows that the EGaln flows readily beyond a critical surface stress (0.5 N/m). <sup>[34]</sup> .....	16
<b>Figure 1.9</b>	(a) A series of photographs of the formation of a conical tip of EGaln. From left to right: A micromanipulator 1) brings a drop of EGaln suspended from a needle into contact with a substrate, and 2) raises the needle until the EGaln separates into a conical tip (which remains attached to the needle) and a drop on the substrate. <sup>[50]</sup> (b) Characterization of molecular rectification in Metal–SAM–Metal Oxide–Metal Junctions by using EGaln soft top contacts. <sup>[51]</sup> .....	17
<b>Figure 1.10</b>	Pressure to fill EGaln or Hg into microchannels increases as a function of the inverse of the smallest width (1/W) of the channel. <sup>[34]</sup> .....	19
<b>Figure 1.11</b>	(a) (A, C) EGaln droplets imaged by scanning electron microscopy (SEM) and (B, D) transmission electron microscopy (TEM). EGaln dispersed in (A and B) 3-mercaptopropionamide (1ATC9), and (C and D) 1-dodecanethiol (C12). <sup>[89]</sup> (b) EGaln droplet formation in aqueous PEG solution using a microfluidic device. A series of images shows droplet generation at different flow rate ratios. <sup>[90]</sup> .....	20
<b>Figure 2.1</b>	(a) Fabrication process of a reversibly deformable dipole antenna. PDMS elastomer cured on a topographically-patterned substrate produces two adjacent microfluidic channels (only one shown). After sealing the PDMS channels to another piece of PDMS, injection of liquid metal alloy into the microfluidic channels produces a dipole antenna. (b-c) Photographs of a prototype antenna being stretched and rolled. There is no hysteresis in the spectral properties of the antenna as it is returned to the “relaxed” state. (d) The antenna self-heals in response to sharp cuts, such as those inflicted by a razor blade. ....	38
<b>Figure 2.2</b>	A schematic depiction of a dipole antenna before and after being stretched. The ability to stretch the antenna improves its overall durability and allows it to sense strain by the modulation of the spectral response during elongation .....	40

<b>Figure 2.3.</b>	Photographs of the device used to stretch the fluidic antenna. (a) Two clamps with four screws secure each end of the antenna and slide parallel to the long axis of the antenna. (b) The dipole fluidic antenna mounted in the device. Two main screws exerted the required force to push the clamps away from each other; this motion caused the antenna to elongate in a controlled manner.....	40
<b>Figure 2.4</b>	A plot of the measured reflection coefficient of the dipole both in its “relaxed” position (54 mm length) and mechanically elongated positions (58, 62, and 66 mm length) as a function of frequency. The ability to stretch the antenna allows the frequency to be tuned mechanically. ....	42
<b>Figure 2.5</b>	Resonant frequency of a fluidic dipole antenna as a function of the length of the antenna as modulated by stretching. The calculated values were modeled using finite element modeling. ....	43
<b>Figure 2.6</b>	Photograph of a partially filled patch antenna taken as the liquid metal fills the antenna in a serpentine fashion to ensure uniform and complete filling of the patch geometry. (right) A close-up micrograph of the leading edge of the liquid.....	45
<b>Figure 2.7</b>	Photograph of a complete, evenly filled patch antenna and ground plane. (left) A close-up micrograph of a representative region of the radiating element shows the PDMS posts and the evenly filled liquid metal.....	45
<b>Figure 3.1</b>	(a) Optical image of the cross-section of a hollow fiber. (b) The inner diameter (ID) and wall thickness (WT) of the fibers decrease with spinning rate.....	58
<b>Figure 3.2</b>	(a) A relaxed, 2 cm section of an ultra-stretchable conductive fiber. The shiny core of its cross-section (inset) is the liquid metal. (b) The fiber is stretched to 20 cm and the metal appears to uniformly fill the stretched fiber.....	59
<b>Figure 3.3</b>	The strain-stress plots of elastomeric hollow (hollow symbols) and filled (solid lines) fibers with two different spinning rates. The fibers have the same mechanical properties with and without the metal. ....	60
<b>Figure 3.4</b>	Cycling test on the mechanical properties of the hollow fibers fabricated with a spinning rate of 1000 m/min. Beyond the first cycle (largest stress), the fibers show minimal signs of mechanical hysteresis. ....	61
<b>Figure 3.5</b>	The experimental (filled squares) and two sets of theoretical resistance (empty triangles and circles) of conductive fibers with two different	

	spinning rates of (a) 100 and (b) 1000 m/min. The resistance increases as the applied strain increases. ....	64
<b>Figure 3.6</b>	(a) Stretchable charger for electronic devices and (b) stretchable cable for earphones.....	66
<b>Figure 4.1</b>	Fabrication process of the memristive circuit with a crossbar structure. Two PDMS sheets with four circular holes of diameter $\sim 2$ mm were prepared to support hydrogel pellets doped with PAA (blue) or PEI (red). Another set of two PDMS sheets with line patterns were prepared by soft lithography (i.e., replica molding). Each PDMS sheet with holes was assembled with the PDMS sheet with line patterns and sealed by using oxygen plasma. After inserting the gel pellets into the holes, the two sets of PDMS sheets were aligned perpendicularly to create four nodes with gel-gel interface. The liquid metal was injected into the line channels by using a syringe and tubes to form electrodes at the top and bottom of the stacked gel layers.....	74
<b>Figure 4.2</b>	Soft memristor prototypes based entirely on soft materials. (a) A schematic depiction of the memristive device. Two polyelectrolytes entrapped in a matrix of agarose/H <sub>2</sub> O dictate the pH values of each hydrogel layer. (b) I-V curves of the device by $\pm 5$ V sweeps. The numbers and the arrows represent the order and the direction of the bias sweeps, respectively. The hysteresis of the I-V curves is the characteristic feature of memristors. The red dotted line indicates the reading bias of 1 V, where the “memorized” resistance is measured. The sweep rate is 0.04 V/s. ....	76
<b>Figure 4.3</b>	Proposed operating mechanism of the gel/liquid metal memristors based on the electrochemical behavior of the oxide skin of the metal in PAA or PEI polyelectrolyte solution. (a) Cross-sectional view of the experimental set-up for the observation of the surface of the EGaIn electrodes in each polyelectrolyte solution. Flexible plastic tubes of diameter $\sim 500$ $\mu\text{m}$ filled with EGaIn were inserted from the bottom of the solution reservoir. The concentrations of PAA and PEI are 7.5 wt. % and 5.7 wt. %, respectively. (b, c) Optical images of the top surface of the EGaIn electrodes to which voltage is applied in PAA (b) or PEI (c) solution. In the presence of aqueous PAA, a thick oxide layer on the EGaIn electrode is formed or removed depending on the applied bias. In the presence of aqueous PEI, the oxide layer formed by the applied bias is unstable and is spontaneously removed. (d) Proposed mechanism of memristor-like function based on the electrochemical behavior of the oxide skin of the EGaIn electrodes. Since the interface of PEI/EGaIn	

	stays conductive, the formation and dissolution of an oxide layer at the PAA/EGaIn interface determines the resistance of the memristor. ....	78
<b>Figure 4.4</b>	The effect of pH conditions on the formation of oxide skin on the EGaIn electrodes. (a) Optical images of the surface of the EGaIn electrodes to which the voltage is applied in PAA or PEI polyelectrolyte solution of the same concentration as the memristor device. (b) The EGaIn electrodes in aqueous solution with identical pH values as the memristor device show the same surface morphological changes in terms of the bias application, which suggests that the different pH values of PAA and PEI polyelectrolyte solutions result in the difference in the oxide formation.....	79
<b>Figure 4.5</b>	(a) Symmetric I-V traces with no hysteresis occur when electrochemically inert metals, such as platinum, were used as electrodes. (b) The device with Al electrodes shows slight I-V hysteresis because Al also forms an oxide layer on its surface. Compared to solid Al metal, it appears that the liquid EGaIn metal has the advantage of self-regeneration due to its fluidity, which results in reproducible hysteresis and more reliable memristive performance.....	80
<b>Figure 4.6</b>	The device with symmetric PAA polyelectrolyte gel exhibited hysteretic I-V curves initially. However, since the oxide skin grows at both electrodes under the pH environment of PAA, total resistance of the device continuously increases as the bias loop is repeated.....	81
<b>Figure 4.7</b>	Slight hysteresis occurs in the device with only PEI polyelectrolyte gel, which is maintained even in the consecutive bias cycles (left). However, the off-state resets spontaneously to the on-state after ~10 min because the oxide skin is unstable and removed under the PEI environment (right). ....	82
<b>Figure 4.8</b>	Performance characteristics of the gel/liquid metal memristors. (a) Conductance through the device depends on the pre-applied bias history. The current is suppressed (off state) below the maximum pre-applied voltage. (b) Switching performance of the memristors. (c) Long-term stability of the stored information. The low-conductance, i. e. ‘off’ state, is restored to ‘on’ state after 3 hrs by applying the switching bias. A switching bias of $\pm 5$ V was applied to the memristors for 3 sec for the experiments of b and c. ....	83
<b>Figure 4.9</b>	Effect of the duration of switching bias on the on/off ratio of the memristor. The “on” state becomes slightly more conductive at longer switching times and the “off” state becomes slightly less conductive at	

	longer switching times. Regardless, switching occurs after only 1 s of applying the switching bias.....	85
<b>Figure 4.10</b>	A crossbar array of soft material-based memristors. (a) Photograph of a prototype of an integrated memristor circuit with a $2 \times 2$ crossbar array. The device is flexible as shown in the inset image and compatible with water. (b) Schematic of the prototype in (a). The arrows point to the nodes. (c) Switching performance of the memristor circuit device. The switching bias to turn ‘off’ (+ 5 V) and ‘on’ (– 5 V) the nodes is applied to the 1-B node for the first and second cycles and to the 2-A node for the third cycle, respectively, as shown by the arrows. The filled symbols represent the nodes in the ‘off’ state. The switching bias was applied to each node for 1 sec to minimize the crosstalk. ....	86
<b>Figure 5.1</b>	(a) Cut-away depiction of the process used to fabricate liquid metal microelectrodes in contact with a central fluidic channel. Two parallel rows of posts separate the liquid metal electrodes from the fluidic channel. (Not shown: The channels are sealed on top by a flat slab of PDMS.) (b) Top-down, back-lit optical micrograph of the fluidic channel flanked by two liquid metal electrodes. The posts prevent the metal from entering the fluidic channel. ....	96
<b>Figure 5.2</b>	Optical micrograph of microfluidic electrodes. (a) Electrodes flush with the central fluidic channel fabricated by injection. (b) Electrodes recessed from the channel. ....	98
<b>Figure 5.3</b>	Optical micrographs of the EGaIn (a) and Ga (b) electrodes after applying 2 V DC bias for 10 sec. Ga electrodes are stable in the solid state while one EGaIn electrode deforms as its thin oxide layer is reduced.....	102
<b>Figure 5.4</b>	Optical micrographs of EGaIn electrodes under AC sinusoidal electric bias at 2V with two different frequencies 10 kHz (a) and 0.1 kHz (b). The dotted lines in (b) represent the location of PDMS posts and where the metal interface placed before applying bias. The EGaIn electrodes show improved mechanical stability as (c) the AC frequency increases at constant ionic concentration (0.1 M NaCl) and (d) the ionic concentration decreases at constant electric bias (10 V). ....	104
<b>Figure 5.5</b>	Optical micrographs of EGaIn electrodes for a microfluidic mixer. (a) Two adjacent fluids undergo laminar flow with minimal mixing. The red colored oil is more conductive than the transparent oil. (Note: The PDMS posts are not visible adjacent to the bottom electrode due to index matching. Reflections from the surface of the metal appear as	

	discoloration in these images) (b) The two fluids mix rapidly when 100 V DC bias is applied. ....	106
<b>Figure 6.1.</b>	A series of sequential images in which a syringe needle extrudes liquid metal to form a straight wire on a withdrawn substrate (from left to right). The oxide skin on the surface of the metal stabilizes the liquid metal wire against gravity. The outer diameter of the hollow needle and the extruded wire is 500 and 270 $\mu\text{m}$ , respectively. The length of the final wire shown is 8 mm before it was intentionally ended by applying vacuum to the syringe. ....	119
<b>Figure 6.2.</b>	Photographs of the diverse free standing, liquid metal microstructures. (a) Liquid metal spouted rapidly from a glass capillary forms a thin wire. (b) Suspended liquid metal fibers formed by rapidly extruding the metal from a syringe. The fiber is strong enough to suspend over a gap. (c) A free standing liquid metal arch structure spanning $\sim 3$ mm. (d) Tower, (e) $3 \times 3 \times 3$ cube array and (f) crossover lines composed of liquid metal droplets. The droplets act as building blocks and form continuous physical and electrical junctions. (g) An array of in-plane lines of free standing liquid metal fabricated by filling a microchannel with the metal and removing the mold. Scale bars represent 500 $\mu\text{m}$ . ....	121
<b>Figure 6.3.</b>	Observed (dot) and fitted (line) tensile force as a function of the minimum circumference of the extruded wire. The slope of the graph represents the stress required to yield the surface oxide skin during the extrusion process, which is $\sim 0.77$ N/m. ....	123
<b>Figure 6.4.</b>	(a) A prototype device composed of two LEDs and stretchable wire bonds connecting them in PDMS (Inset: Micrograph of the liquid metal wire bonds). (b-d) The fluidic property of the metal wire in the elastomer allows stretchability (b) and flexibility (c, d) of the device and keeps its electrical continuity. ....	124
<b>Figure 7.1</b>	A schematic of the experimental setup. EGaIn is sandwiched between an oscillating top plate and a stationary bottom plate. All the resistance to top plate movement is generated by the skin on EGaIn and the instrument measures the strain ( $\gamma$ ) while controlling stress ( $\sigma$ , Pa). To test EGaIn in different chemical environments, an acrylic reservoir fits firmly with the dummy bottom plate. The reservoir is filled with different liquids, which we call the “surrounding liquids”, to quantify their effect on the mechanical properties of the skin on EGaIn. ....	135

**Figure 7.2** Oscillatory stress sweep of EGaIn in air, water and after drying. All the reported values are for surface modulus. The elastic modulus plateaus before the liquid metal yields beyond a critical stress. The elastic modulus decreases by an order of magnitude in water. The yield stress is also reduced by approximately a factor of three. The elastic modulus and yield stress of the dried metal is higher than the elastic modulus of the metal in water..... 137

**Figure 7.3.** Removal of the oxide skin using acid causes the modulus of the skin to decrease significantly with time. The mechanical modulus in 0.1 M HCl solution drops down continuously over time whereas the metal in 0.001M HCl solution shows similar value of the metal in water. We suspect that the skin is thinning with time in 0.1 M HCl solution as indicated by the continuous decrease in elastic modulus..... 138

# **Chapter 1. Introduction**

This dissertation describes the study of a micro-moldable liquid metal, eutectic gallium indium (EGaIn) for the fabrication of soft and stretchable electronics with new functionality and for novel approaches to pattern metallic microcomponents. Although much is known about the metal, our studies focus on the composite system of the metal surrounded by an oxide skin. Thus, the unique contribution of this thesis is new insights into controlling the interfacial and electronic properties of the metal. In this chapter, we provide a general overview on previous research on EGaIn as well as other low melting temperature liquid metals and their applications. EGaIn has a thin solid oxide on its surface and the oxide skin dictates electrical and rheological properties of the liquid metal. We discuss the properties of the oxide skin and resulting unique behaviors of the liquid metal on the microscale. This background information motivates the work described in this dissertation.

### **1.1 General Information on Low Melting Temperature Metals and their Applications**

Low melting temperature metals and alloys hold great promise for forming soft and conformal metallic contacts, electro-microfluidic components, and highly deformable electronics. The ability for liquid metals to flow also offers a new fabrication paradigm (e.g., injection) for metallic components and new opportunities for shape reconfigurable electronics.

Mercury is one of the most well-known liquid metals and it has a number of uses. For example, mercury dropping electrodes benefit from the fluidic properties of the liquid metal. Pumping the liquid metal from a capillary maintains a pristine and clean electrode surface, which is desired for sensitive electrochemical measurements such as the voltammetric

detection of trace-metals and organics in solutions.<sup>[1, 2]</sup> Mercury also has been used as a top electrode to measure electrical properties of molecular junctions such as self assembled monolayers (SAMs) between two metal electrodes as shown in **Figure 1.1(a)**.<sup>[3]</sup> The mercury electrode supporting thin molecular layers is compliant and provides conformal contact to the topography of a solid surface. This ability minimizes the potential of shorting and of mechanical damage to the organic molecular layers. The fluidic properties such as low viscosity also allow new applications of the metal in electronics and microfluidics (Figure 1.1(b) and (c)).<sup>[4-6]</sup> However, mercury has high surface energy and tends to minimize the surface area which makes it difficult to control the shape and the fluidic behavior. Moreover, mercury is toxic,<sup>[7-10]</sup> thus its use is widely eschewed.

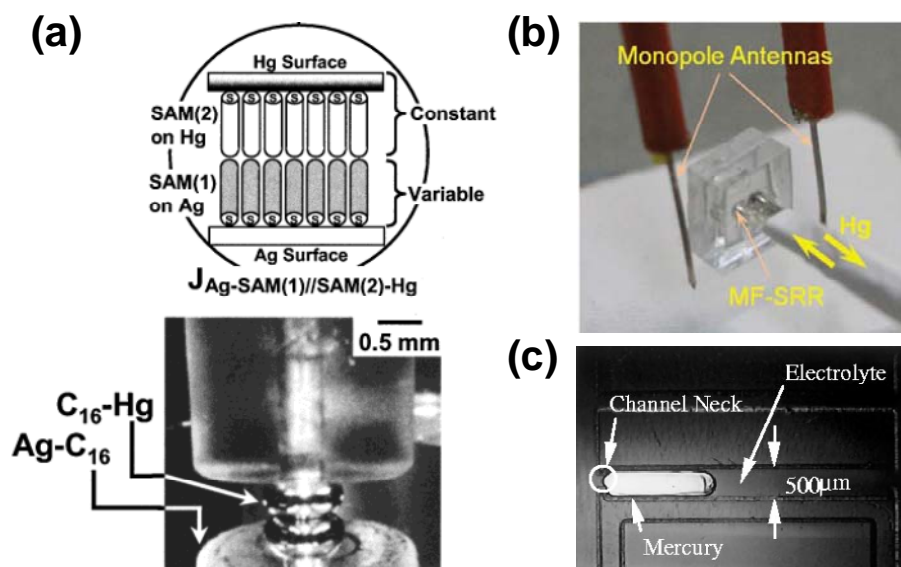


**Figure 1.1** (a) Schematic illustration and photo of a self assembled monolayer junction between gold and mercury electrodes.<sup>[3]</sup> (b) Microfluidic split-ring resonator. Mercury flows into and out of a microchannel in the device.<sup>[4]</sup> (c) Surface tension driven microactuation of a mercury droplet based on continuous electrowetting.<sup>[5]</sup>

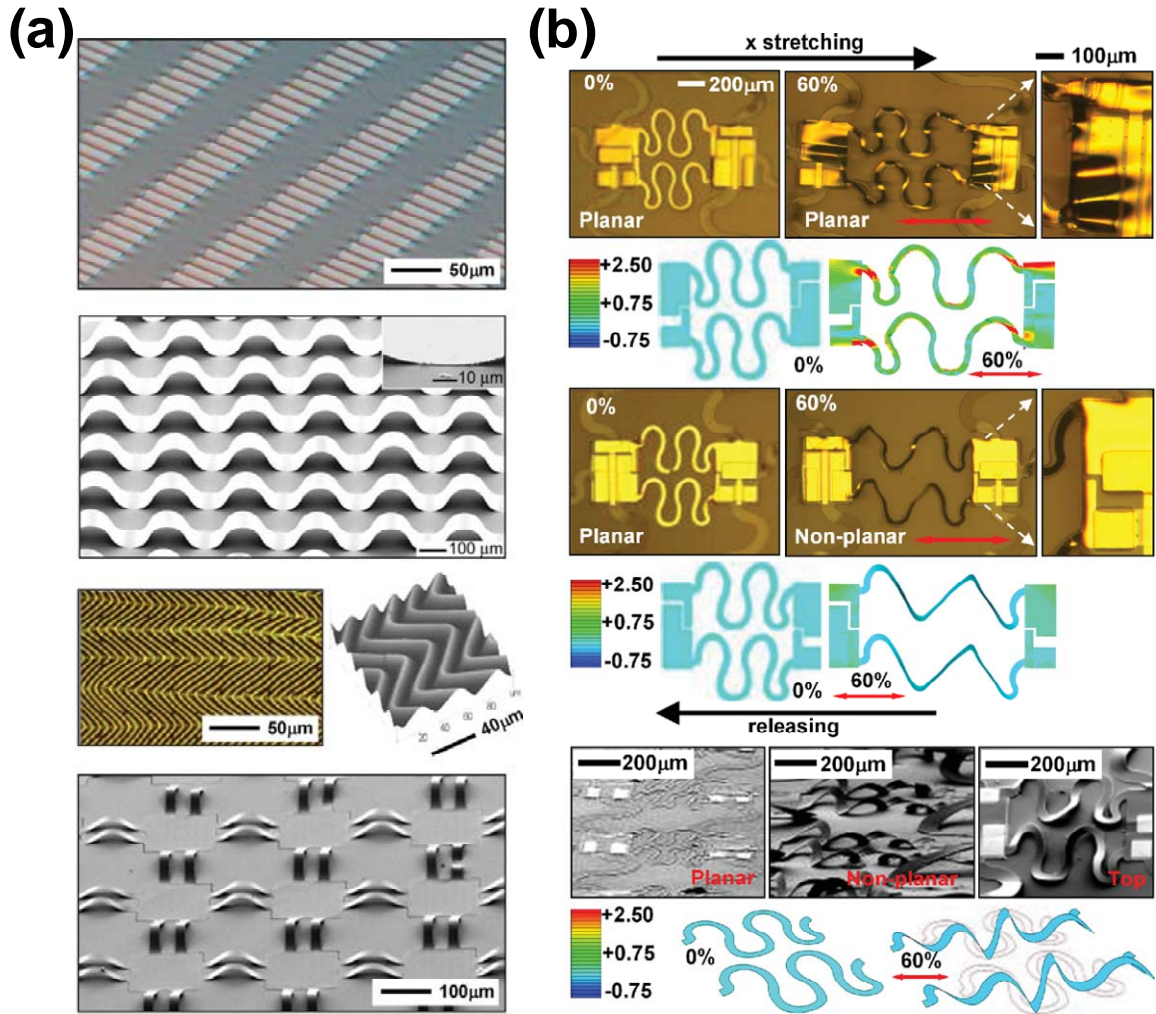


**Figure 1.2** (a) Scanning electron microscopy (SEM) and optical microscopy images of inorganic structures on elastomeric substrates. The structures show different approaches to stretchable inorganic materials.<sup>[17]</sup> (b) Optical microscopy images and maximum strain distributions for serpentine interconnects composed of gold thin films.<sup>[17]</sup>

Recently, the emerging field of flexible electronics triggered more need and interest in liquid metals to replace solid metals (e.g. copper), which have limitations with respect to the type and amount of mechanical deformation they can endure. The flexibility of solid metals in conventional flexible electronics mainly stems from their geometries (not from

intrinsic properties).<sup>[11-16]</sup> **Figure 1.2** shows the different approaches that can offer stretchability and compressibility in brittle materials and how strain is distributed in the solid structures.<sup>[17]</sup> Although thin films of solid metals are flexible, they show limited stretchability and durability with repeated deformation (**Figure 1.3**).<sup>[18-20]</sup> In contrast to solid metals, liquid metals flow in response to applied stress and are therefore highly deformable and durable without generating cracks or fatigue. Here, we discuss new functionalities and capabilities of low melting temperature metals other than mercury.

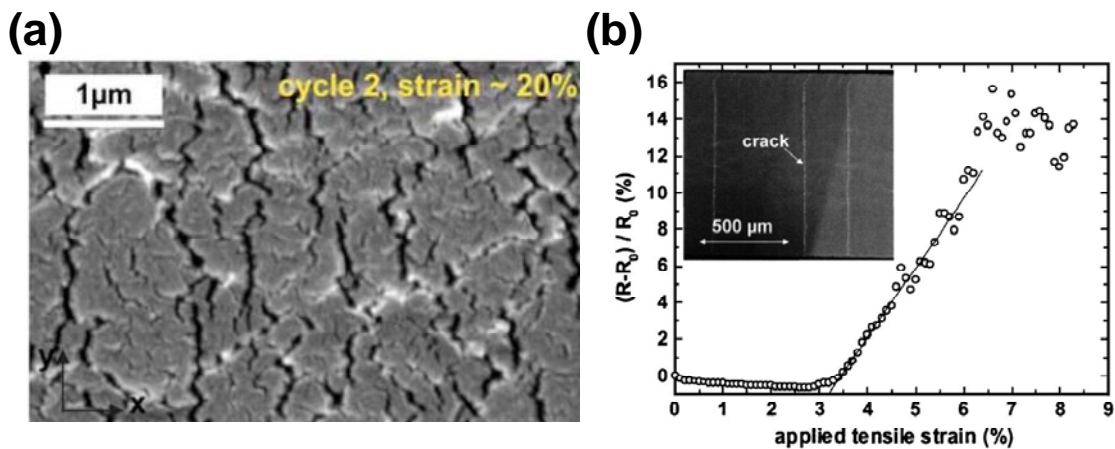


**Figure 1.3** (a) SEM image of a gold network with microcracks at 20% strain. The applied strain is along the x-axis.<sup>[18]</sup> (b) The resistance of 50 nm thick gold stripe on a silicone elastomer increases with applied strain more than 3% and generates cracks perpendicular to the stretch direction.<sup>[19]</sup>

This dissertation focuses on a eutectic alloy of gallium and indium (EGaIn, 75 % Ga 25 % In by weight) to replace solid metals in soft electronics and microcomponents and also provide new functionalities. EGaIn is liquid at room temperature and has a low level of toxicity unlike mercury. As one of the components of the liquid metal, Indium has a

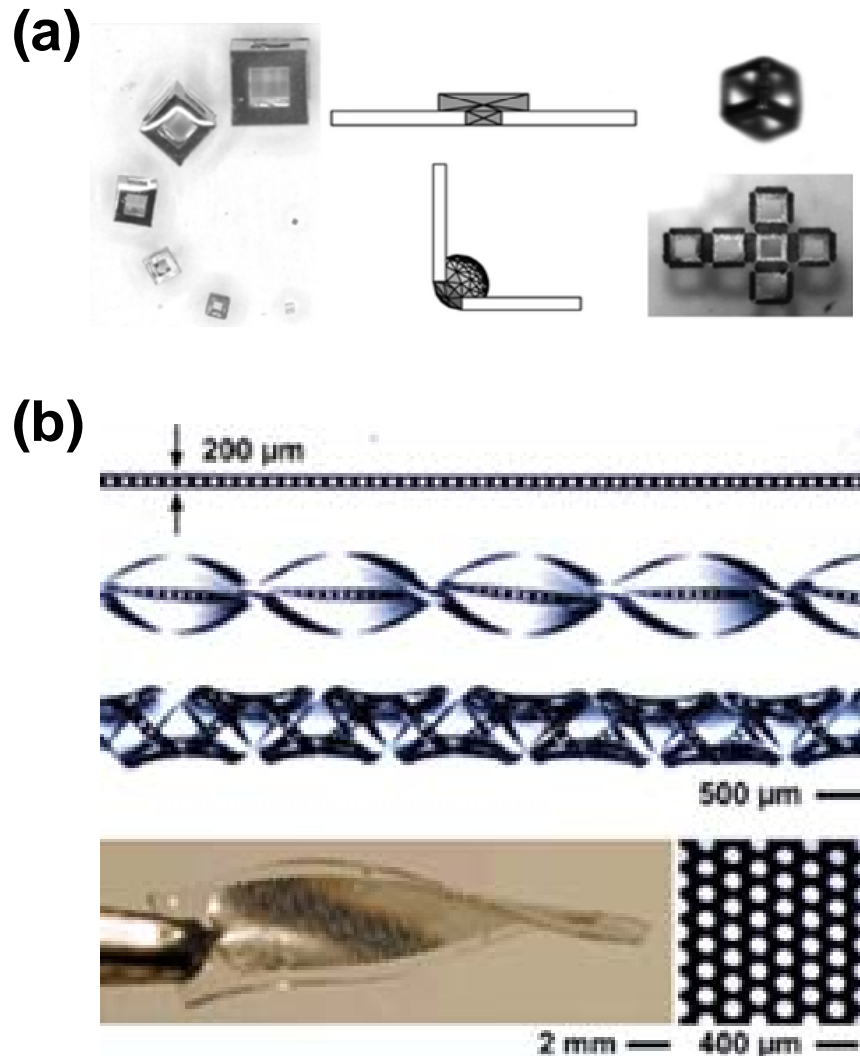


**Figure 1.4** (a) Surface tension driven self-folding of patterned polyhedral. Two dimensional templates fold when solder hinges between adjacent faces melts.<sup>[26]</sup> (b) Injection of liquid solder into microchannels produces deformable metallic structures.<sup>[21]</sup>

relatively low melting point ( $\sim 158\text{ }^{\circ}\text{C}$ ) compared to popular solid metals such as copper and gold.<sup>[21]</sup> The metal can be easily liquefied with mild heating and thus has been widely utilized for reflow soldering in packaging, micromolding and three dimensional (3D) connections of electronic components.<sup>[22-25]</sup> The fluidic properties of the metal may be utilized in self-

folding microstructures(**Figure 1.4(a)**).<sup>[26]</sup> Placing indium at the hinges of two dimensional (2D) structures leads to surface tension-driven folding process as the metal heats above its melting point. More recently, Siegel and coworkers reported a new concept of “microsolidics” by injecting molten indium or indium alloys into microchannels(**Figure 1.4(b)**).<sup>[21]</sup> The method takes advantage of microfluidic techniques to fabricate complex metallic microstructures in 3D. Solid metallic components (e.g. electrodes, heaters, inductors, electromagnets) form by injecting metals at elevated temperatures into microchannels and then cooling them subsequently to room temperature.<sup>[27-29]</sup> Because the metallic components are thin and composed of soft metals, they can be flexed, bent, or twisted.

Gallium and gallium based alloys such as EGaIn and eutectic gallium indium tin (Galinstan, 68.5% Ga, 21.5% In, 10% Sn) have lower melting points than indium (Ga ~30°C, EGaIn ~15.7°C, GaInSn ~ -19°C).<sup>[30-32]</sup> Gallium exhibits the largest temperature difference between the melting point (30 °C) and boiling point (2200 °C) among all elements,<sup>[30, 33]</sup> and has effectively no vapor pressure at room temperature, in contrast to mercury. The promise of the liquid metals to replace solid metals in microelectronics and microfluidics promoted studies on the physical and mechanical properties of the metals. Initial studies on the mechanical and rheological properties of EGaIn show that the surface oxide layer dictates those properties.<sup>[34]</sup> As a result, the critical pressure required to induce the flow into microchannels depends on the size of the channels. More in-depth studies on the rheological properties of the liquid metal showed that the oxide skin has non-Newtonian behavior with viscoelastic properties.<sup>[35]</sup> Other groups have characterized the fluidic properties of Galinstan such as contact angles, surface tension and electrowetting behavior for applications in

microdevices.<sup>[36, 37]</sup> EGaIn is more expensive than copper which is wide used in electronics. However, the amount of the metal required in micro-electrosystems is on microliter scales, thus the value from new functionalities could exceed the cost. **Table 1.1** summarizes the physical properties of gallium, EGaIn and Galinstan, and compare them with those of water and mercury. We focus our studies here on EGaIn. We avoided using gallium in most cases because it has a freezing point above room temperature. We avoided using Galinstan because a ternary system is potentially more complicated to study than a binary system.

**Table 1.1** Physical parameters of gallium and gallium based alloys in comparison with mercury and water <sup>[30-33, 38]</sup>

	Gallium	GaIn	Galinstan	Hg	Water
Melting point (°C)	29.8	15.7	-19	-39	0
Boiling point (°C)	2200	2000	>1300	357	100
Density (kg m <sup>-3</sup> )	6100	6250	6440	13599	1000
Thermal conductivity (W mK <sup>-1</sup> )	28	41.8	16.5	7.8	0.61
Viscosity (10 <sup>-3</sup> kg m <sup>-1</sup> s <sup>-1</sup> )	1.96	1.99	2.4	1.55	1
Electric resistance (mΩ m)	0.27	0.29	0.29	0.96	1.8×10 <sup>8</sup>

Because of their potential for substituting mercury in electronic and microfluidic applications, the gallium and gallium based alloys have been utilized in applications including reconfigurable and stretchable antennas,<sup>[39-45]</sup> pressure sensors,<sup>[46-48]</sup>

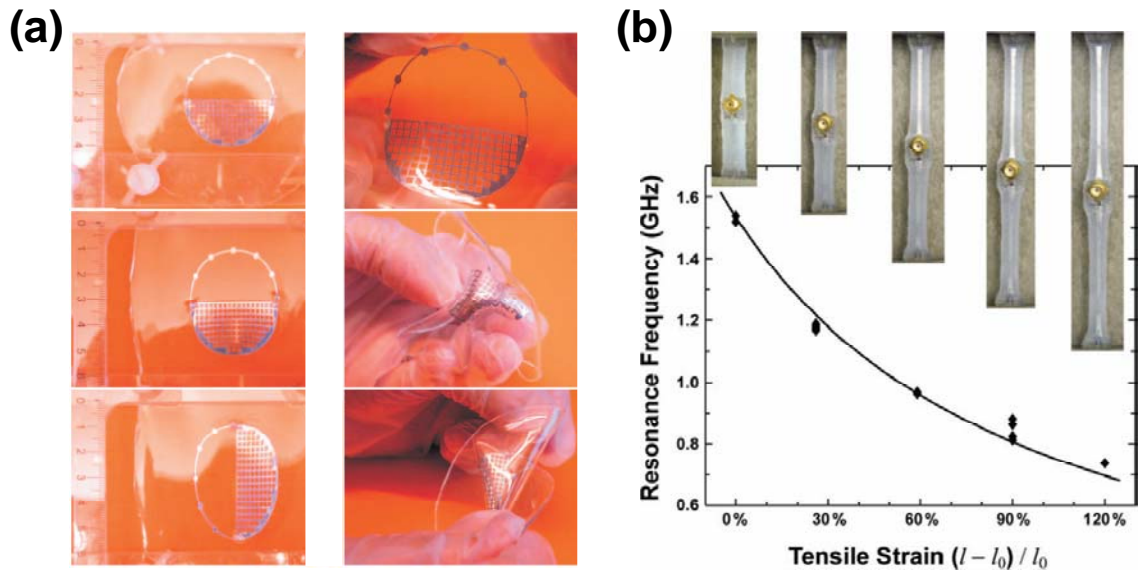


**Figure 1.5** (a) Photographs of a stretchable loop antenna. The antenna is stretched, folded, and twisted.<sup>[39]</sup> (b) The resonance frequency of a stretchable dipole antenna shifts as a function of applied strain. The mechanical deformation and the resulting frequency are reversible.<sup>[42]</sup>

interconnects,<sup>[49]</sup> soft and conformal electrodes for molecular junctions,<sup>[50-55]</sup> reconfigurable plasmonic devices,<sup>[56]</sup> microelectrodes,<sup>[57-59]</sup> soft matter based diodes and memristors,<sup>[57, 60]</sup> photovoltaic devices,<sup>[61-63]</sup> coolant for computer chips in place of water.<sup>[33, 64]</sup> Flexible and stretchable electronics such as stretchable and reconfigurable antennas and sensors is one of the most popular applications of the liquid metals. As discussed in Chapter 2, we describe different types of reconfigurable antennas by injecting EGaln into elastomeric casings with different geometries.<sup>[40, 41, 45]</sup> Other groups also reported reversibly deformable and stretchable antennas by using highly stretchable elastomers (**Figure 1.5**).<sup>[42, 43]</sup> Galinstan has been also used as conductive elements in stretchable antennas.<sup>[39, 44]</sup> Soft artificial skin that senses strain and normal force has been reported (**Figure 1.6**).<sup>[46, 48, 65]</sup> The sensors are

formed by injecting EGaIn or Galinstan into elastomeric microchannels. The surface pressure and in-plane strain induce electrical resistance changes in the conductive channel. The ability of the metal to flow readily in response to applied stress also allows a fast and simple way to fabricate self-aligned microelectrodes. Chapter 5 describes one method to fabricate inherently aligned electrodes in microchannels.

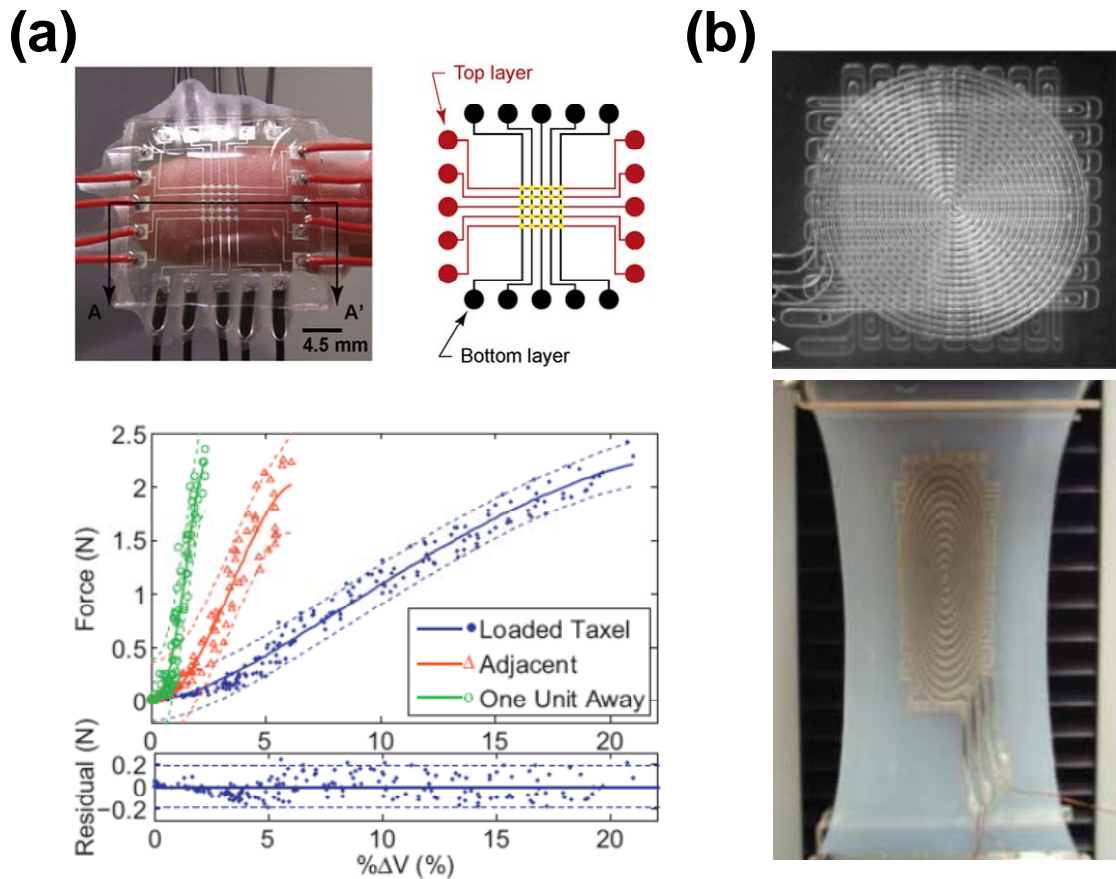


**Figure 1.6** (a) Photograph of a prototype of capacitive microfluidic device formed by embedding Galinstan within PDMS elastomer (top left), and a layout of microchannels (top right). Sensitivity of pixels to direct and indirect loading (bottom).<sup>[48]</sup> (b) Multilayered soft artificial skin sensor with embedded EGaIn microchannels.<sup>[46]</sup>

It is possible to form cone-shaped EGaIn top electrodes to measure tunneling current through self assembled monolayers.<sup>[50]</sup> The cones form by bifurcating a droplet of the metal and the presence of the oxide skin helps stabilize the shape of the metal. EGaIn provides soft, non-damaging contacts and showed better yield than deposited solid metal electrodes or mercury electrodes. After this pioneering work, the liquid metal has been used to measure characteristics of various types of molecular junctions.<sup>[50, 51, 53-55]</sup> These soft electrical contacts can also be fabricated by injecting EGaIn into microchannels.<sup>[27, 57]</sup> EGaIn also accomplished great conformal contact with a rugged polymer substrate and showed good performance as an electrode of photovoltaic cells.<sup>[63]</sup> Surmann and coworkers tested the voltammetric behavior of Galinstan and showed the potential windows of use for different pH values are similar to those obtained with conventional mercury electrodes.<sup>[66]</sup> Knoblauch and coworkers reported microinjection of organelles into cells with minimal cellular damage by using the heat-induced expansion of Galinstan within a pipette.<sup>[67]</sup>

The ability to create soft electrodes offers an opportunity to interface with other soft materials to create electronic analogs that are composed entirely of soft materials. Chapter 4 describes a memory resistors composed of hydrogel and EGaIn. The ability to control the thickness, and thus resistivity, of an insulating oxide skin on the metal enables the current rectification. This property can also be used to fabricate soft diodes(**Figure 1.7**).<sup>[57]</sup> Soft devices composed of hydrogels<sup>[68-70]</sup> are of interest because hydrogels are biomcompatible, soft, aqueous, and ionic<sup>[71]</sup>; these features are similar to the features of circuits found in biology including the brain.

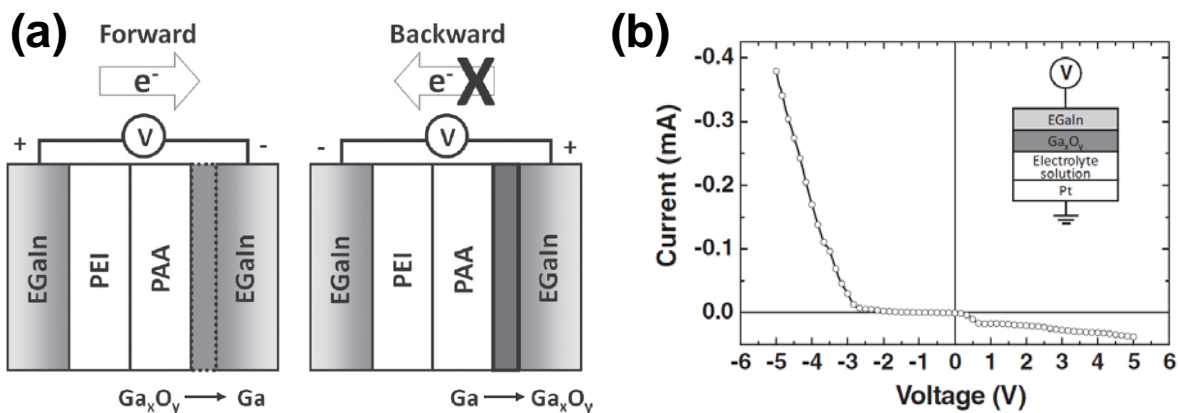


**Figure 1.7** The electrically insulating oxide skin on the EGaIn electrode is reduced or oxidized further depending on the direction of the bias, thereby allowing unidirectional ionic current. (a) A schematic depiction of the soft-matter diode with asymmetrically configured polyelectrolyte gels under forward and backward biases. (b) Current rectification of an EGaIn/electrolyte solution/Pt diode. The negative bias reduces the insulating oxide layer at the interface of the liquid metal. The positive bias oxidizes the liquid metal resulting in a resistive barrier for electrical current.<sup>[57]</sup>

This dissertation focuses on EGaIn because of its fascinating properties for applications including soft electronics, patterning microstructures and microfluidics. EGaIn has low viscosity and high electrical conductivity (more detail will be provided in section 1.2). Moreover, the liquid metal can be micromolded because of the oxide skin that grows spontaneously on the surface of the metal and passivates the inner liquid. The oxide skin stabilizes mechanically the liquid metal and prevents it from resolving to hemispherical structures to minimize surface energy. The ability to mold the liquid metal into microstructures provides a new concept to shape a high surface tension liquid, for example, injection of the metal into microchannels or capillaries (Chapter 2 to 5) and patterning self-supporting 3D microstructures (Chapter 6). These novel ways to control the shape of liquid extend the range of applications with new functionalities and capabilities which would be

impossible with solid metals or high surface tension liquids such as water and mercury. While this dissertation focuses on EGaIn, the conclusions reached will likely be applicable to any liquid alloy containing gallium (e.g., Galinstan) since it would have a thin layer of native gallium oxide which governs the mechanical and electrical properties of the metal.

## 1.2 Properties of Eutectic Gallium Indium

EGaIn does not evaporate and effectively has no vapor pressure at room temperature. The metal is liquid at room temperature (m.p.=15.7 °C<sup>[32]</sup>) which makes this metal more appealing than solders for applications in flexible electronics. EGaIn is capable of remaining in a supercooled liquid state at temperatures below the solidification point for a long time<sup>[72]</sup>. When seeded or stirred, the metal solidifies rapidly. The surface tension of EGaIn (624mN/m) is about ten times higher than that of water.<sup>[38]</sup> The bulk viscosity of EGaIn is  $1.99 \times 10^{-3} \text{ Pa} \cdot \text{s}$ , which is a factor of two greater than that of water.<sup>[32]</sup> Thus the metal readily flows under gravity or applied stress. The density of EGaIn is  $6250 \text{ kg} \cdot \text{m}^{-3}$ <sup>[32]</sup> and the conductivity of EGaIn is  $3.4 \times 10^4 \text{ Scm}^{-1}$ <sup>[38]</sup> which is about eight times more resistive than copper. EGaIn has a thin solid oxide skin on its surface in ambient conditions. The oxide skin allows the metal to be micromolded into different shapes and dictates surface and fluidic properties of the metal. The characteristics of the oxide skin and the advantages are described in Chapter 1.3.

Gallium has a low level of toxicity.<sup>[73]</sup> Gallium alloys have been evaluated as substitutes for mercury dental amalgams and a review summarizes the mechanisms of gallium for health purposes.<sup>[74]</sup> Gallium(III) is the most stable oxidized state of the metal.

Because gallium(III) and ferric salts behave similarly in biological systems, gallium ions often mimic iron ions in medical applications. The gallium ions localize to and interact with many processes in the body in which iron(III) is found (an important exception is hemoglobin, which does not bind to gallium (III)). As these processes include inflammation, which is a marker for many disease states, several gallium salts are used, or are in development, as both pharmaceuticals and radiopharmaceuticals in medicine to treat some cancers, hypercalcemia, allograft rejection, and autoimmune diseases.<sup>[75-82]</sup> The effects of the long term exposure to gallium metal and gallium alloys needs to be studied further before these metals are used in consumer devices.

### **1.3 Surface Oxide of Eutectic Gallium Indium**

The liquid metal has a thin, passivating solid-like oxide skin, i.e., the oxide protects the inner liquid underneath from further oxidation. Studies of the skin by using Auger spectroscopy<sup>[34]</sup> show spectra with an enhanced amount of Ga and O at the surface compared to the bulk, confirming that the skin consists of gallium oxide. This result is consistent with X-ray reflectivity and scattering studies on the surface of the metal.<sup>[83-85]</sup> After sputtering etching the oxide skin off the metal, the surface became enriched with In due to its lower surface energy. However, the gallium oxide displaced In at the surface immediately after the metal is exposed to ambient air. Studies of Galinstan by using XPS confirmed the surface of the metal is also enriched with gallium oxide like EGaIn as a consequence of the preferential oxidation of gallium in the near-surface region.<sup>[86]</sup>

A fascinating advantage of the oxide skin is that it allows the liquid metal to be molded into mechanically stable non-spherical microstructures.<sup>[34]</sup> The skin distinguishes EGaIn from mercury, which tends to bead up to minimize its surface area and is therefore difficult to manipulate. The ability to control the shape of the metal is essential for the liquid metal to be applied in 3D micro-patterning and opens new possibilities in micro-electro systems including antennas, microelectrodes, soft and conformal top electrodes for molecular junctions. Notably, it is possible to mold EGaIn on the  $\mu\text{m}$ -to- $\text{mm}$  size scale (i.e., on the macroscopic scale, EGaIn is not moldable because the skin is unable to support gravitational forces). This observation suggests that its moldability is a function of the ratio of surface area to volume (a ratio which increases as the size of the structure decreases), and is therefore attributable to the properties of its skin.

A rheometer with parallel plate geometry studied the unique mechanical properties of the liquid metal with the oxide skin.<sup>[34, 35]</sup> **Figure 1.8(a)** shows photo images which illustrate how the “skin” on the EGaIn surface deformed during the oscillation of the top plate about the axis normal to the plane of the plate (the bottom plate was stationary). The oscillating stress generates creases in the skin slanted in concert with the rotation. The oxide skin ruptures easily during handling by external force including shear stress, gravity, vibration and agitation since it is floating on a liquid substrate and is only a couple of nanometer thick.<sup>[55]</sup> The liquid metal showed a critical surface stress ( $\sim 0.5$  N/m) above which the oxide skin ruptures and the metal starts to flow (**Figure 1.8(b)**). Once the oxide skin ruptures, any surface of the metal newly exposed to air or water oxidizes immediately.

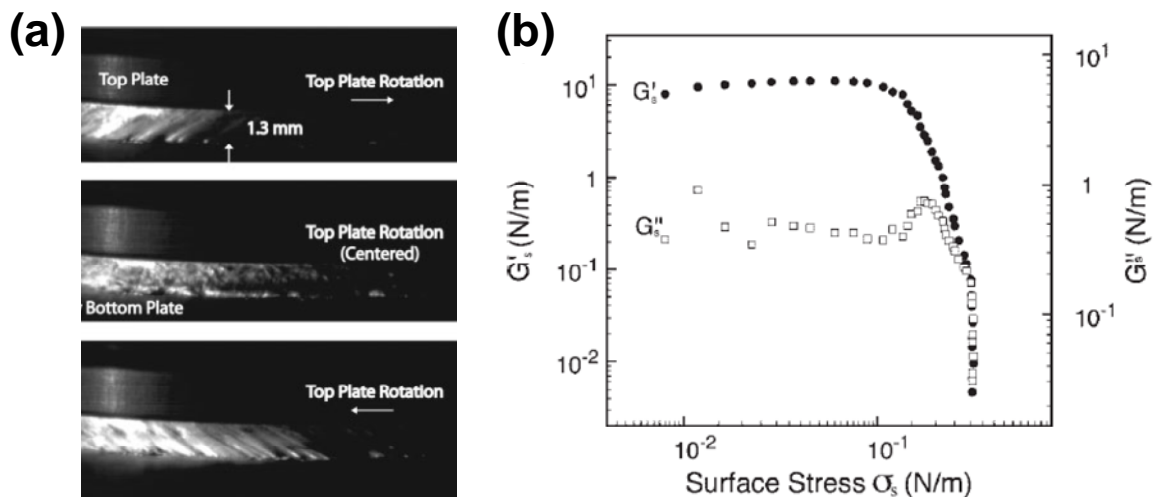


**Figure 1.8** (a) A series of side-view snapshots of EGaln between the two parallel plates of the rheometer. The plate rotated to the right of the center position (top), returned to its initial center position (middle), and the relaxed skin appeared crumpled after being stretched. The plate rotated to the left of the center position, and the creases of the skin slanted accordingly (bottom). (b) A plot of elastic and viscous modulus as a function of stress for EGaln. The data shows that the EGaln flows readily beyond a critical surface stress (0.5 N/m).<sup>[34]</sup>

Oxidized metal wets most surfaces, which makes it very hard to clean the metal from substrates or containers. However, acidic or basic solutions which are strong enough to dissolve the oxide (pH below 3 or above 11),<sup>[87, 88]</sup> remove the skin and reveal shiny and reflective liquid metal surface. In the absence of the skin, the metal beads up on most surfaces. Therefore, the ability of the metal to ‘wet’ surfaces is likely due to the formation of the stiff oxide skin (i.e., the term ‘wetting’ is not an inherent fluid property, as used commonly, but rather a function of the composite oxide-liquid system). Electric bias provides another way to control the thickness of the oxide skin.

## 1.4 Eutectic Gallium Indium on the Micro-scale

On the micrometer length scale, the oxide skin dictates the mechanical and rheological properties, and thus the shape and flow of the metal. Here, we discuss examples of the unique behavior of the liquid metal in microscales and how the properties have been utilized in several applications.

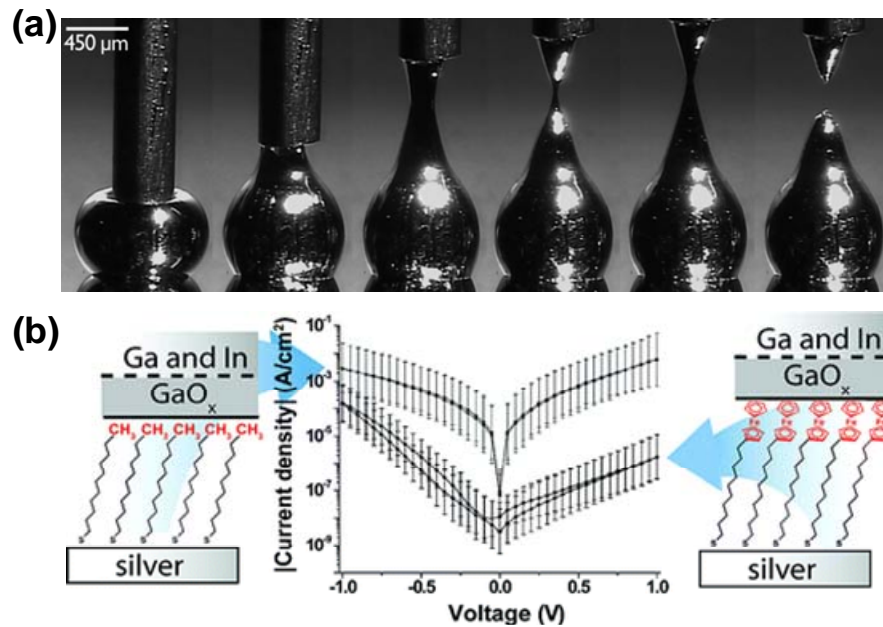


**Figure 1.9** (a) A series of photographs of the formation of a conical tip of EGaln. From left to right: A micromanipulator 1) brings a drop of EGaln suspended from a needle into contact with a substrate, and 2) raises the needle until the EGaln separates into a conical tip (which remains attached to the needle) and a drop on the substrate.<sup>[50]</sup> (b) Characterization of molecular rectification in Metal-SAM-Metal Oxide-Metal Junctions by using EGaln soft top contacts.<sup>[51]</sup>

The surface oxide skin of EGaln allows the metal to be molded into non-hemispherical shapes such as conically shaped microtips. The tips may be formed by suspending a drop of EGaln from a needle, bringing the drop into contact with a bare

substrate, and retracting the needle slowly(**Figure 1.9**).<sup>[50]</sup> The EGaIn adheres to both the needle and the substrate and pinches into to an hour-glass shape until it bifurcates into two structures, one attached to the syringe and one attached to the substrate. The conical tips of EGaIn do not retract into a semispherical droplet (as would high surface tension liquids) and ranges from less than 1  $\mu\text{m}$  to 100  $\mu\text{m}$  in diameter. These tips form soft and stable electrical contacts in micrometer scales with SAMs thus minimize the contribution of defects in the SAMs to tunneling current, resulting in high yields (70-90%).

EGaIn can be injected easily into microfluidic channels because of its low viscosity. Its thin passivating oxide layer provides mechanical stability to the liquid metal in the channel despite its high surface tension. EGaIn is therefore a suitable metal for microfluidic applications. The ability to inject EGaIn into a microfluidic channel depends on the pressure applied to the metal at the inlet of the channel, and the pressure, in turn, depends on the cross-sectional dimensions of the channel (**Figure 1.10**).<sup>[34]</sup> The relationship between the critical pressure ( $P_c$ ) required to induce flow and the critical dimension can be expressed with the Young's-Laplace equation

$$P_c = 2\gamma \cos \theta \left( \frac{1}{W} + \frac{1}{H} \right)$$

where  $\gamma$  is the effective surface tension,  $\theta$  is the contact angle between the liquid and the walls and  $W$  and  $H$  is the width and height of the channel, respectively. In the absence of the skin, EGaIn has a surface tension of 624 mN/m.<sup>[34, 38]</sup> Phenomenologically, the skin acts like surface tension ( $\sim 0.5$  N/m) in the sense the critical pressure scales inversely with critical dimension; this value is the surface stress that must be exceeded before EGaIn flows. Above

the critical stress, the liquid metal rapidly fills microfluidic channels because of its low viscosity. Below the critical stress, the oxide skin provides mechanical stability to the metal within the channels (i.e., it does not withdraw from the channels). Mercury, in contrast, withdraws from microchannels rapidly to minimize its surface area. In the absence of the oxide skin, EGaIn behaves like mercury and is unstable in microchannels.

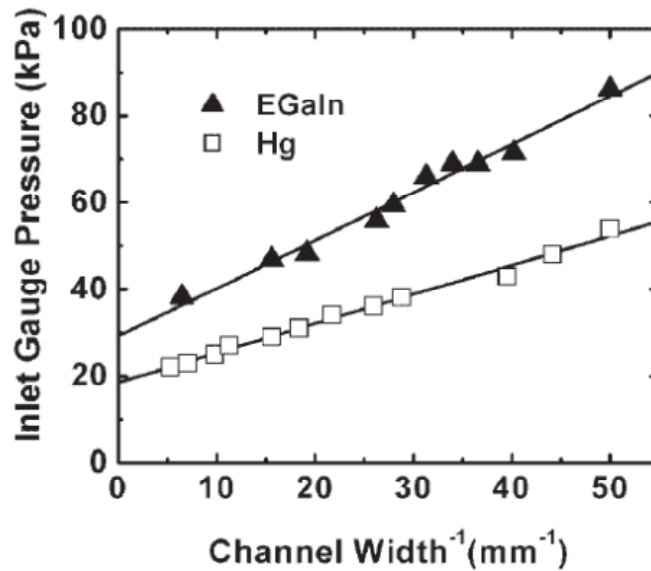


**Figure 1.10** Pressure to fill EGaIn or Hg into microchannels increases as a function of the inverse of the smallest width ( $1/W$ ) of the channel.<sup>[34]</sup>

Micro and nanodroplets of EGaIn can be stabilized by coating the surface of the metal with self assembled monolayers (**Figure 1.11(a)**).<sup>[89]</sup> The molecules on the surface of the metal stabilize the microdroplets and prevents them from coalescing into bigger droplets. Flow focusing using microfluidics offers a simple way to fabricate EGaIn microdroplets (**Figure 1.11(b)**).<sup>[90]</sup> The effect of different channel dimensions, flow rates and types of carrier fluids on the shape and size of the metal microdroplets have been studied. The

droplets form and retain non-spherical shapes in oxygenated silicone oil due to the instantaneous formation of the oxide skin. However, in aqueous poly(ethylene glycol) solution and deoxygenated silicone oil, the metal droplets adopt a spherical geometry to minimize the surface energy. Controlling the formation of metal microdroplets can potentially be used in micro-electro-mechanical system (MEMS) devices for optical and electrical switches, valves and micropumps.

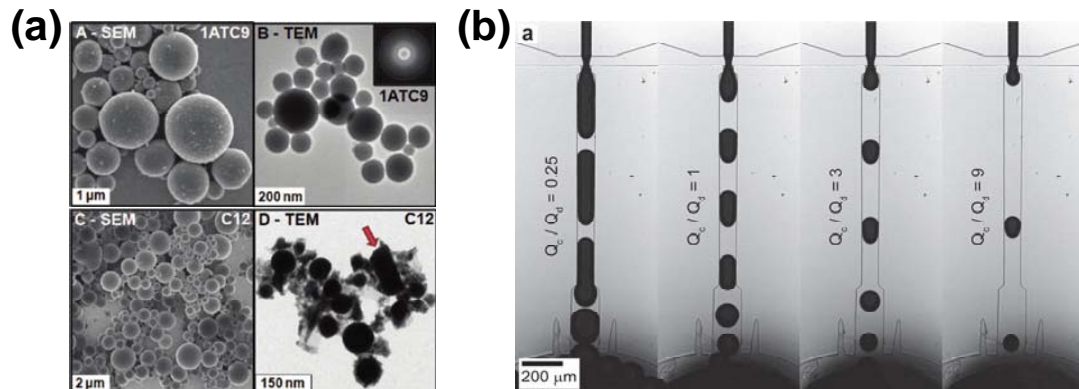


**Figure 1.11** (a) (A, C) EGaIn droplets imaged by scanning electron microscopy (SEM) and (B, D) transmission electron microscopy (TEM). EGaIn dispersed in (A and B) 3-mercaptopropionamide (1ATC9), and (C and D) 1-dodecanethiol (C12).<sup>[89]</sup> (b) EGaIn droplet formation in aqueous PEG solution using a microfluidic device. A series of images shows droplet generation at different flow rate ratios.<sup>[90]</sup>

## 1.5 Motivation and Layout of this Dissertation

Conventional electronics are typically fabricated from rigid materials (e.g., silicon and copper) using expensive processes, such as milling, etching, deposition and photolithography. Inexpensive flexible devices are being developed that enable new applications; examples include flexible solar cells,<sup>[91-94]</sup> textiles with integrated

electronics,<sup>[95-97]</sup> and electronic papers.<sup>[98-101]</sup> While the flexibility of current materials stems from thin-film geometries, the materials cannot be stretched or deformed significantly without inducing irreversible damage. Here, we study a room temperature liquid metal for making metallic components because it flows in response to deformation and thus the mechanical properties of electronic devices composed of the liquid metal depend on the properties of the casing material. In Chapter 2 and 3, we will discuss reconfigurable and mechanically tunable antennas and highly stretchable conductive fibers formed by injecting the liquid metal into elastomeric casings.

In addition to forming stretchable components for electronics, the metal can also be utilized for soft electronics. Although the term soft electronics can have many implications, here we use it to describe electronic devices that are composed entirely from soft materials. This concept is motivated in part by the differences between modern computers and ‘circuits’ found in nature (e.g., the human brain). The brain, for example, is composed of soft materials, has a 3D architecture, operates in an aqueous environment, and uses ions to operate. Computer chips, in contrast, are 2D, rigid, electron-based, and require a dry environment. Furthermore, computer chips have not been able to mimic the operational complexity of the brain. In Chapter 4, we introduce a new class of soft and quasi-liquid electronic memory devices formed by combining the liquid metal and hydrogel doped with polyelectrolyte. The electronic functionality of these devices originates from the ability to control the electronic and ionic transport at the interface between the metal and the hydrogel. The oxide skin of the metal is a wide band-gap semiconductor and the electrical resistance through the oxide skin depends on its thickness. Controlling the thickness by applying

electric bias and/or changing pH of environments offers a new way to control resistance of electric devices. We combine the metal and this operating principle with hydrogels, which are a class of soft materials that are biocompatible and aqueous based.

The mechanical properties of the oxide skin offer new opportunities to create metallic components using fabrication methods that would not be possible with rigid metals. For example, EGaIn is well suited for microfluidic applications since the oxide skin provides mechanical stability to the liquid metal inside microchannels. In Chapter 5, we present liquid metal microelectrodes for integrated microfluidic devices. The metal can be injected into microfluidic channels to produce structures that are self aligned with adjacent microfluidic channels; that is, the channels are produced in the same fabrication step as the microfluidic channels and are therefore inherently aligned. The liquid metal microelectrodes are in direct contact with the microchannel fluid and also span from the bottom to the top of the channel, thus generate an effective electric field in micro-electro systems.

Interfacial tension limits the ability to pattern liquids into arbitrary shapes both in and out of plane. For example, the Rayleigh instability limits the aspect ratio of liquid cylinders to below  $\pi$ . However, the oxide skin allows new opportunities to overcome the destabilizing effects of surface tension. In Chapter 6, we describe printing of the liquid metal into a variety of stable free-standing 3D microstructures such as cylinders with aspect ratios significantly beyond the Rayleigh stability limit, 3D droplet arrays, out of plane arches and wires. Because of the importance of the oxide skin for all of the applications described in this thesis, we sought to study the mechanical and rheological properties.

Although much is known about the metal itself, little is known about the composite oxide-metal system. In Chapter 7, we seek to understand the rheological properties of this system in different chemical environments and exploit them for various applications. This study will produce fundamental understanding of the skin and provide insight for future applications. It also provides some fundamental understanding that complements the other chapters in this thesis. For example, it elucidates the behavior of the metal in contact with water, which occurs in the memristor devices described in Chapter 4.

## 1.6 References

- [1] A. J. Bard, L. R. Faulkner, *Electrochemical Methods: Fundamentals and Applications*, Wiley, New York, **2001**.
- [2] J. H. Christie, J. A. Turner, R. A. Osteryoung, *Anal. Chem.* **1977**, *49*, 1899.
- [3] R. E. Holmlin, R. Haag, M. L. Chabinyo, R. F. Ismagilov, A. E. Cohen, A. Terfort, M. A. Rampi, G. M. Whitesides, *J. Am. Chem. Soc.* **2001**, *123*, 5075.
- [4] T. S. Kasirga, Y. N. Ertas, M. Bayindir, *Appl. Phys. Lett.* **2009**, *95*, 3.
- [5] J. Lee, C. J. Kim, *J. Microelectromech. Syst.* **2000**, *9*, 171.
- [6] K. S. Yun, I. J. Cho, J. U. Bu, C. J. Kim, E. Yoon, *J. Microelectromech. Syst.* **2002**, *11*, 454.
- [7] T. W. Clarkson, L. Magos, G. J. Myers, *N. Engl. J. Med.* **2003**, *349*, 1731.
- [8] M. Valko, H. Morris, M. T. D. Cronin, *Curr. Med. Chem.* **2005**, *12*, 1161.
- [9] B. L. Vallee, D. D. Ulmer, *Annu. Rev. Biochem.* **1972**, *41*, 91.
- [10] R. K. Zalups, *Pharmacol. Rev.* **2000**, *52*, 113.
- [11] J. C. Langer, J. Zou, C. Liu, J. T. Bernhard, *IEEE Microw. Wirel. Co. Lett.* **2003**, *13*, 120.
- [12] D.-Y. Khang, H. Jiang, Y. Huang, J. A. Rogers, *Science* **2006**, *311*, 208.
- [13] Q. Cao, S. H. Hur, Z. T. Zhu, Y. G. Sun, C. J. Wang, M. A. Meitl, M. Shim, J. A. Rogers, *Adv. Mater.* **2006**, *18*, 304.
- [14] Q. Cao, J. A. Rogers, *Adv. Mater.* **2009**, *21*, 29.
- [15] D.-H. Kim, J.-H. Ahn, W. M. Choi, H.-S. Kim, T.-H. Kim, J. Song, Y. Y. Huang, Z. Liu, C. Lu, J. A. Rogers, *Science* **2008**, *320*, 507.
- [16] Y. Sun, J. A. Rogers, *Adv. Mater.* **2007**, *19*, 1897.
- [17] D.-H. Kim, J. A. Rogers, *Adv. Mater.* **2008**, *20*, 4887.
- [18] S. P. Lacour, D. Chan, S. Wagner, T. Li, Z. Suo, *Appl. Phys. Lett.* **2006**, *88*, 204103/1.
- [19] T. Li, Z. Huang, Z. Suo, S. P. Lacour, S. Wagner, *Appl. Phys. Lett.* **2004**, *85*, 3435.

- [20] T. Li, Z. Suo, *Int. J. Solids Struct.* **2006**, *43*, 2351.
- [21] A. C. Siegel, D. A. Bruzewicz, D. B. Weibel, G. M. Whitesides, *Adv. Mater.* **2007**, *19*, 727.
- [22] A. M. Alfantazi, R. R. Moskalyk, *Miner. Eng.* **2003**, *16*, 687.
- [23] M. Abtew, G. Selvaduray, *Mat. Sci. Eng. R.* **2000**, *27*, 95.
- [24] K. Shimizu, T. Nakanishi, K. Karasawa, K. Hashimoto, K. Niwa, *J. Electron. Mater.* **1995**, *24*, 39.
- [25] D. Wojciechowski, J. Vanfleteren, E. Reese, H. W. Hagedorn, *Microelectron. Reliab.* **2000**, *40*, 1215.
- [26] T. G. Leong, P. A. Lester, T. L. Koh, E. K. Call, D. H. Gracias, *Langmuir* **2007**, *23*, 8747.
- [27] A. C. Siegel, S. K. Y. Tang, C. A. Nijhuis, M. Hashimoto, S. T. Phillips, M. D. Dickey, G. M. Whitesides, *Accounts Chem. Res.* **2010**, *43*, 518.
- [28] S. S. Shevkoplyas, A. C. Siegel, R. M. Westervelt, M. G. Prentiss, G. M. Whitesides, *Lab Chip* **2007**, *7*, 1294.
- [29] A. C. Siegel, S. S. Shevkoplyas, D. B. Weibel, D. A. Bruzewicz, A. W. Martinez, G. M. Whitesides, *Angew. Chem Int. Edit.* **2006**, *45*, 6877.
- [30] L. J. Briggs, *J. Chem. Phys.* **1957**, *26*, 784.
- [31] I. A. Sheka, I. S. Chaus, T. T. Mitiureva, *The Chemistry of Gallium*, Elsevier, New York, **1966**.
- [32] S. J. French, D. J. Saunders, G. W. Ingle, *J. Phys. Chem.* **1938**, *42*, 265.
- [33] V. Y. Prokhorenko, V. V. Roshchupkin, M. A. Pokrasin, S. V. Prokhorenko, V. V. Kotov, *High Temp.* **2000**, *38*, 954.
- [34] M. D. Dickey, R. C. Chiechi, R. J. Larsen, E. A. Weiss, D. A. Weitz, G. M. Whitesides, *Adv. Funct. Mater.* **2008**, *18*, 1097.
- [35] R. J. Larsen, M. D. Dickey, G. M. Whitesides, D. A. Weitz, *J. Rheol.* **2009**, *53*, 1305.
- [36] T. Y. Liu, P. Sen, C. Kim, *J. Microelectromech. Syst.* **2012**, *21*, 443.

- [37] T. Y. Liu, P. Sen, C. J. Kim, IEEE, in *Mems 2010: 23rd IEEE International Conference on Micro Electro Mechanical Systems, Technical Digest*, IEEE, New York **2010**, 560.
- [38] D. Zrnica, D. S. Swatik, *J. Less-Common Metals* **1969**, *18*, 67.
- [39] S. Cheng, A. Rydberg, K. Hjort, Z. Wu, *Appl. Phys. Lett.* **2009**, *94*, 144103.
- [40] G. J. Hayes, J. H. So, A. Qusba, M. D. Dickey, G. Lazzi, *IEEE Trans. Antennas Propag.* **2012**, *60*, 2151.
- [41] M. R. Khan, G. J. Hayes, J.-H. So, G. Lazzi, M. D. Dickey, *Appl. Phys. Lett.* **2011**, *99*, 013501.
- [42] M. Kubo, X. Li, C. Kim, M. Hashimoto, B. J. Wiley, D. Ham, G. M. Whitesides, *Adv. Mater.* **2010**, *22*, 2749.
- [43] M. Kubo, X. F. Li, C. Kim, M. Hashimoto, B. J. Wiley, D. Ham, G. M. Whitesides, IEEE, in *2011 IEEE 61st Electronic Components and Technology Conference*, **2011**, 1582.
- [44] S. J. Mazlouman, X. J. Jiang, A. Mahanfar, C. Menon, R. G. Vaughan, *IEEE Trans. Antennas Propag.* **2011**, *59*, 4406.
- [45] J.-H. So, J. Thelen, A. Qusba, G. J. Hayes, G. Lazzi, M. D. Dickey, *Adv. Funct. Mater.* **2009**, *19*, 3632.
- [46] Y. L. Park, B. R. Chen, R. J. Wood, *IEEE Sens. J.* **2012**, *12*, 2711.
- [47] Y. L. Park, C. Majidi, R. Kramer, P. Berard, R. J. Wood, *J. Micromech. Microeng.* **2010**, *20*.
- [48] R. D. P. Wong, J. D. Posner, V. J. Santos, *Sens. Actuator A-Phys.* **2012**, *179*, 62.
- [49] H.-J. Kim, C. Son, B. Ziaie, *Appl. Phys. Lett.* **2008**, *92*, 011904/1.
- [50] R. C. Chiechi, E. A. Weiss, M. D. Dickey, G. M. Whitesides, *Angew. Chem., Int. Ed.* **2008**, *47*, 142.
- [51] C. A. Nijhuis, W. F. Reus, G. M. Whitesides, *J. Am. Chem. Soc.* **2009**, *131*, 17814.
- [52] D. Fracasso, H. Valkenier, J. C. Hummelen, G. C. Solomon, R. C. Chiechi, *J. Am. Chem. Soc.* **2011**, *133*, 9556.
- [53] C. A. Nijhuis, W. F. Reus, A. C. Siegel, G. M. Whitesides, *J. Am. Chem. Soc.* **2011**, *133*, 15397.

- [54] M. M. Thuo, W. F. Reus, C. A. Nijhuis, J. R. Barber, C. Kim, M. D. Schulz, G. M. Whitesides, *J. Am. Chem. Soc.* **2011**, *133*, 2962.
- [55] L. Cademartiri, M. M. Thuo, C. A. Nijhuis, W. F. Reus, S. Tricard, J. R. Barber, R. N. S. Sodhi, P. Brodersen, C. Kim, R. C. Chiechi, G. M. Whitesides, *J. Phys. Chem. C* **2012**, *116*, 10848.
- [56] J. Q. Wang, S. C. Liu, A. Nahata, *Opt. Express* **2012**, *20*, 12119.
- [57] J.-H. So, M. D. Dickey, *Lab Chip* **2011**, *11*, 905.
- [58] H. Channaa, P. Surmann, *Pharmazie* **2009**, *64*, 161.
- [59] B. L. Mellor, N. A. Kellis, B. A. Mazzeo, *Rev. Sci. Instrum.* **2011**, *82*.
- [60] H.-J. Koo, J.-H. So, M. D. Dickey, O. D. Velev, *Adv. Mater.* **2011**, *23*, 3559.
- [61] A. Du Pasquier, S. Miller, M. Chhowalla, *Sol. Energ. Mat. Sol. C* **2006**, *90*, 1828.
- [62] D. J. Lipomi, R. C. Chiechi, W. F. Reus, G. M. Whitesides, *Adv. Funct. Mater.* **2008**, *18*, 3469.
- [63] D. J. Lipomi, B. C. K. Tee, M. Vosgueritchian, Z. Bao, *Adv. Mater.* **2011**, *23*, 1771.
- [64] I. Silverman, A. L. Yarin, S. N. Reznik, A. Arenshtam, D. Kijet, A. Nagler, *Int. J. Heat Mass Tran.* **2006**, *49*, 2782.
- [65] C. Majidi, R. Kramer, R. J. Wood, *Smart Mater. Struct.* **2011**, *20*.
- [66] P. Surmann, H. Zeyat, *Anal. Bioanal. Chem.* **2005**, *383*, 1009.
- [67] M. Knoblauch, J. M. Hibberd, J. C. Gray, A. J. E. van Bel, *Nat. Biotechnol.* **1999**, *17*, 906.
- [68] O. J. Cayre, S. T. Chang, O. D. Velev, *J. Am. Chem. Soc.* **2007**, *129*, 10801.
- [69] H.-J. Koo, S. T. Chang, J. M. Slocik, R. R. Naik, O. D. Velev, *J. Mater. Chem.* **2011**, *21*, 72.
- [70] H.-J. Koo, S. T. Chang, O. D. Velev, *Small* **2010**, *6*, 1393.
- [71] N. A. Peppas, J. Z. Hilt, A. Khademhosseini, R. Langer, *Adv. Mater.* **2006**, *18*, 1345.
- [72] J. N. Koster, *Cryst. Res. Technol.* **1999**, *34*, 1129.

- [73] D. R. Lide, *CRC Handbook of Chemistry and Physics*, Taylor and Francis, FL, Boca Raton **2007**.
- [74] L. R. Bernstein, *Pharmacol. Rev.* **1998**, *50*, 665.
- [75] M. K. Chaffin, V. Fajt, R. J. Martens, C. E. Arnold, N. D. Cohen, M. O'Connor, R. J. Taylor, L. R. Bernstein, *J. Vet. Pharmacol. Ther.* **2010**, *33*, 376.
- [76] C. R. Chitambar, *Expert Opin. Inv. Drug.* **2004**, *13*, 531.
- [77] C. R. Chitambar, D. P. Purpi, *Leukemia Res.* **2010**, *34*, 950.
- [78] B. Desoize, *Anticancer Res.* **2004**, *24*, 1529.
- [79] M. Frezza, C. N. Verani, D. Chen, Q. P. Dou, *Lett. Drug Des. Discov.* **2007**, *4*, 311.
- [80] J. Goncalves, N. Wasif, D. Esposito, J. M. Coico, B. Schwartz, P. J. Higgins, R. S. Bockman, L. Staiano-Coico, *J. Surg. Res.* **2002**, *103*, 134.
- [81] Y. Kaneko, M. Thoendel, O. Olakanmi, B. E. Britigan, P. K. Singh, *J. Clin. Invest.* **2007**, *117*, 877.
- [82] S. P. Valappil, D. Ready, E. A. Abou Neel, D. M. Pickup, L. A. O'Dell, W. Chrzanowski, J. Pratten, R. J. Newport, M. E. Smith, M. Wilson, J. C. Knowles, *Acta Biomater.* **2009**, *5*, 1198.
- [83] M. J. Regan, P. S. Pershan, O. M. Magnussen, B. M. Ocko, M. Deutsch, L. E. Berman, *Phys. Rev. B* **1997**, *55*, 15874.
- [84] P. S. Pershan, *J. Phys. Chem. B* **2009**, *113*, 3639.
- [85] P. S. Pershan, *Eur. Phys. J.-Spec. Top.* **2011**, *196*, 109.
- [86] F. Scharmann, G. Cherkashinin, V. Breternitz, C. Knedlik, G. Hartung, T. Weber, J. A. Schaefer, *Surf. Interface Anal.* **2004**, *36*, 981.
- [87] Q. Xu, N. Oudalov, Q. Guo, H. M. Jaeger, E. Brown, *Phys. Fluids* **2012**, *24*, 063101.
- [88] M. Pourbaix, *Atlas of Electrochemical Equilibria in Aqueous Solutions - Gallium*, Vol. 16.1, National Association of Corrosion Engineers, Houston, Texas, USA **1974**.
- [89] J. N. Hohman, M. Kim, G. A. Wadsworth, H. R. Bednar, J. Jiang, M. A. LeThai, P. S. Weiss, *Nano Lett.* **2011**, *11*, 5104.
- [90] T. Hutter, W. A. C. Bauer, S. R. Elliott, W. T. S. Huck, *Adv. Funct. Mater.* **2012**, *22*, 2624.

- [91] D. Kuang, J. Brillet, P. Chen, M. Takata, S. Uchida, H. Miura, K. Sumioka, S. M. Zakeeruddin, M. Graetzel, *Acs Nano* **2008**, *2*, 1113.
- [92] Z. Fan, H. Razavi, J.-w. Do, A. Moriwaki, O. Ergen, Y.-L. Chueh, P. W. Leu, J. C. Ho, T. Takahashi, L. A. Reichertz, S. Neale, K. Yu, M. Wu, J. W. Ager, A. Javey, *Nat. Mater.* **2009**, *8*, 648.
- [93] F. C. Krebs, S. A. Gevorgyan, J. Alstrup, *J. Mater. Chem.* **2009**, *19*, 5442.
- [94] F. C. Krebs, M. Jorgensen, K. Norrman, O. Hagemann, J. Alstrup, T. D. Nielsen, J. Fyenbo, K. Larsen, J. Kristensen, *Sol. Energ. Mater. Sol. C.* **2009**, *93*, 422.
- [95] D. Marculescu, R. Marculescu, N. H. Zamora, P. Stanley-Marbell, P. K. Khosla, S. Park, S. Jayaraman, S. Jung, C. Lauterbach, W. Weber, T. Kirstein, D. Cottet, J. Grzyb, G. Troster, M. Jones, T. Martin, Z. Nakad, *P. IEEE* **2003**, *91*, 1995.
- [96] R. F. Service, *Science* **2003**, *301*, 909.
- [97] M. Hamedi, R. Forchheimer, O. Inganas, *Nat. Mater.* **2007**, *6*, 357.
- [98] B. Comiskey, J. D. Albert, H. Yoshizawa, J. Jacobson, *Nature* **1998**, *394*, 253.
- [99] J. A. Rogers, Z. Bao, K. Baldwin, A. Dodabalapur, B. Crone, V. R. Raju, V. Kuck, H. Katz, K. Amundson, J. Ewing, P. Drzaic, *P. Natl. Acad. Sci. USA* **2001**, *98*, 4835.
- [100] Y. Chen, J. Au, P. Kazlas, A. Ritenour, H. Gates, M. McCreary, *Nature* **2003**, *423*, 136.
- [101] A. C. Siegel, S. T. Phillips, M. D. Dickey, N. Lu, Z. Suo, G. M. Whitesides, *Adv. Funct. Mater.* **2010**, *20*, 28.

## **Chapter 2. Reversibly Deformable and Mechanically Tunable Fluidic Antennas\***

---

\* This chapter is partially based on J.-H. So, J. Thelen, A. Qusba, G. J. Hayes, G. Lazzi, M. D. Dickey. *Adv. Funct. Mater.*, 2009, 19, 3632 and G. J. Hayes, J.-H. So, A. Qusba, M.D. Dickey, G. Lazzi, *IEEE Trans. Antennas Propag.*, 2012, 60, 2151.

## 2.1 Introduction

This chapter describes a simple technique to fabricate reversibly-deformable and mechanically-tunable antennas by injecting a liquid metal alloy into elastomeric microfluidic channels. The metal, eutectic gallium indium (EGaIn, 75 %, Ga 25 % In by weight, m.p.=15.7 °C<sup>[1]</sup>), fills the channels rapidly at room temperature and possesses a thin oxide “skin” that keeps the fluid mechanically stable inside of the channels despite the high surface energy of the metal.<sup>[2]</sup> We fabricated the channels using soft lithography,<sup>[3]</sup> a rapid prototyping method capable of producing antennas without any milling or etching. The elastomeric channels define the mechanical properties of the antenna since the metal is a low viscosity fluid. Unlike conventional copper antennas, the fluidic antennas resist permanent deformation (i.e., the antennas return to their original state after removal of an applied stress) and can thus be deformed (stretched, bent, rolled, and twisted) reversibly without any hysteresis. The fluid metal ensures electrical continuity during deformation and “self-heals” in response to small cuts. Having a radiation efficiency of ~90% over a broad frequency range (1910 to 1990 MHz), these fluidic antennas are as efficient as conventional dipole antennas with solid metallic elements. In addition, the resonant frequency of the antenna can be mechanically tuned by elongating (i.e., stretching) the elastomer, and can therefore act as a wireless sensor of strain. The fluidic antennas have the potential to enhance the emerging field of flexible electronics by enabling wireless communication capabilities. We demonstrate, characterize, and model the capabilities of these fluidic dipole antennas.

## 2.2 Background

The rapid growth of applications requiring wireless communication or remote sensing has created demand for advances in antenna technologies. We sought to fabricate antennas that are highly flexible, stretchable, and reversibly deformable. Flexible antennas have the potential to enhance the emerging field of flexible electronics, which is primarily motivated by the desire to incorporate electronics into flexible substrates such as textiles, displays, and bandages. The ability to reversibly deform antennas may also enable new capabilities (e.g., rolling and unrolling for remote deployment, enhanced durability) and the ability to reconfigure the shape of an antenna mechanically (e.g., by elongation) provides a means of tuning its spectral response or sensing external forces. Bendable antennas are also of interest for “smart antenna” applications; that is, beam-forming and beam-bending antennas. These devices are useful in millimeter-wave applications (e.g., automotive radars, security and surveillance systems, and high-data rate wireless communication systems).<sup>[4]</sup> Mechanically scanned antennas—that is, devices in which a portion of the antenna is designed to bend out of plane—are being explored for these applications because they are less expensive, more efficient, and offer better control than electronic phase shifting arrays.<sup>[4-7]</sup>

Most conventional antennas are fabricated by milling or etching rigid sheets of copper into a static shape that dictates a singular function. Copper forms efficient antennas, but is poorly suited for flexible electronics because it fatigues when bent repeatedly and undergoes irreversible plastic deformation beyond strains of  $\sim 2\%$ .<sup>[8]</sup> Thin inorganic films<sup>[9, 10]</sup> and semiconducting organic polymers<sup>[11-13]</sup> are the primary materials used for flexible electronic applications. These materials, however, are limited in the extent to which they can be

stretched and do not exhibit the electrical properties required for efficient antennas. Flexible electronics have been formed by encasing thin coils of metallic wire in an elastomer.<sup>[14-20]</sup> These approaches take advantage of the ability to bend metals with sufficiently small cross-sections. Unfortunately, when thin films of metal are stretched they can form micro-cracks<sup>[21]</sup> or deform.<sup>[22, 23]</sup> The use of coils also imposes an unnecessary design constraint for antennas and increases the complexity of fabrication.

Polydimethylsiloxane (PDMS), a silicone elastomer with a low Young's modulus (< 2 MPa), has recently been used as a supporting substrate for copper to make flexible antennas.<sup>[4]</sup> The mechanical properties of the device are defined by those of the copper (Young's modulus ~130 GPa). Although the antenna can be bent slightly, it is not designed to be deformed (twisted, rolled, stretched) without inducing irreversible deformation or fatigue.

We sought to fully utilize the deformability of the PDMS substrate by replacing the solid metal components with a fluid metal, thus allowing significant deformation of the antennas as governed by the mechanical properties of the elastomeric substrate, rather than that of a solid metal. Importantly, the liquid metal has a thin, solid-like oxide skin on its surface that is well suited for microfluidics. The liquid metal fills microchannels rapidly at room temperature when the pressure applied to the inlet exceeds the force required to rupture the skin. Once the metal is inside the channel, the skin reforms and provides mechanical stability to the otherwise low-viscosity and high surface tension liquid (Hg, in contrast, withdraws from microchannels rapidly to minimize its surface area).<sup>[2]</sup> The use of fluid metal allows the elastomeric antenna to be deformed (stretched, bent, flexed, or rolled)

significantly and reversibly without loss of electrical continuity; the resulting antennas are therefore durable. The fluid can flow in response to elongation of the elastomer, resulting in a reconfiguration of the geometry of the antenna and thus a shift in the resonant frequency. We demonstrate that the fluid metal forms highly efficient antennas that can be tuned via mechanical elongation without any hysteresis.

### **2.3 Experimental Design**

We chose to fabricate a dipole antenna because the simplicity of the design allows changes in geometry (and thus resonant frequency) during stretching to be interpreted easily. The dipole structure can also be simulated numerically under multiple operating conditions using finite element method (FEM) modeling. Typically, the metallic elements of conventional planar copper antennas are fabricated by mechanical stamping and forming of a sheet of metal or through a sequential multi-step process of plating a conductive layer of copper on a dielectric substrate, etching the desired antenna element, and milling the antenna assembly from the host dielectric substrate. As a result, the rapid generation of large sets of prototype antennas may incur a significant cost. We fabricated the antenna by injecting fluid metal into an elastomeric microfluidic channel formed by a soft-lithographic process based on replica molding.<sup>[3]</sup> This fabrication method allows for rapid prototyping of new antenna designs and a single “master” can be replicated to produce many identical antennas.

We used PDMS (Sylgard 184 kit, Dow Corning) as the antenna substrate. PDMS is a commercial elastomer that is used routinely for preparing microfluidic channels.<sup>[24]</sup> PDMS is highly elastic, and possesses a low modulus and low surface energy; these properties enable

it to conform to surfaces. PDMS has a low dielectric constant (2.67) and a high loss tangent (0.0375).<sup>[25]</sup> Dipole antennas, however, do not have resonant fields within the surrounding dielectric and therefore the field densities inside the PDMS are low. PDMS is thus a suitable casing for dipole antennas.<sup>[4]</sup>

We used EGaIn as the conductive element of the antenna, which has several advantages compared with other conductive materials such as water, solder, or mercury. Microfluidic channels are typically used to manipulate aqueous solutions. Although saline water is electrically conductive, it is poorly suited for antenna formation because it can evaporate and the conductivity is relatively low compared to metals. Mercury could be used to fill the channels, but it is toxic and its high surface energy prevents it from forming mechanically stable structures (i.e., mercury withdraws from the channel to minimize its surface area).<sup>[2]</sup> EGaIn is a low viscosity (approximately twice the viscosity of water) liquid metal alloy at room temperature with a relatively high conductivity ( $\sigma=3.4\times 10^5 \text{ Scm}^{-1}$  <sup>[26, 27]</sup>). For comparison, the conductivity of copper at room temperature is  $5.96\times 10^5 \text{ Scm}^{-1}$ .<sup>[28]</sup> Unlike solder, EGaIn does not need to be heated prior to injection and it maintains its fluidity after injection, which is critical to maintain continuity during deformation. Unlike mercury, EGaIn has a low level of toxicity<sup>[28]</sup> and is well-suited for forming conductive and mechanically stable structures in microfluidic channels.<sup>[2, 29]</sup> The thin passivating oxide layer (i.e., it does not grow thicker with time)<sup>[30, 31]</sup> that forms on EGaIn provides mechanical stability to the liquid metal such that it can maintain its non-spherical structure in the microfluidic channels despite its high surface tension. EGaIn is therefore a suitable metal for microfluidic applications.

## 2.4 Fabrication and Characterization of Dipole Antennas

We fabricated dipole antennas by injecting EGaIn into PDMS microchannels. A dipole antenna consists of two conductive rods of equal length that are aligned along their long axis and separated by an insulating gap. A dipole resonates with a wavelength,  $\lambda$ , that is approximately twice that of the total antenna length,  $L$  ( $\lambda = 2L$ ) and is inversely proportional to the resonant frequency ( $\lambda = cv^{-1}$ , where  $v$  is the resonant frequency, and  $c$  is the speed of light). The total length of the antenna ( $\sim 54$  mm) was chosen so that it resonates at a frequency ( $\sim 2$  GHz) within the range of the detector.

Figure 2.1a is a schematic diagram of the process used for fabricating a fluidic dipole antenna. We used photolithography to generate a “master” pattern of the dipole on a silicon wafer using a negative photoresist (SU-8, Microchem). The pattern consisted of two  $150\ \mu\text{m}$  thick (as verified by profilometry),  $25.4$  mm long, and  $0.5$  mm wide lines aligned along their long axis and separated by  $2$  mm. Curing a PDMS pre-polymer against this topographically patterned substrate (i.e., replica molding)<sup>[31]</sup> produced an inverse replica of the master. After exposure of the replica to an oxygen plasma, we sealed it to a flat PDMS substrate ( $\sim 1$  mm thick), producing a microfluidic channel into which we injected the liquid metal. An additional thin-layer of PDMS sealed the inlet and outlet holes of the channel to assist with handling.

An Agilent E5071B ENA series network analyzer measured the spectral properties of the antenna. We used a balanced-to-unbalanced (balun) transformer to convert the “unbalanced” (i.e., grounded) coaxial cable from the network analyzer to the “balanced” (i.e., ungrounded) antenna.<sup>[32]</sup> The input to the balun is a coaxial connection and the output is a

pair of balanced electrical leads. Solder typically connects the leads from the balun to copper antennas, but in this case, the leads could simply be inserted into the fluidic antenna elements. The network analyzer transmits incident electromagnetic waves into the antenna and measures the amount of energy reflected back to the analyzer as a function of frequency. The reflection coefficient,  $\Gamma$  or  $S_{11}$ , is the ratio of the reflected voltage divided by the incident voltage. For each frequency in the sweep, the network analyzer calculates the reflection coefficient. In decibels, the reflection coefficient, or return loss, is  $-20 \log |\Gamma|$  where  $|\Gamma|$  is the magnitude of the complex reflection coefficient. The frequency with the lowest return loss is the resonant frequency.

We characterized the spectral properties and efficiency of the fluidic antenna in the “free space” position (i.e., not stretched or clamped). The antenna resonated at approximately 1962 MHz with ~90% radiation efficiency as measured by a far-field, anechoic chamber. The radiation efficiency is defined as the ratio of total power radiated by the antenna to the power delivered to the input of the antenna. An efficiency of 100% implies that all of the input power is radiated by the antennas without any losses. An efficiency of 90% is expected for a similar dipole with solid metallic elements. These results, therefore, indicate that the electrical losses of EGaIn within PDMS channels are insignificant.

The fluidic antennas can be deformed reversibly (stretched, bent, rolled, wrapped, folded) without any loss of electrical continuity (cf Figures 2.1b-2.1c). We characterized the spectral characteristics of the antenna before and after deforming the antenna in the following ways: (1) stretching (up to 40% strain); (2) twisting along the long axis by 90 degrees; (3) folding in half; and (4) rolling. Without exception, the antenna exhibited the same spectral

response before and after deformation. Furthermore, the resonant frequency did not change significantly during deformation. These observations demonstrate that the fluidic antennas are reversibly deformable and suggest that they are durable because of the lack of hysteresis.

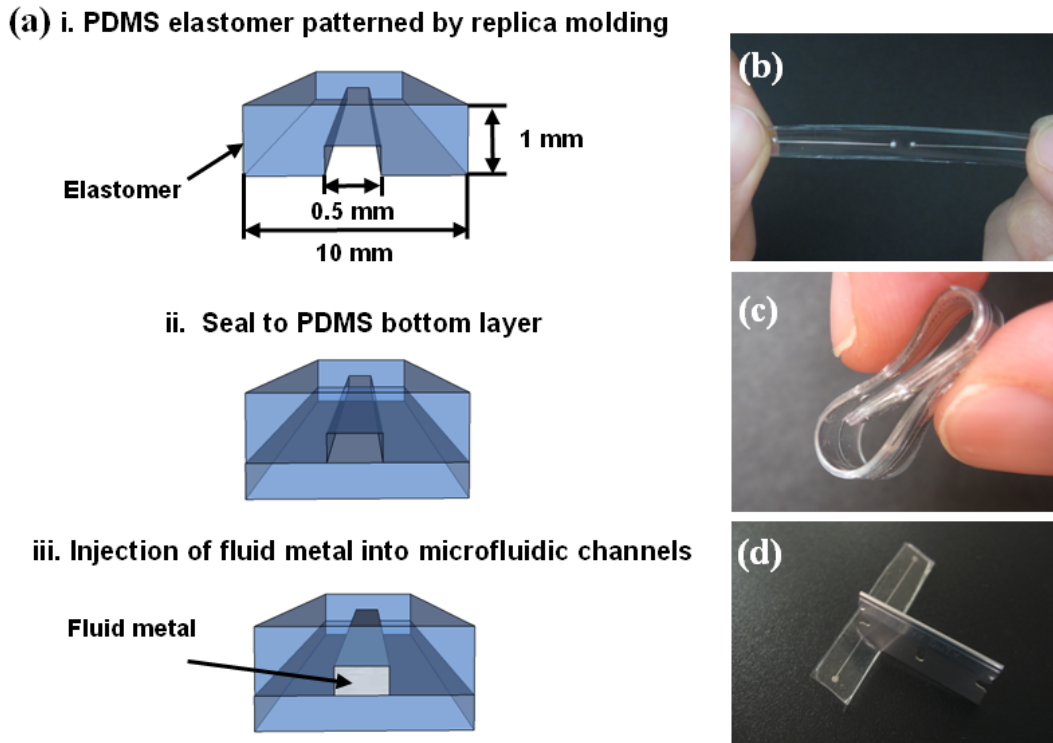


**Figure 2.1** (a) Fabrication process of a reversibly deformable dipole antenna. PDMS elastomer cured on a topographically-patterned substrate produces two adjacent microfluidic channels (only one shown). After sealing the PDMS channels to another piece of PDMS, injection of liquid metal alloy into the microfluidic channels produces a dipole antenna. (b-c) Photographs of a prototype antenna being stretched and rolled. There is no hysteresis in the spectral properties of the antenna as it is returned to the “relaxed” state. (d) The antenna self-heals in response to sharp cuts, such as those inflicted by a razor blade.

The fluidic antennas self-healed (that is, they retained their conductivity) after being cut with a razor blade. We cut entirely through the metal portion of the antenna (perpendicular to the long axis), as shown in Figure 2.1(d), but left some of the PDMS

surrounding the antenna intact. After removing the razor blade, the electrical resistance through the antenna returned to its pre-cut value. Stretching the antenna slightly expanded the gap formed at the site of the cut and caused the resistance to be infinite. Within the gap, it was apparent that the razor blade created two distinct metal-air interfaces, suggesting that the metal remained flush with the cut interface (i.e., it did not reflow into or out of the channel). Observation of these exposed interfaces by optical microscopy showed that the oxide skin gets pinned at the edges of the opening in the channel created by the razor blade. When we relaxed the antenna, it returned to its original conducting state. The process of re-breaking (by stretching the antenna and thereby separating the metal interfaces in the cut region) and reconnecting the wire could be repeated. In contrast to previous work, which has shown that discontinuities in wires in microfluidic channels composed of solder can be healed by heating and sonication,<sup>[33]</sup> the fluidic antennas heal spontaneously. We were able to get the two metal interfaces to merge into a continuous element by intentionally pressing on the channels. As a control experiment, we embedded a thin copper wire (with similar cross sectional area to the antenna) in PDMS and measured the electrical resistance before and after cutting through it with a razor blade. Approximately 40% of the time the wire returned to a conductive state, and 60% of the time the resistance was infinite. These results suggest that while the elasticity of the PDMS is primarily responsible for reconnecting the broken wires, the soft interface of the fluidic antenna facilitates reliable healing.

We hypothesized that elongating an (uncut) antenna by stretching (Figure 2.2) the elastomeric device would shift the resonant frequency towards lower frequencies. We built an apparatus to stretch the antenna to minimize human bias in the measurements. The device

contained no metal parts to avoid electronic coupling with the antenna and thus simplify the interpretation of the results. The device consisted of two clamps composed of plastic (Delrin) onto which we affixed each end of the antenna. The clamps slid along glass rods parallel to the long axis of the antenna. Plastic screws exerted the force required to elongate the antenna in a controlled manner. A picture of the clamping fixture is shown in Figure 2.3.

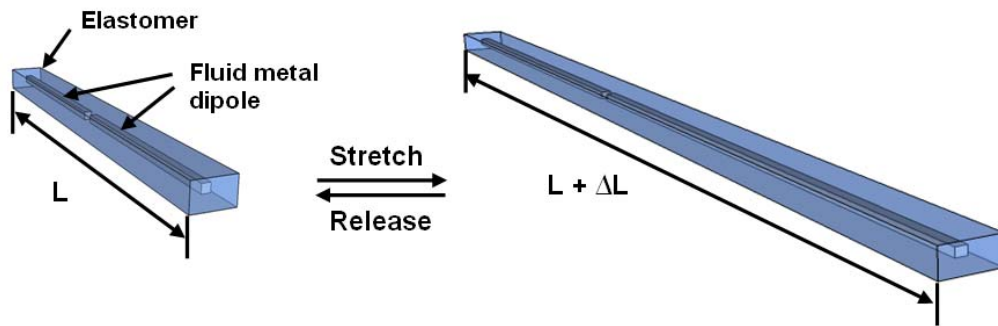


**Figure 2.2** A schematic depiction of a dipole antenna before and after being stretched. The ability to stretch the antenna improves its overall durability and allows it to sense strain by the modulation of the spectral response during elongation.

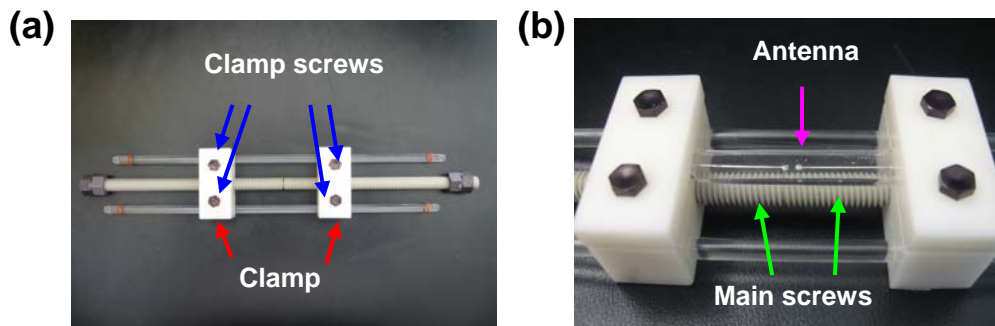


**Figure 2.3.** Photographs of the device used to stretch the fluidic antenna. (a) Two clamps with four screws secure each end of the antenna and slide parallel to the long axis of the antenna. (b) The dipole fluidic antenna mounted in the device. Two main screws exerted the required force to push the clamps away from each other; this motion caused the antenna to elongate in a controlled manner.

We stretched the antenna from 54 mm to 66 mm (defined as the total end-to-end length of the metal in the antenna) by increments of 2 mm. We chose this range because it minimized the chances of tearing the device (discussed below) and thereby enabled the measurement of hysteresis in the device during strain relaxation (from 66 mm back to 54 mm). The liquid metal in the elastomer maintained its electrical continuity during stretching. Although the cross-sectional area of the antenna reduces during elongation to maintain its total volume (the Poisson ratio of PDMS is 0.5<sup>[34]</sup>), the length of the metal is directly proportional to the length of elastomer.

Figure 2.4 shows that elongating the antenna modulates the spectral response; the antennas can therefore sense strain. We determined the resonance frequency of the antennas using the radio frequency network analyzer. A reflection coefficient (or return loss) below -10 dB is considered sufficient for effective radiation in commercial antennas. We recorded the spectral response as a function of the length of the antenna (measured using calipers) at 2 mm increments, but only plotted four series in Figure 2.4 for clarity. The resonant frequency at 56, 60, and 64 mm follow the same trends as those in Figure 2.4.

Stretching the antenna beyond ~75 mm caused it to tear (~40 % elongation at break). The theoretical extent of elongation depends on the type of PDMS and the way in which it is prepared.<sup>[35, 36]</sup> In principle, PDMS can be stretched beyond 40% strain, but it is likely that the antennas failed prematurely because of small defects at the surface of the PDMS that focused the applied stress. The antennas typically failed in regions of the PDMS that had been compromised or cut during fabrication.

Figure 2.4 shows that the antennas behave as true dipole antennas in the frequency range predicted from simple scaling ( $\sim 2$  GHz). As expected, the resonant frequency of the antenna decreased with increasing antenna length (Figure 2.5). The resonant frequency measured during the release of the applied strain did not exhibit any hysteresis. This result illustrates that the antenna is reversibly stretchable and the resonant frequency is indicative of the length of the antenna regardless of whether strain is increasing or decreasing.

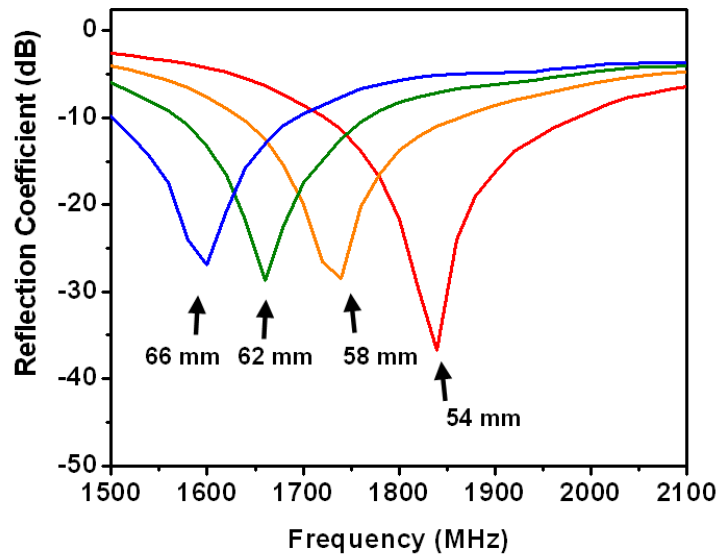


**Figure 2.4** A plot of the measured reflection coefficient of the dipole both in its “relaxed” position (54 mm length) and mechanically elongated positions (58, 62, and 66 mm length) as a function of frequency. The ability to stretch the antenna allows the frequency to be tuned mechanically.

We used a FEM simulator to model the resonant frequency of the dipole antenna as a function of induced strain. A computer-aided design (CAD) file input into the simulator identified the physical geometries and electric properties of each element within and surrounding the antenna. The FEM simulator generated a complex mesh of elements over the

antenna and iteratively optimized an approximate solution to Maxwell's equations over the mesh until it achieved a solution with a sufficiently low error value. The model accounted for the geometry of the dipole (as a function of strain), the presence of the PDMS dielectric, and the surrounding clamping fixture. Figure 2.5 presents the simulated resonance frequency with the measured resonance frequency. The difference between the simulated and measured resonance frequencies is insignificant ( $\pm 0.1$ - $0.3$  % at each point).

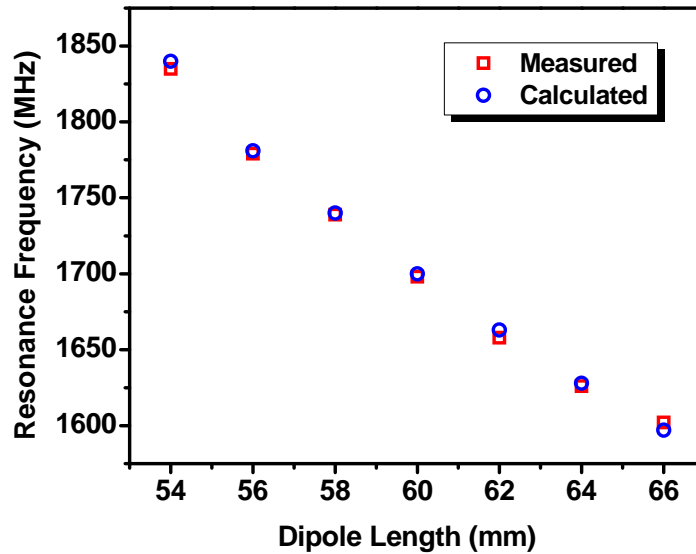


**Figure 2.5** Resonant frequency of a fluidic dipole antenna as a function of the length of the antenna as modulated by stretching. The calculated values were modeled using finite element modeling.

## 2.5 Fabrication and Characterization of Microstrip Patch Antennas

Antennas with radiating elements that have narrow cross sections (such as a dipole) have proven to be straight forward to fabricate reliably by simply injecting the metal into microchannels shaped with the desired geometry. In contrast, the conductive elements (i.e.,

radiating element and ground layer) of the patch antenna resemble a large, flat rectangle. Channels with cross-sections that have small aspect ratios (i.e., a small height relative to the width) present at least two challenges. First, the channels tend to collapse because of the low modulus of the PDMS, which is an important attribute of the polymer that allows it to flex easily. Second, we found it challenging to inject the metal uniformly into low aspect ratio channels without creating pockets of air bubbles or uneven filling. This problem is exacerbated by the critical yield stress behavior of EGaIn; that is, it flows readily only when the pressure is large enough to rupture the skin and therefore does not necessarily flow evenly in every direction.

We overcame these challenges by designing microchannel geometries that guide the metal to fill the wide, rectangular geometry of the patch antenna uniformly by taking advantage of the rheological properties of EGaIn described in Chapter 1.2 with Young's-Laplace equation. As shown in Figure 2.6, we designed a serpentine pathway of posts with constant height ( $H$ ,  $100\ \mu\text{m}$ ) in which the distance between two neighboring posts ( $W_2$ ,  $100\ \mu\text{m}$ ) is much smaller than the width of the serpentine channel ( $W_1$ ,  $1000\ \mu\text{m}$ ). The critical pressure required to inject the metal through the channel ( $P_{c1}$ ) is therefore less than that required to inject it through the posts ( $P_{c2}$ ). In this implementation, the ratio of the two critical pressures is approximately 2:1; that is, it takes nearly twice as much pressure to force the metal between the posts than through the channels. The liquid metal therefore flows selectively through the serpentine-shaped channel (rather than between the posts) and thereby fills the entire area of the antenna. The posts also prevent the channel from collapsing. Once the metal fills the serpentine pathway completely, the pressure is increased (e.g., by simply

pressing on the top of the antenna by hand) to force the metal between the posts to merge, as shown in Figure 2.7. The patch antennas could be flexed without significant change in performance.<sup>[37]</sup>

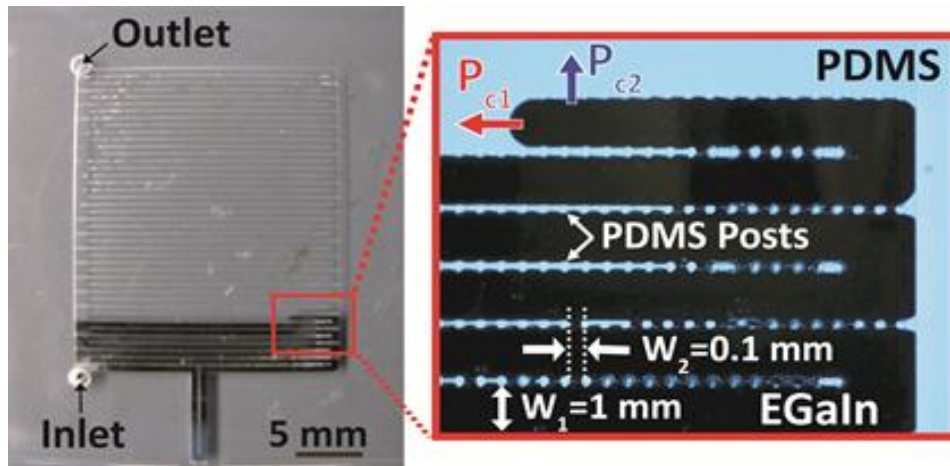


**Figure 2.6** Photograph of a partially filled patch antenna taken as the liquid metal fills the antenna in a serpentine fashion to ensure uniform and complete filling of the patch geometry. (right) A close-up micrograph of the leading edge of the liquid.

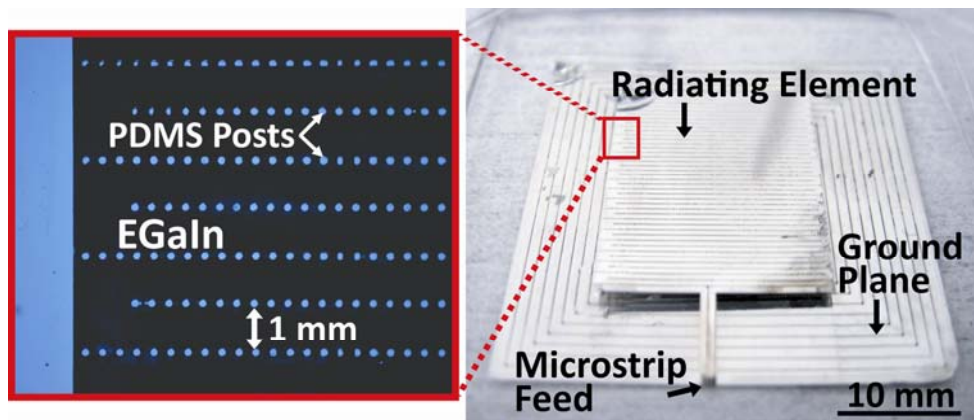


**Figure 2.7** Photograph of a complete, evenly filled patch antenna and ground plane. (left) A close-up micrograph of a representative region of the radiating element shows the PDMS posts and the evenly filled liquid metal.

## 2.6 Advantages of Fluidic Antennas

Relative to conventional copper antennas, fluidic antennas have several advantages: (1) The antennas are reversibly deformable and durable. The elastomeric casing defines the mechanical properties of the antenna and the fluid metal flows in response to deformation to ensure electrical continuity. (2) The fluidic antennas are mechanically tunable and sensitive to strain. (3) The liquid metal forms contacts with the baluns at room temperature without soldering. (4) The antenna self-heals in response to sharp cuts. (5) The fabrication of the antenna by soft-lithography is simple and many antennas can be produced from a single lithographic master.

An additional attractive feature of fluidic antennas is the new ways in which they can be integrated into devices. We envision two general strategies. In the first approach, the fluidic antenna (casing plus liquid metal) is fabricated *ex situ* and subsequently integrated with a device. For example, the low modulus and low surface energy of PDMS allows the fluidic antennas to conform to numerous surfaces and substrates.<sup>[3]</sup> The flexibility of the antennas could also enable them to be wound or woven into devices. In the second approach, the fluid antenna is fabricated *in situ* by injecting liquid metal into conduits that are part of the larger device structure. For example, microfluidic channels formed by sealing a mold (c.f. Figure 2.1) onto a substrate or capillaries in monolithic structures could be filled with liquid metal to form the fluidic antennas. The latter approach is distinguished from conventional approaches because the metallic elements are introduced in an additive manner and can be formed on demand by fluid injection. The ability of the liquid metal to form electrical

contacts without solder or wire bonding further simplifies the integration of these antennas into devices.

## **2.7 Limitations**

While the use of PDMS enables deformability, it is not ideal for situations that require static antennas. This problem can be overcome by placing the antenna on a solid support, which is facilitated by the conformable nature of the PDMS elastomer. There are also limits on the extent to which PDMS can be stretched. The fluidic antenna tore into two pieces after ~40% strain; this value could be increased with optimized design and minimization of defects in the PDMS that otherwise focus stress, or by exploring other elastomers. The use of a fluid metal could also be worrisome for cases in which the antenna is severely damaged. Fortunately, the small amount of EGaIn in the antenna does not flow readily in the absence of a large driving force because of the presence of the mechanically-stabilizing oxide skin. For example, EGaIn did not leak or spray out of the device when the antenna ripped beyond 40% strain nor did it flow when cut in half, as evidenced by the self-healing properties.

## **2.8 Conclusions**

By injecting fluid metal into elastomeric microfluidic channels, we have demonstrated a simple method to produce highly deformable and mechanically tunable antennas. The fluidic dipole antennas radiated with 90% efficiency and displayed a resonant frequency in excellent agreement with theoretical modeling. The shape of the antenna was reconfigurable and the resonant frequency could be tuned mechanically by elongating the antenna via stretching

without hysteresis upon relaxation. This property may be useful for sensing strain wirelessly (e.g., sensing the expansion and contraction of bridges, or the detection of motion). We also demonstrated a novel, multi-layer microstrip patch antenna composed of liquid metal that is mechanically flexible. The thickness of the elastomer could be tuned to change the mechanical properties of the antenna and thereby change the amount of strain induced by a given stress. Fluidic antennas can also withstand mechanical deformation without damage and self-heal when cut. The flexibility of the antenna may allow it to be incorporated into specialized products, such as electronic fabric, without loss of ergonomic functionality, or to be rolled up for remote deployment. Fluidic antennas also have the potential to enhance the emerging field of flexible electronics by providing new sensing or wireless communication capabilities. The ability of the fluid metal to alloy with many metals could facilitate the direct electrical connection and incorporation of antennas onto substrates featuring electronic components.

## 2.9 References

- [1] S. J. French, D. J. Saunders, G. W. Ingle, *J. Phys. Chem.* **1938**, 42, 265.
- [2] M. D. Dickey, R. C. Chiechi, R. J. Larsen, E. A. Weiss, D. A. Weitz, G. M. Whitesides, *Adv. Funct. Mater.* **2008**, 18, 1097.
- [3] Y. Xia, G. M. Whitesides, *Angew. Chem., Int. Ed.* **1998**, 37, 550.
- [4] N. Tiercelin, P. Coquet, R. Sauleau, V. Senez, H. Fujita, *J. Micromech. Microeng.* **2006**, 16, 2389.
- [5] C.-W. Baek, S. Song, J.-H. Park, S. Lee, J.-M. Kim, W. Choi, C. Cheon, Y.-K. Kim, Y. Kwon, *IEEE Trans. Microwave Theory Tech.* **2003**, 51, 325.
- [6] G. DeJean, R. Bairavasubramanian, D. Thompson, G. E. Ponchak, M. M. Tentzeris, J. Papapolymerou, *IEEE Antennas Wirel. Propag. Lett.* **2005**, 4, 22.
- [7] J. C. Langer, J. Zou, C. Liu, J. T. Bernhard, *IEEE Microwave Compon. Lett.* **2003**, 13, 120.
- [8] C. M. Kuo, C. H. Lin, Y. C. Huang, *Mater. Sci. Eng., A* **2005**, 396, 360.
- [9] D.-Y. Khang, H. Jiang, Y. Huang, J. A. Rogers, *Science* **2006**, 311, 208.
- [10] Y. Sun, J. A. Rogers, *Adv. Mater.* **2007**, 19, 1897.
- [11] J. Unsworth, C. Conn, Z. Jin, A. Kaynak, R. Ediriweera, P. Innis, N. Booth, *J. Intell. Mater. Syst. Struct.* **1994**, 5, 595.
- [12] S. Yang, E. Ruckenstein, *Synth. Met.* **1993**, 60, 249.
- [13] F. Zhang, O. Inganaes, *Opt. Sci. Eng.* **2005**, 99, 479.
- [14] S. Befahy, S. Yunus, T. Pardoen, P. Bertrand, M. Troosters, *Appl. Phys. Lett.* **2007**, 91, 141911/1.
- [15] D. Brosteaux, F. Axisa, M. Gonzalez, J. Vanfleteren, *IEEE Electron Device Lett.* **2007**, 28, 552.
- [16] M. Gonzalez, F. Axisa, M. V. Bulcke, D. Brosteaux, B. Vandeveld, J. Vanfleteren, *Microelectron. Reliab.* **2008**, 48, 825.
- [17] D. S. Gray, J. Tien, C. S. Chen, *Adv. Mater.* **2004**, 16, 477.

- [18] B. Huyghe, H. Rogier, J. Vanfleteren, F. Axisa, *IEEE Trans. Adv. Packag.* **2008**, *31*, 802.
- [19] M. S. Miller, G. J. E. Davidson, B. J. Sahli, C. M. Mailloux, T. B. Carmichael, *Adv. Mater.* **2008**, *20*, 59.
- [20] R. Morent, N. De Geyter, F. Axisa, N. De Smet, L. Gengembre, E. De Leersnyder, C. Leys, J. Vanfleteren, M. Rymarczyk-Machal, E. Schacht, E. Payen, *J. Phys. D: Appl. Phys.* **2007**, *40*, 7392.
- [21] S. P. Lacour, D. Chan, S. Wagner, T. Li, Z. Suo, *Appl. Phys. Lett.* **2006**, *88*, 204103/1.
- [22] T. Li, Z. Huang, Z. Suo, S. P. Lacour, S. Wagner, *Appl. Phys. Lett.* **2004**, *85*, 3435.
- [23] T. Li, Z. Suo, *Int. J. Solids Struct.* **2006**, *43*, 2351.
- [24] J. C. McDonald, D. C. Duffy, J. R. Anderson, D. T. Chiu, H. Wu, O. J. A. Schueller, G. M. Whitesides, *Electrophoresis*, **2000**, *21*, 27.
- [25] J. C. Lotters, W. Olthuis, P. H. Veltink, P. Bergveld, *J. Micromech. Microeng.* **1997**, *7*, 145.
- [26] R. C. Chiechi, E. A. Weiss, M. D. Dickey, G. M. Whitesides, *Angew. Chem., Int. Ed.* **2008**, *47*, 142.
- [27] D. Zrnic, D. S. Swatik, *J. Less-Common Metals* **1969**, *18*, 67.
- [28] D. R. Lide, *CRC Handbook of Chemistry and Physics*, Taylor and Francis, FL, Boca Raton **2007**.
- [29] H.-J. Kim, C. Son, B. Ziaie, *Appl. Phys. Lett.* **2008**, *92*, 011904/1.
- [30] M. J. Regan, P. S. Pershan, O. M. Magnussen, B. M. Ocko, M. Deutsch, L. E. Berman, *Phys. Rev. B* **1997**, *55*, 15874.
- [31] M. J. Regan, H. Tostmann, P. S. Pershan, O. M. Magnussen, E. DiMasi, B. M. Ocko, M. Deutsch, *Phys. Rev. B* **1997**, *55*, 10786.
- [32] The two radiating elements of the dipole antenna are electrically “balanced” (i.e. neither lead is connected to electrical ground). In contrast, the coaxial cable from the network analyzer is electrically “unbalanced” with the outer conductor of the coaxial line being electrically grounded. For simplicity, we used a common quarter-wavelength coaxial balun.

- [33] A. C. Siegel, D. A. Bruzewicz, D. B. Weibel, G. M. Whitesides, *Adv. Mater.* **2007**, *19*, 727.
- [34] J. E. Mark, *The Polymer Data Handbook*, Oxford Univ. Press, New York **1999**.
- [35] K. M. Choi, J. A. Rogers, *J. Am. Chem. Soc.* **2003**, *125*, 4060.
- [36] X. Ye, H. Liu, Y. Ding, H. Li, B. Lu, *Microelectronic Engineering* **2009**, *86*, 310.
- [37] G. J. Hayes, J.-H. So, A. Qusba, M. D. Dickey, G. Lazzi, *IEEE Trans. Antennas Propag.* **2012**, *60*, 2151

**Chapter 3. Ultrastretchable Fibers with Metallic Conductivity  
Using a Liquid Metal Alloy Core**

### 3.1 Introduction

This chapter describes the fabrication and characterization of ultra-stretchable fibers with metallic conductivity formed by injecting a moldable liquid metal into hollow elastomeric fibers. We fabricated the hollow fibers by melt processing commercial elastomers (Kraton G1643). Injecting a liquid metal alloy, eutectic gallium indium (EGaIn, 75% Ga, 25% In by weight, melting point  $15.7^{\circ}\text{C}^{[1, 2]}$ ), into these fibers produces conductive wires encased in an insulating polymer shell. Because the metal is a liquid at room temperature, it is capable of maintaining electrical continuity while stretching the fibers significantly ( $\sim 800\%$  strain). Stretchable and flexible conductive fibers are important for a number of applications, including stretchable electronics, electret filtration, and electronic textiles. Conventional electronics are fabricated typically from rigid materials (e.g., silicon, copper, aluminum). Flexible electronics are motivated, in part, by the ability to incorporate electronic function into non-rigid substrates (e.g., textiles, filters, clothing, chapter, sensors).<sup>[3-5]</sup> Stretchable electronics furthers the concept of flexible electronics and enables the electronics to be used in more mechanically demanding applications. Here, we focus on stretchable conductors, which are useful for wires, interconnects, meta-materials, and antennas.

Conductive fibers are an attractive platform for flexible and stretchable electronics because fibers are inexpensive, inherently flexible, compatible with fabrics, and can be mass produced via melt processing with very high speeds ( $>1000$  m/min). The most common methods to impart conductivity into melt processed fibers include coating the fibers with conductive films (e.g., metals or carbon)<sup>[6-8]</sup> or creating conductive composites by introducing electrically conductive additives (e.g., graphite or carbon,<sup>[9-12]</sup> metal

nanoparticles,<sup>[13]</sup> conductive polymers<sup>[11, 14-17]</sup> such as polyaniline and poly 3-hexylthiophene). The composite method requires including enough additive to exceed a percolation threshold to ensure conductivity through the fiber. Thus, the mechanical properties (modulus, toughness, tactility, yield point) of the fiber change in unintended ways; coating methods have similar effects. Moreover, the composite fibers rarely results in metallic conductivity and conductive polymers tend to degrade due to oxidation.<sup>[6, 18]</sup> In some applications (e.g., commercial wires), it may be undesirable to have the current carrying components exposed to the exterior of the fiber. Commercial wires (e.g., copper wire insulated with polymer) are flexible due to their thin cross-section, but are not stretchable.<sup>[19, 20]</sup> We sought to demonstrate a new approach to create conductive fibers that would be simple, highly conductive, and stretchable without modifying the mechanical or tactile properties of the fiber. The present work is distinguished by (1) the ability of the fibers to maintain metallic conductivity with ultra-large strains, (2) the geometry of the fiber (a conductive core surrounded by an insulating shell, which is similar to conventional wires), and (3) the mechanical and tactile properties of the fiber, which are altered minimally since the fiber shell is unadulterated polymer.

We fabricated the fibers by injecting a moldable liquid metal into hollow fibers. The metal, EGaIn, is liquid at room temperature with a low viscosity and a high conductivity ( $\sigma = 3.4 \times 10^4$  S/cm<sup>[21]</sup>). The liquid metal forms spontaneously a thin oxide skin at room temperature that reforms rapidly when ruptured. The metal can be injected into capillaries, microchannels, and hollow fibers by exceeding the pressure required to rupture the skin.<sup>[2]</sup> Once it is in the capillary, a new skin forms rapidly and holds it into place. This ability to

mold the metal into non-spherical shapes has been utilized to fabricate microelectrodes,<sup>[22]</sup> stretchable antennas,<sup>[23-25]</sup> soft diodes<sup>[26]</sup> and flexible solar cells.<sup>[27]</sup> Here, we harness this property to form ultra-stretchable, conductive wires inside hollow elastomeric fibers.

Poly[styrene-*b*-(ethylene-co-butylene)-*b*-styrene] (SEBS) resin is a thermoplastic elastomer with low modulus, high tensile strength (stress at break ~10.34 MPa), high stretchability (strain at break >600%), and good resistance to most chemicals.<sup>[28]</sup> SEBS resins are used widely in the production of handles and grips, medical equipment, roofing and many other applications due to their rubber-like properties. We chose one type of SEBS resin, Kraton G1643 because it is commercially available, highly stretchable (strain at break >900%) and easy to melt process. This particular resin consists of 20% styrene endblocks and 80% ethylene-butylene midblock.<sup>[28]</sup> Here, we describe the fabrication and characterization of stretchable conductive fibers and demonstrate their function as a stretchable charger for electronic devices and as a stretchable cable for earphones.

## **3.2 Experimental**

### **3.2.1 Fabrication of hollow fibers**

We fabricated the hollow fibers by a melt drawing process because it is a widely used technique in the non-wovens industry. We used a pilot scale Fuji Filter Melt Spinning Tester (MST-CII Special Type). The instrument melt extruded the polymer resin at 230 °C and 400 psi through a hollow configured die. The die consisted of a circular slit divided into three equal sections. The circle had an outer diameter of 2 mm and inner diameter of 1.5 mm. The slits were 3 mm deep and the sections were separated by 0.2 mm. A series of rollers

mechanically drew the extruded hollow fibers through a water bath at room temperature to cool the fibers and the final roller collected them and dictated the “spinning rate”. We varied the quench distance (i.e., the distance from the die to the water bath) between 20” and 38”, as well as the speed of the gear pump that meters the polymer (between 20 and 47 rpm). These changes had minimal effects on the fiber dimensions. Taken in sum, these results suggest that other methods may be necessary to make even smaller fibers (e.g., different die dimensions).

### **3.2.2 Injection of liquid metal**

We injected the liquid metal into the hollow fibers to fabricate stretchable conductive fibers. A needle on a syringe filled with the liquid metal and threaded into the fiber provided the source of the conductive core of conductive fibers. For cases in which the gauge of the needle was larger than the diameter of the fiber, we inserted the fiber into the needle and sealed it with glue so that the syringe would force the metal into the fiber.

### **3.2.3 Mechanical Characterization**

We measured the mechanical properties of both hollow and filled fibers with different dimensions using an Instron 5943. Two hydraulic grips held one inch sections of fiber and stretched it at a constant rate of 10 cm/min. A computer recorded the gauge length between the two grips throughout the entire experiment process and converted it into pressure with the available cross-sectional area of the material in each test sample.

### 3.2.4 Electrical Characterization

A customized digitally controlled stretcher extended the conductive fibers at 1 mm/s while measuring the resistance using a four point probe measurement. Copper wire inserted into both open ends of the fibers provided electrical connections between the liquid metal and the probe clamps from the source meter. We measured the resistance of these wires to be 13.4 m $\Omega$ , which agrees with the theoretical value based on the resistivity of copper and the physical dimensions of the wires. To prevent any slippage that might occur during fiber stretching, we assembled loose loops of the fiber at each end of the conductive fibers. The loops had a diameter of about 0.25" while leaving a 1" straight section in between the loops as the effective original sample length. A drop of glue encased the loops and the copper wire connections, and their resistance was subtracted from the overall resistance measurement to isolate the contributions from the stretchable portion of the fiber. A four point probe technique using a Keithley 2400 measured the overall resistance (through the copper wires, loops, and stretchable portion of the fiber).

### 3.3 Results

We produced hollow fibers by melt extruding SEBS through a die consisting of a circular slit divided into three equal segments. The fibers exited the extruder in a downward motion (i.e., in the direction of gravity) and a collection roller dictated the speed with which the fibers were drawn through a water bath at room temperature. To control the dimensions of the hollow fibers, we varied the spinning rate of the collection roller. **Figure 3.1** shows the cross sectional dimensions of the fibers for spinning rates ranging from 25 to 1000 m/min. In all

cases, the fibers have a triangular cross section, which is most likely due to the shape of the die. The fibers tended to have a slightly more circular shape at slower spinning rates. The inner diameter of the fabricated fiber varied from 400 to 800 microns (we define the inner diameter as the average of the length of the three lines that originate from the vertexes and bisect the triangular cross-section of the core of the fiber) and the thickness of the walls of the fiber ranges from 100 to 200  $\mu\text{m}$ . As expected, faster spinning rates produce smaller fibers. The fiber geometry appears to level out at higher spinning rates. We varied several processing parameters, but did not observe significant changes in fiber geometry.

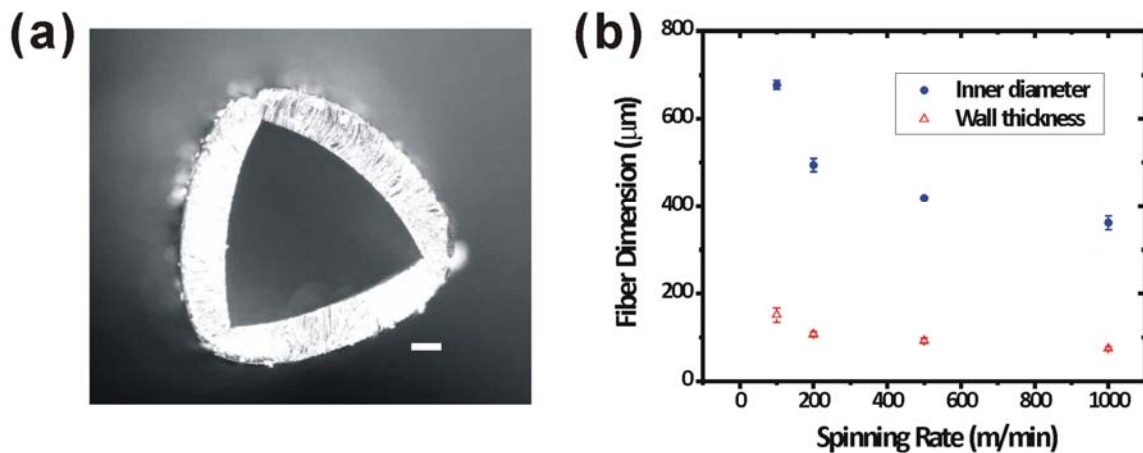


**Figure 3.1** (a) Optical image of the cross-section of a hollow fiber. (b) The inner diameter (ID) and wall thickness (WT) of the fibers decrease with spinning rate.

It is straightforward to inject the metal into the hollow fibers. A long segment of hollow fiber can be filled with liquid metal using a syringe and then cut into several pieces with desired lengths. The oxidized skin of the metal prevents the metal from flowing out of

the fiber when the fiber is not disturbed (e.g., squeezed significantly). The inset in **Figure 3.2(a)** shows that the metal remains flush with the cut end of the fiber.

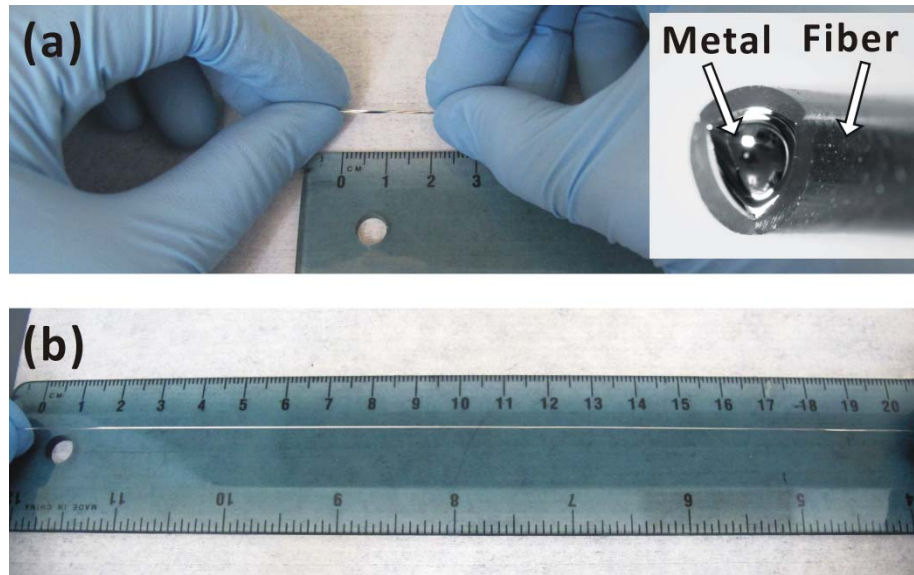


**Figure 3.2** (a) A relaxed, 2 cm section of an ultra-stretchable conductive fiber. The shiny core of its cross-section (inset) is the liquid metal. (b) The fiber is stretched to 20 cm and the metal appears to uniformly fill the stretched fiber.

We hypothesized that the incorporation of the metal impacts minimally the mechanical properties of the fibers since the metal is a low viscosity liquid and flows readily in response to applied strain. We measured the mechanical properties of both the hollow and filled fibers using an Instron. **Figure 3.3** shows the stress-strain profiles of the fibers for two spinning rates spanning an order of magnitude in spin speed (100 m/min and 1000 m/min). The profile shows the typical properties of thermoplastic elastomers: low modulus and high tensile strength. Fibers made with the lowest spinning rate can be strained the furthest before

the point of failure. At the lowest spinning rate (100 m/min), we found that the fibers could be stretched to 800-1000% strain before reaching the point of failure (with an ultimate strength of ~14 MPa). Figure 3.3 shows that the fibers with and without the metal have nearly identical mechanical properties, which illustrates the negligible effects of the liquid metal on the mechanical properties of the fibers.

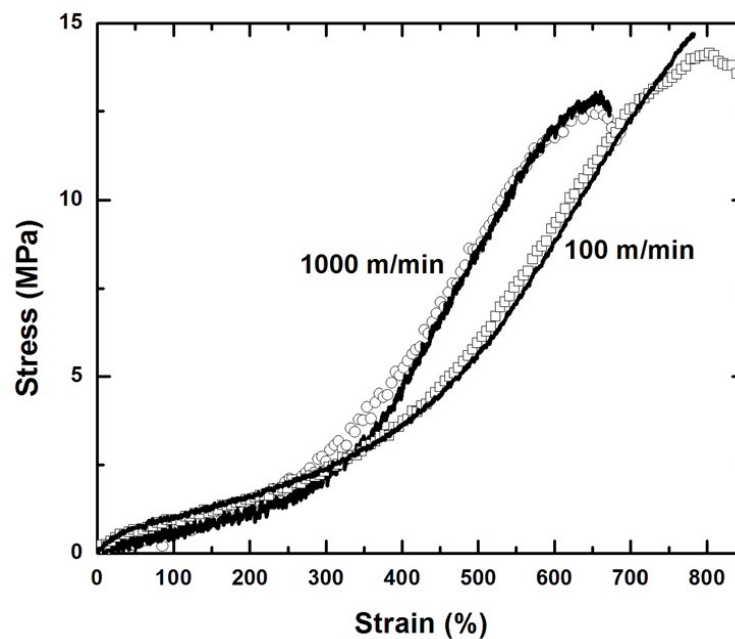


**Figure 3.3** The strain-stress plots of elastomeric hollow (hollow symbols) and filled (solid lines) fibers with two different spinning rates. The fibers have the same mechanical properties with and without the metal.

For any stretchable electronics application, a consideration is the effect of multiple strain cycles on the performance of the fiber. We performed cyclic testing on the fibers to quantify the effects of repeated strain on the mechanical properties. **Figure 3.4** shows that

after the first cycle (0 to 800 to 0% strain), subsequent strain cycles overlap nearly perfectly with minimal signs of hysteresis. After the first cycle, there is ~50% unrecoverable strain (i.e., the “set”) and each subsequent cycle has a similar set. This result suggests there is some plastic deformation during the first strain cycle, but negligible plastic deformation during subsequent cycles. Similar behavior was observed for fibers fabricated with other spinning rates.

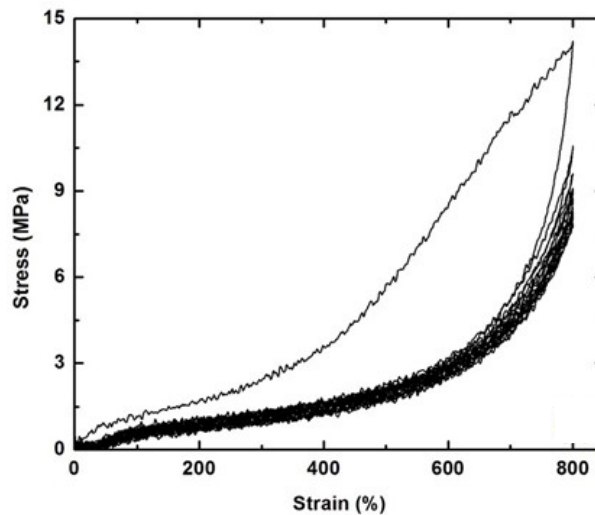


**Figure 3.4** Cycling test on the mechanical properties of the hollow fibers fabricated with a spinning rate of 1000 m/min. Beyond the first cycle (largest stress), the fibers show minimal signs of mechanical hysteresis.

We sought to assess the electrical performance of the ultra-stretchable fibers during elongation. It is expected that the electrical resistance of the fiber should increase as a function of applied strain since the length of the fiber increases while the cross-sectional area decreases with elongation. We measured the resistance as a function of strain and normalized

all measurements by the resistance at zero strain such that the initial normalized resistance is 1. The resistance  $R$  of a wire depends on its resistivity  $\rho$ , length  $L$ , and cross-sectional area  $A$ , as shown in Pouillet's law. If we assume a Poisson's ratio of 0.5 and the metal is incompressible, then the resistance of the fiber should be proportional to the change in the square of the length from a purely geometric perspective. We note, however, that decreasing spinning rates tend to shift the cross sectional area from triangular to a more circular shape. We developed two sets of theoretical resistance values: one is based on the assumption that the cross-sectional area remains triangular while stretching and the other one assumes it becomes circular (i.e., for a given circumference, the cross-sectional area is 60% larger for a circle than an equilateral triangle and thus, the resistance through a circular cross section should be lower). The experimental data, in principle, should be within these bounds for the given assumptions. **Figure 3.5** shows that the resistance increases as a function of strain. We repeated these measurements at least three times for each fiber with large and small cross sectional areas (i.e., 100 and 1000 m/min) and the test results are reproducible for both sizes. The fibers with a smaller cross sectional area (1000 m/min) have an electrical resistance that agrees nearly perfectly with that predicted by the model for a triangular cross sectional area. The fibers with a larger cross sectional area (100 m/min) have an electrical resistance similar to the theoretical resistance for a triangular cross section until ~200% strain and starts to deviate to lower values and follows the model for a circular cross-section until 700-800% strain, at which point the resistance rises rapidly and ultimately loses conductivity. In most cases, we observe that the loss of conductivity coincides with the physical collapse of the fibers. Our best sample (100 m/min) maintained conductivity to 1000% strain, but we chose

to plot more conservative values. The conductivity recovers upon returning the fibers back to a non-stressed state (in some cases, massaging the fibers is required to regain continuity). To investigate how the spinning rate affects the discrepancy between the measured values and the two theoretical models, we embedded the 100 and 1000 m/min fibers in UV curable epoxy while applying 200 % strain and observed the cross section of the fibers after cutting it in half. The cross section of the fiber with 100 m/min spinning rate becomes circular with strain while the fibers with 1000 m/min spinning rate maintain their triangular cross section. We speculate that the stability of the cross-sectional profile of the fibers at higher spinning rates (compared to those at lower rates) could be associated with the stiffer mechanical properties, the more triangular initial geometry, or the smaller size (e.g., increasing the circumference of the fiber should make the side walls easier to deform). Sources of error in our measurements include experimental variability and uncertainty in the fiber geometry, minor slippage of the fiber from the clamps, potential void space in the metal or non-uniform constriction of the non-circular cross-section. Regardless, the model captures the general trends and suggests that the resistance is less than or equal to that expected from a triangular shaped fiber. We emphasize that the key advance is the remarkable conductivity at large strains and only offer speculation that the triangular cross section may have the added benefit of lowering the relative electrical resistance due to the effective enlargement of the cross sectional area of the fiber as it elongates. Because the conductivity is metallic, the results match the most conductive composite fibers in the literature.<sup>[29]</sup> The elongation also matches the best stretchable fibers in the literature.<sup>[16]</sup>

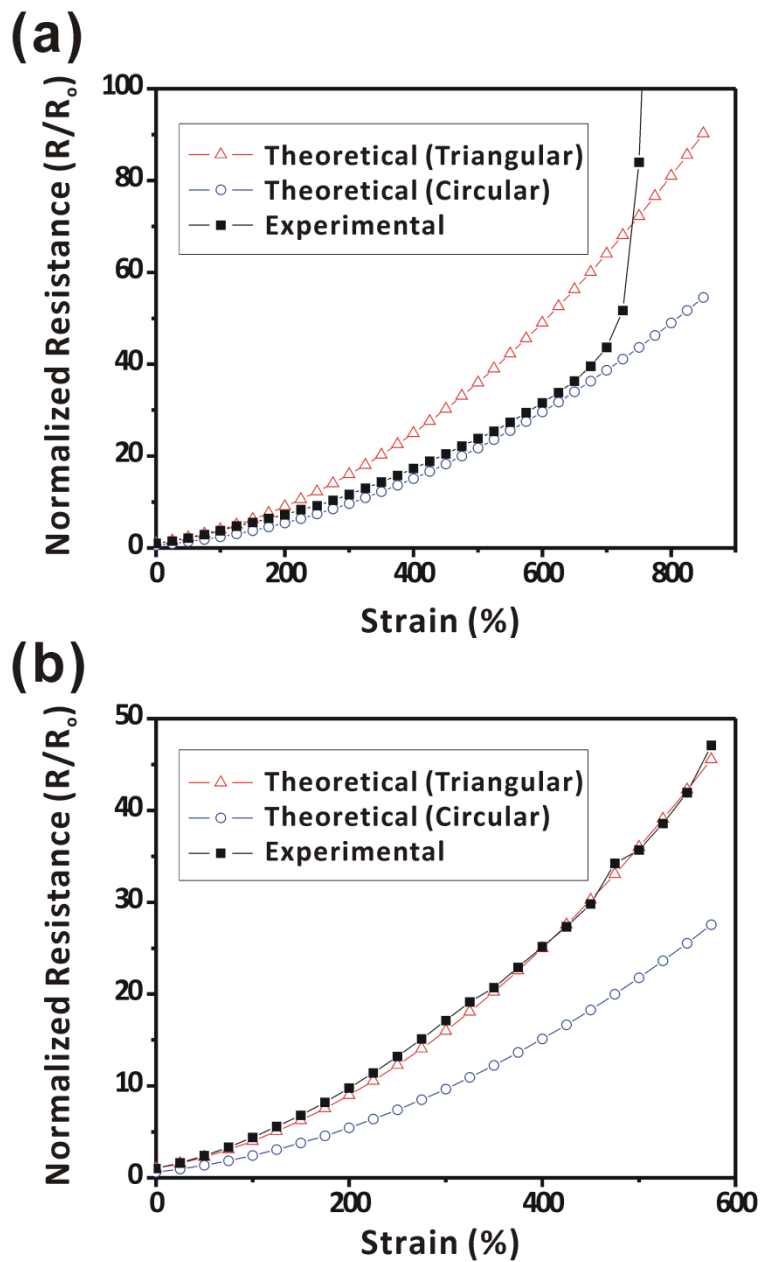


**Figure 3.5** The experimental (filled squares) and two sets of theoretical resistance (empty triangles and circles) of conductive fibers with two different spinning rates of (a) 100 and (b) 1000 m/min. The resistance increases as the applied strain increases.

A potential drawback of a liquid core encased in an elastomeric shell is that the metal can flow and increase its resistance when pinched. We performed some qualitative experiments to emulate conditions the fiber may encounter during handling. We pinched the 100m/min fiber between our fingers and found the resistance to increase by an order of magnitude, but not lose electrical continuity. The resistance returned to its initial value when we ceased to pinch the fiber. We also observed that the resistance increased two orders of magnitude, but did not lose its electrical continuity when pinched using more concentrated pressure from our finger nails. It recovered to its pre-pinched value after releasing the force and massaging the fiber. These qualitative experiments suggest that it is challenging to completely eliminate electrical continuity by hand when the fiber is in the rest state.

To demonstrate the stretchable fibers in electronic applications, we utilized the fibers as wires of a charger and earphones for an iPod. We cut a portion of a iPod charger line and inserted four stretchable fibers (two power wires and two data transmission wires) as shown in **Figure 3.6(a)**. The iPod began charging when connected to a computer through the stretchable charger, and maintained the mode while we repeatedly stretched and relaxed the fibers. We also inserted the fibers to replace a portion of the wires for earphones (Figure 3.6(b)) and the earphones continued to play music as well as the unmodified earphone even when elongated.

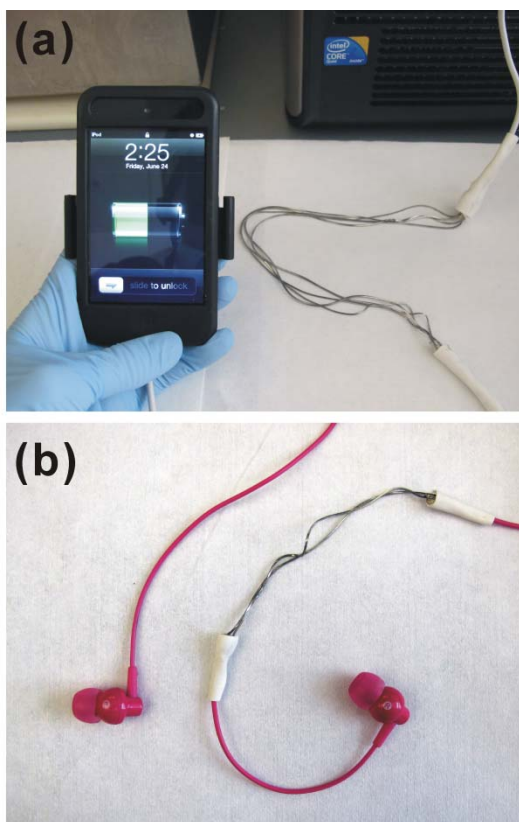


**Figure 3.6** (a) Stretchable charger for electronic devices and (b) stretchable cable for earphones.

### 3.4 Conclusion

This study provides an alternative approach to generate ultra-stretchable conductive fibers by simply injecting liquid alloy (EGaIn) into hollow polymer (Kraton SEBS) fibers. The dimensions of the conductive fibers can be manipulated readily by varying the spinning rate of collecting rollers during the melt spinning process. The fibers have the same mechanical and tactile properties with and without the metal. Metallic electrical continuity can be maintained to greater than 800% strain depending on the dimensions of the fiber, which we believe represents one of the best combinations of conductivity and stretchability for

conductive fibers reported to date. The triangular cross section of the fibers appears to have an unexpected benefit of decreasing the relative resistance while elongating the fiber due to changes in the cross sectional area. The conductive fibers can be incorporated into numerous applications including flexible electronics, smart garments, stretchable wires, inductors, interconnects, and antennas. The mechanical properties of the fibers here are limited only by the properties of the polymer, which in principle could be rendered even more stretchable (with less hysteresis) by the incorporation of block-selective oils.<sup>[30]</sup>

### 3.5 References

- [1] S. J. French, D. J. Saunders, G. W. Ingle, *J. Phys. Chem.* **1938**, *42*, 265.
- [2] M. D. Dickey, R. C. Chiechi, R. J. Larsen, E. A. Weiss, D. A. Weitz, G. M. Whitesides, *Adv. Funct. Mater.* **2008**, *18*, 1097.
- [3] R. F. Service, *Science* **2003**, *301*, 909.
- [4] P. Gibbs, H. H. Asada, *J. NeuroEng. Rehabil.* **2005**, *2*, 7.
- [5] D.-H. Kim, J. A. Rogers, *Adv. Mater.* **2008**, *20*, 4887.
- [6] X. Jin, C. Xiao, S. An, G. Jia, *J. Mater. Sci.* **2007**, *42*, 4384.
- [7] N. J. Pinto, P. Carrion, J. X. Quinones, *Mater. Sci. Eng. A* **2004**, *366*, 1.
- [8] D. Zabetakis, M. Dinderman, P. Schoen, *Adv. Mater.* **2005**, *17*, 734.
- [9] G. Che, B. B. Lakshmi, C. R. Martin, E. R. Fisher, R. S. Ruoff, *Chem. Mater.* **1998**, *10*, 260.
- [10] Z. Li, G. Luo, F. Wei, Y. Huang, *Compos. Sci. Technol.* **2006**, *66*, 1022.
- [11] A. Soroudi, M. Skrifvars, *Synthetic Met.* **2010**, *160*, 1143.
- [12] W. Thongruang, R. J. Spontak, C. M. Balik, *Polymer* **2002**, *43*, 3717.
- [13] G. Mattana, P. Cosseddu, B. Fraboni, G. G. Malliaras, J. P. Hinstroza, A. Bonfiglio, *Org. Electron.* **2011**, *12*, 2033.
- [14] B. Kim, V. Koncar, E. Devaux, C. Dufour, P. Viallier, *Synthetic Met.* **2004**, *146*, 167.
- [15] C. R. Ríos-Soberanis, R. A. Ley-Bonilla, R. H. Cruz-Estrada, C. V. Cupul-Manzano, L. M. Rangel-Rodríguez, A. Caballero-Can, *Polym. Int.* **2009**, *58*, 817.
- [16] A. J. Granero, P. Wagner, K. Wagner, J. M. Razal, G. G. Wallace, M. in het Panhuis, *Adv. Funct. Mater.* **2011**, *21*, 955.
- [17] P. Sukitpaneent, T. Thanpitcha, A. Sirivat, C. Weder, R. Rujiravanit, *J. Appl. Polym. Sci.* **2007**, *106*, 4038.
- [18] J. Stejskal, I. Sapurina, J. Proke, J. Zemek, *Synthetic Met.* **1999**, *105*, 195.
- [19] S. P. Lacour, D. Chan, S. Wagner, T. Li, Z. Suo, *Appl. Phys. Lett.* **2006**, *88*, 204103/1.

- [20] T. Li, Z. Huang, Z. Suo, S. P. Lacour, S. Wagner, *Appl. Phys. Lett.* **2004**, 85, 3435.
- [21] D. Zrnic, D. S. Swatik, *J. Less-Common Met.* **1969**, 18, 67.
- [22] J.-H. So, M. D. Dickey, *Lab Chip* **2011**, 11, 905.
- [23] M. R. Khan, G. J. Hayes, J.-H. So, G. Lazzi, M. D. Dickey, *Appl. Phys. Lett.* **2011**, 99, 013501.
- [24] M. Kubo, X. Li, C. Kim, M. Hashimoto, B. J. Wiley, D. Ham, G. M. Whitesides, *Adv. Mater.* **2010**, 22, 2749.
- [25] J.-H. So, J. Thelen, A. Qusba, G. J. Hayes, G. Lazzi, M. D. Dickey, *Adv. Funct. Mater.* **2009**, 19, 3632.
- [26] J.-H. So, H.-J. Koo, M. D. Dickey, O. D. Velev, *Adv. Funct. Mater.* **2011**, 22, 625.
- [27] D. J. Lipomi, B. C. K. Tee, M. Vosgueritchian, Z. Bao, *Adv. Mater.* **2011**, 23, 1771.
- [28] KRATON®, G1643 M Polymer, **2012**, Mar 1,  
[http://docs.kraton.com/tl\\_warehouse/pdf\\_data\\_docs/WG\\_4140\\_WG29E4.tmp.pdf](http://docs.kraton.com/tl_warehouse/pdf_data_docs/WG_4140_WG29E4.tmp.pdf)
- [29] D. Wakuda, K. Suganuma, *Appl. Phys. Lett.* **2011**, 98, 073304.
- [30] J. H. Laurer, R. Bukovnik, R. J. Spontak, *Macromolecules* **1996**, 29, 5760.

## **Chapter 4. Towards All-Soft Matter Circuits: Prototypes of Quasi-Liquid Devices with Memristor Characteristics\***

---

\* This chapter is partially based on H.-J. Koo, J.-H. So, M. D. Dickey, O. D. Velev, *Adv. Mater.*, 2011, 23, 3559.

## 4.1 Introduction

We present a new class of electrically functional devices composed entirely of soft, liquid-based materials that display memristor-like characteristics. A memristor, or a “memory resistor”, is an electronic device that changes its resistive state depending on the current or voltage history through the device. Memristors may become the core of next generation memory devices because of their low energy consumption and high data density and performance.<sup>[1-3]</sup> Since the concept of memristors was theorized in 1971,<sup>[4]</sup> resistive switching memories have been fabricated from a variety of materials operating on magnetic,<sup>[5]</sup> thermal,<sup>[6]</sup> photonic,<sup>[7]</sup> electronic and ionic mechanisms.<sup>[3,8,9]</sup> Conventional memristive devices typically include metal-insulator-metal (M-I-M) junctions composed of rigid stacks of films fabricated by multiple vacuum-deposition steps, often at high temperature. The most common “insulator” materials in M-I-M memristor junctions are inorganic metal oxides such as  $\text{TiO}_2$ <sup>[10]</sup> and  $\text{NiO}$ <sup>[11]</sup>. Conducting pathways can form by current bias across such layers. Solid electrolytes between metal electrodes can also be used to create resistance switches (e.g.,  $\text{Ag}/\text{Ag}_2\text{S}/\text{Pt}$ ), in which conductive metal filaments that bridge the two electrodes can be formed or annihilated on demand.<sup>[3,9]</sup> Memristive circuits composed of organic materials have advantages over conventional metal oxides due to their ease of processing, light weight, and low cost. A variety of organic materials such as homogeneous polymers, small-molecule or nanoparticle doped polymers, and organic donor-acceptor complexes have been evaluated as components in memory switching devices.<sup>[12]</sup>

We present a new class of controllably bi-stable memristor-like devices that are fabricated entirely from liquid-based materials. These soft and flexible devices are built from

liquid metal and hydrogels that are used routinely in laboratories for hosting biological molecules and supporting cell growth. Hydrogels are soft, moldable and bio-compatible media similar to biological systems with high ion mobility due to the high water content (> 90 % water).<sup>[13,14]</sup> The ionic properties of the gels can be tuned by inclusion of polyelectrolytes that are immobilized via entanglement within the gel network. Hydrogels doped with polyelectrolytes have been utilized for fabricating electronic devices such as diodes and photovoltaic cells.<sup>[13,15,16]</sup> The electrodes of these devices, however, are rigid metals such as platinum and they cannot truly be classified as “soft” electronics. Replacing the rigid electrodes with a moldable liquid metal that is electrochemically active harnesses the synergetic effect of the two liquid based materials – hydrogel and a liquid metal. Because these soft memristor prototypes function on the basis of ionic transport, they complement recent reports on the analogy between memristors and neural systems,<sup>[17,18]</sup> where the memristive characteristic of synapses enables learning and adaptation in biological systems.

An eutectic alloy of gallium and indium (EGaIn, 75 % Ga, 25 % In) is well suited as a soft electrode because it is a low viscosity liquid at room temperature with a high conductivity ( $\sigma = 3.4 \times 10^4$  S/cm).<sup>[19]</sup> The surface of the EGaIn liquid metal forms spontaneously a thin, native skin of gallium oxide, which is a wide band-gap semiconductor ( $\sim 4.8$  eV at room temperature).<sup>[20]</sup> The electrical conductance through the oxide skin depends on the thickness of the oxide layer, which can be controlled using pH and/or electric bias to oxidize or reduce the skin.<sup>[21]</sup>

## 4.2 Experimental

The polyelectrolyte doped hydrogels were prepared following a procedure described previously.<sup>[16]</sup> The gel contained 2 wt. % agarose (biochemistry research grade, Acros Organics). PAA ( $M_w$  100,000, Sigma-Aldrich) and PEI ( $M_w$  750,000, Sigma-Aldrich) polyelectrolytes were used as doping agents to adjust pH condition of the hydrogel. The pH values of the hydrogel with 0.72 wt. % and 7.2 wt. % of PAA and 0.57 wt. % and 5.7 wt. % of PEI were  $\sim 2.3$ ,  $\sim 3.3$ ,  $\sim 10.1$  and  $\sim 10.8$ , respectively. Eutectic gallium/indium was purchased from Sigma-Aldrich. For the fabrication of the device shown in **Figure 4.1**, two pieces of Tygon tube filled with EGaIn liquid metal using a syringe were inserted from the bottom of two polydimethylsiloxane (PDMS) molds, which have hemispherical wells of diameter  $\sim 5$  mm. The wells were filled with the polyelectrolyte gels melted by microwave heating to form either PAA/EGaIn or PEI/EGaIn interface. After cooling down, the two polyelectrolyte gels interfacing the EGaIn liquid metal electrodes were brought in contact with each other, creating a gel-gel interface. All I-V curves were collected by using a computer-controlled source meter (Keithley 2602, Keithley Instruments Inc.) at room temperature.

The crossbar array was fabricated by PDMS (Figure 4.1). Two PDMS sheets with four circular holes of diameter  $\sim 2$  mm for each node in the  $2 \times 2$  crossbar array were prepared to support hydrogel pellets doped with PAA or PEI. Another two PDMS sheets with two parallel channels were prepared by soft lithography (i.e., replica molding). The line patterns were placed on the top and the bottom of the two gel layers and crossed perpendicularly from the top view at the junctions of two polyelectrolyte gels, which act as

independent nodes. All of the PDMS sheets were sealed by oxygen plasma treatment. After assembling all of the sheets, the liquid metal was injected into the line channels by using a syringe and tubes to form electrodes.

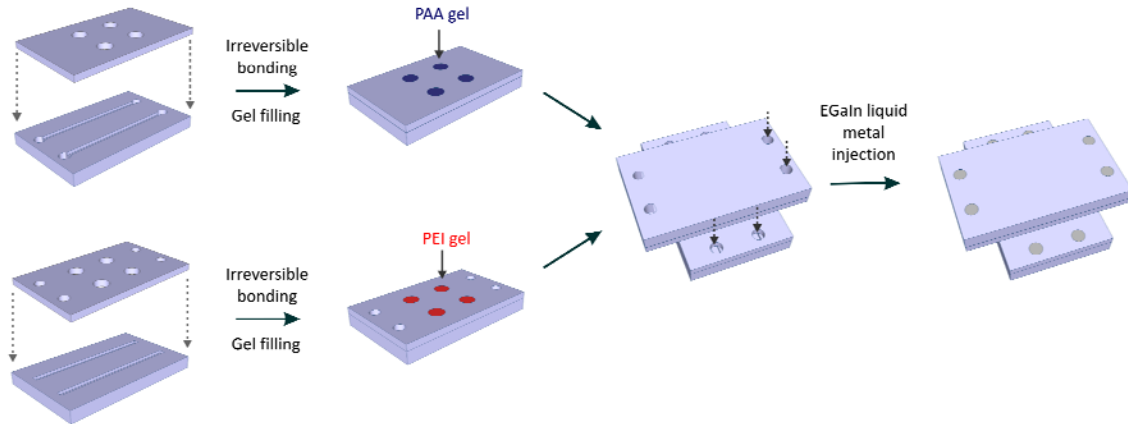


**Figure 4.1** Fabrication process of the memristive circuit with a crossbar structure. Two PDMS sheets with four circular holes of diameter  $\sim 2$  mm were prepared to support hydrogel pellets doped with PAA (blue) or PEI (red). Another set of two PDMS sheets with line patterns were prepared by soft lithography (i.e., replica molding). Each PDMS sheet with holes was assembled with the PDMS sheet with line patterns and sealed by using oxygen plasma. After inserting the gel pellets into the holes, the two sets of PDMS sheets were aligned perpendicularly to create four nodes with gel-gel interface. The liquid metal was injected into the line channels by using a syringe and tubes to form electrodes at the top and bottom of the stacked gel layers.

### 4.3 Fabrication and Characterization of Soft Matter Based Memristors

We constructed memristor-like devices composed of two liquid metal electrodes separated by two thin layers of hydrogel each doped with polyelectrolytes (polyacrylic acid, PAA and polyethylene imine, PEI) as shown in **Figure 4.2a**. The polyelectrolytes control the local pH in the gel and create asymmetry in the device, which is essential for bipolar switching memristors.<sup>[22]</sup> The local pH in the individual gel layers is maintained because the

polyelectrolyte molecules, acting as buffers, are entangled with the agarose polymer network.<sup>[15]</sup> The fabricated device exhibits hysteretic and bipolar I-V traces that are characteristic of memristive devices (Figure 4.2b). In the range of positive voltage, the device shows two different levels of current values depending on the history of the bias. The current during the forward sweep from 0 V to 5 V (1 and 3<sub>b</sub> in Figure 4.2b) is approximately two orders of magnitude higher than those during the backward sweep from 5 V to 0 V (2<sub>a</sub> and 4 in Figure 4.2b).

The thickness of the oxide skin that forms on the metal dictates the conductance through the device; the ability to control the thickness of the oxide in an asymmetric fashion is central to the operation of the quasi-liquid memristors. To elucidate their operating mechanism, we investigated the effect of pH and electric bias on the interface between the liquid metal and the (PAA or PEI) gel. According to the Pourbaix diagram,<sup>[21]</sup> the oxidation and reduction of liquid metal depends on the applied electric bias and pH values of its local environment. We observed the morphology of the surface of the liquid metal electrodes in each polyelectrolyte solution while applying a bias of  $\pm 5$  V between two liquid metal electrodes using the experimental set-up illustrated in **Figure 4.3a**. Figure 4.3b and 4.3c show the effect of PAA and PEI polyelectrolytes on the formation of the oxide skin of the metal electrodes (at 10 $\times$  the concentration in the bulk in order to highlight their effect). Before applying a bias, the electrode, which is coated with a thin native oxide layer, appears smooth, reflective, and metallic. After applying + 5 V to the electrode in the PAA solution, the whole surface formed a thick oxide skin as shown in Figure 4.3b. This skin maintained

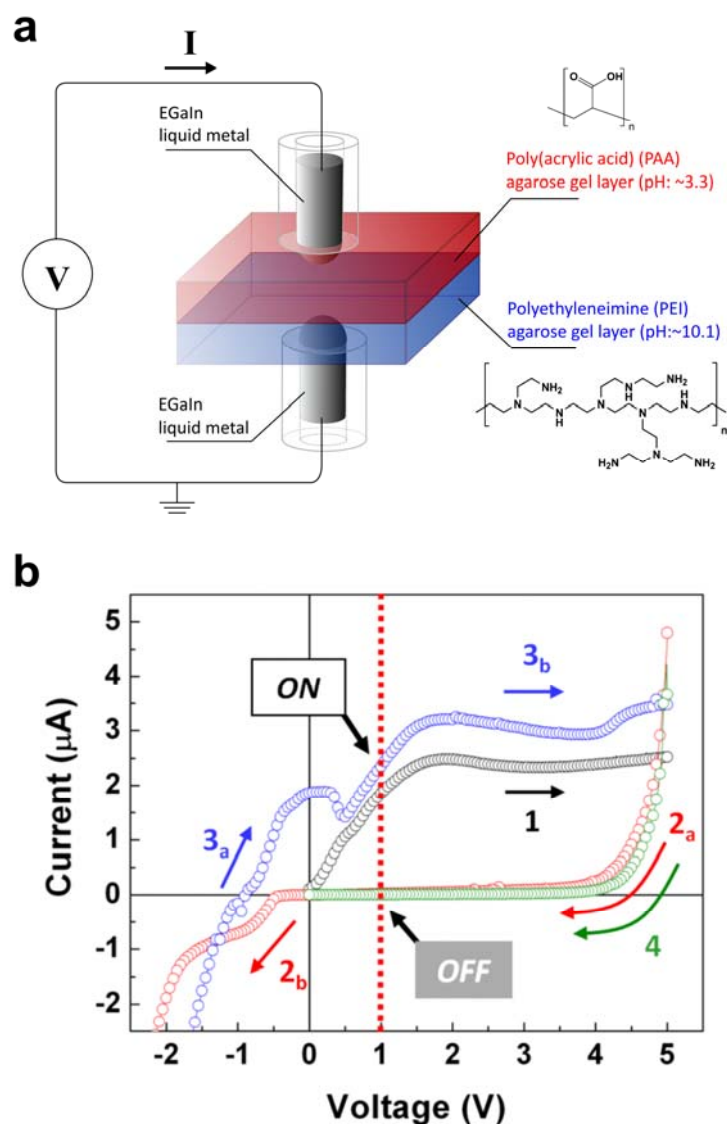


**Figure 4.2** Soft memristor prototypes based entirely on soft materials. (a) A schematic depiction of the memristive device. Two polyelectrolytes entrapped in a matrix of agarose/ $H_2O$  dictate the pH values of each hydrogel layer. (b) I-V curves of the device by  $\pm 5$  V sweeps. The numbers and the arrows represent the order and the direction of the bias sweeps, respectively. The hysteresis of the I-V curves is the characteristic feature of memristors. The red dotted line indicates the reading bias of 1 V, where the “memorized” resistance is measured. The sweep rate is 0.04 V/s.

its shape and morphology for more than 1 hour (without bias) until we applied  $-5\text{ V}$  to reduce it. The surface of the electrode in the PEI solution under  $+5\text{ V}$ , however, only changed slightly compared to that in the PAA solution (Figure 4.3c) and reverted spontaneously to its original state within a couple of minutes. The difference in the oxidative behavior of the skin of the metal is associated with the pH values of the PAA and PEI polyelectrolytes in the agarose gel, which are  $\approx 3.3$  and  $\approx 10.1$ , respectively. Experiments with polyelectrolyte concentrations equivalent to those used in the soft memristor, and experiments with aqueous HCl and NaOH solutions with pH values equivalent to those of gels in the device show the same results as those in Figure 4.3b and 3c (**Figure 4.4**), supporting the conclusion that pH is the critical parameter for controlling the formation and removal of the oxide skin. The anodic formation of the oxide film on EGaIn is analogous to the properties of typical valve metals, such as Al, Ta and Nb.<sup>[23, 24]</sup>

In our system, the asymmetry leading to memristor-like behavior arises from differences in the stability of the surface oxide layers on the two metal electrodes that contact the polyelectrolyte gel (Figure 4.3d). A positive bias applied to the electrode interfacing the PAA gel causes the metal to oxidize further and thereby decreases the conductance through the device. A negative bias applied to the same electrode reduces the oxide layer at the interface between EGaIn/PAA gel. At the other electrode, the interface of the EGaIn/PEI gel invariably suppresses the oxidation reaction driven by the applied bias and consequently introduces asymmetry into the device. Thus, the formation (i.e., oxidation) or removal (i.e., reduction) of the oxide layer at the interface of the PAA-doped gel determines the high (“off”) or low (“on”) resistance states of the memristor, respectively.

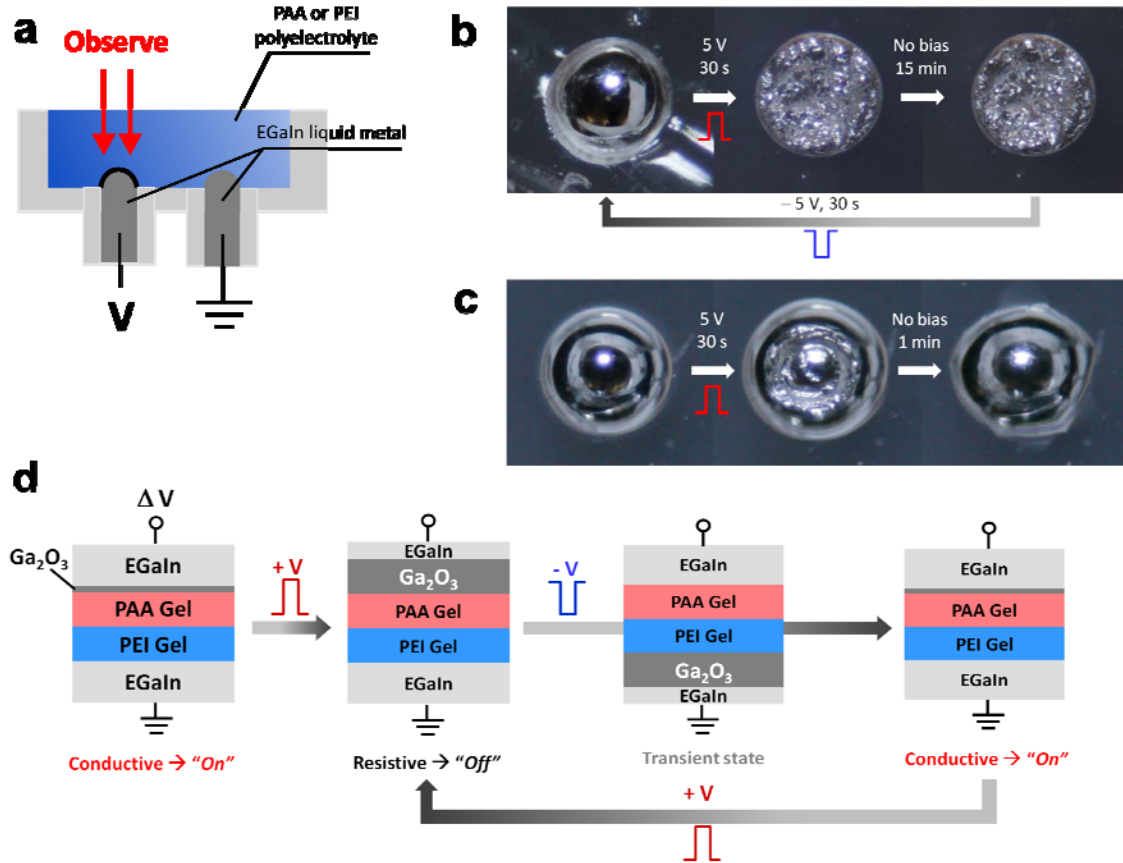


**Figure 4.3** Proposed operating mechanism of the gel/liquid metal memristors based on the electrochemical behavior of the oxide skin of the metal in PAA or PEI polyelectrolyte solution. (a) Cross-sectional view of the experimental set-up for the observation of the surface of the EGaIn electrodes in each polyelectrolyte solution. Flexible plastic tubes of diameter  $\sim 500 \mu\text{m}$  filled with EGaIn were inserted from the bottom of the solution reservoir. The concentrations of PAA and PEI are 7.5 wt. % and 5.7 wt. %, respectively. (b, c) Optical images of the top surface of the EGaIn electrodes to which voltage is applied in PAA (b) or PEI (c) solution. In the presence of aqueous PAA, a thick oxide layer on the EGaIn electrode is formed or removed depending on the applied bias. In the presence of aqueous PEI, the oxide layer formed by the applied bias is unstable and is spontaneously removed. (d) Proposed mechanism of memristor-like function based on the electrochemical behavior of the oxide skin of the EGaIn electrodes. Since the interface of PEI/EGaIn stays conductive, the formation and dissolution of an oxide layer at the PAA/EGaIn interface determines the resistance of the memristor.

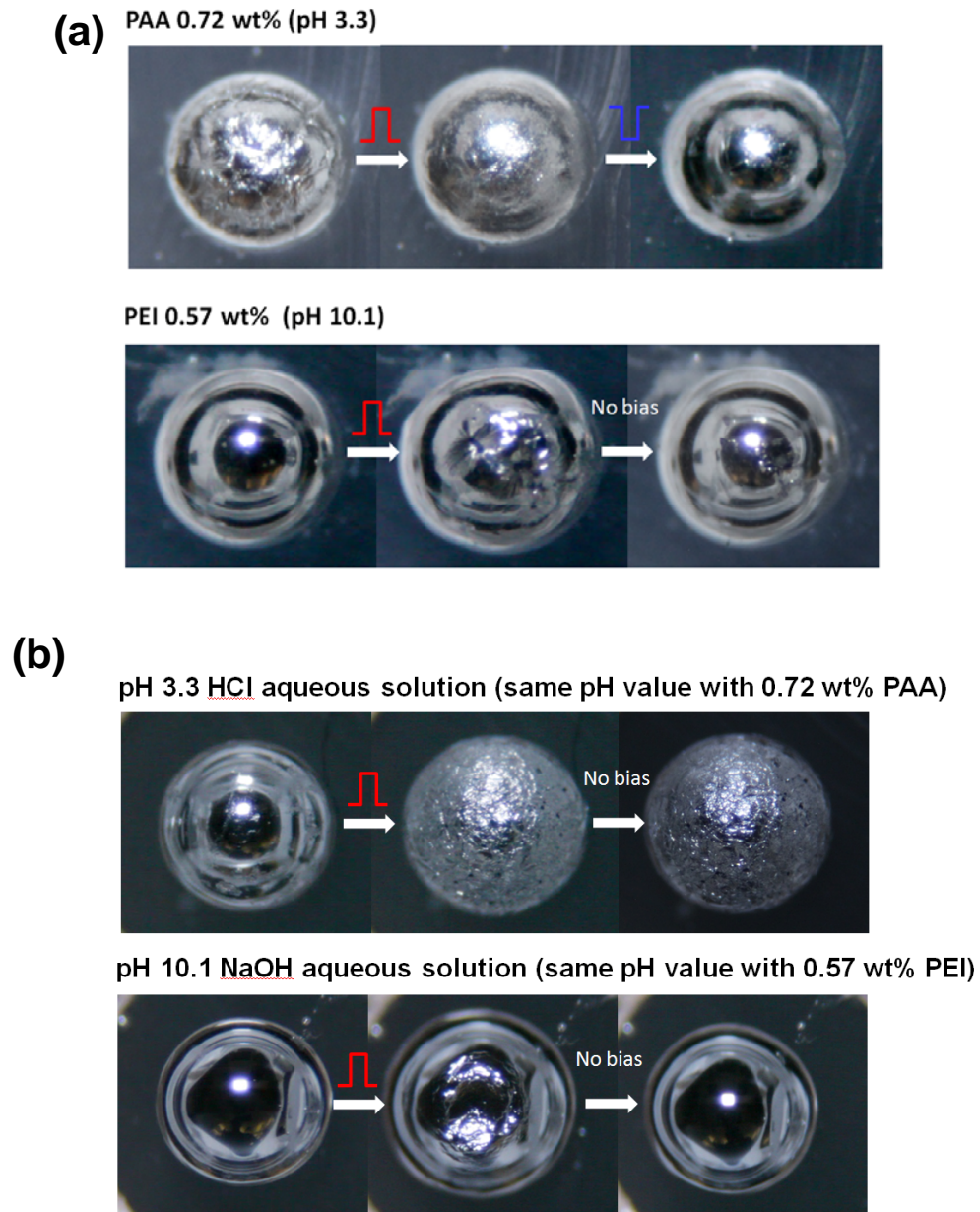


**Figure 4.4** The effect of pH conditions on the formation of oxide skin on the EGaIn electrodes. (a) Optical images of the surface of the EGaIn electrodes to which the voltage is applied in PAA or PEI polyelectrolyte solution of the same concentration as the memristor device. (b) The EGaIn electrodes in aqueous solution with identical pH values as the memristor device show the same surface morphological changes in terms of the bias application, which suggests that the different pH values of PAA and PEI polyelectrolyte solutions result in the difference in the oxide formation.

The oxide-based mechanism is consistent with the bipolar I-V characteristic of the memristor shown in Figure 4.2b. The oxide layer grows at the interface of EGaIn/PAA gel during the first forward positive sweep (1 in Figure 4.2b) from 0 V to 5 V, which sets the memristor into the high resistance state (off state) and maintains its increased resistance during the backward sweep from 5 V to 0 V (2<sub>a</sub>). The grown oxide layer is reduced during the negative bias sweeps (2<sub>b</sub> and 3<sub>a</sub>) and the memristor resets into the low resistance (“on”) state. The I-V curves of the consecutive forward and backward positive sweeps (3<sub>b</sub> and 4) demonstrate a recovery of the first positive sweeps (1 and 2<sub>a</sub>). The current and voltage traces of these soft memristive devices show subtle differences from conventional semiconductor memristors,<sup>[2,8,10]</sup> which operate on completely different principles and materials. However, they clearly show the essential memristive characteristics – bistable, history-based resistance,

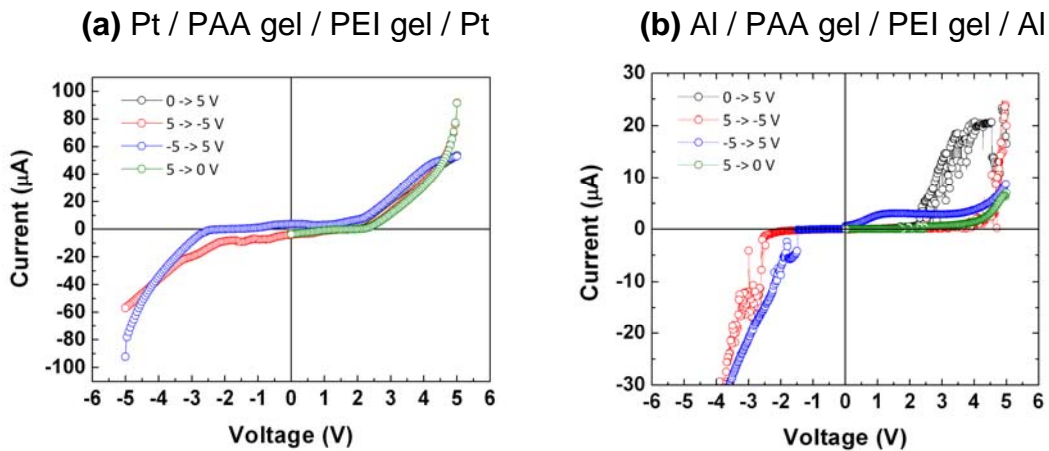


**Figure 4.5** (a) Symmetric I-V traces with no hysteresis occur when electrochemically inert metals, such as platinum, were used as electrodes. (b) The device with Al electrodes shows slight I-V hysteresis because Al also forms an oxide layer on its surface. Compared to solid Al metal, it appears that the liquid EGaIn metal has the advantage of self-regeneration due to its fluidity, which results in reproducible hysteresis and more reliable memristive performance.

which can be reversibly switched between on and off states. The non-zero current at 0 V during sweep 3 likely results from the spontaneous formation of the native oxide at the interface of the PAA gel/EGaIn.<sup>[25,26]</sup> This current is transient and is suppressed when the oxide skin grows to the equilibrium thickness. Inert metal electrodes (e.g., Pt) or symmetrical gel layers do not exhibit the effective memristive as shown in **Figure 4.5, 4.6** and **4.7**. Further electrochemical studies are underway to better understand any secondary processes that may be occurring in this ionic system.

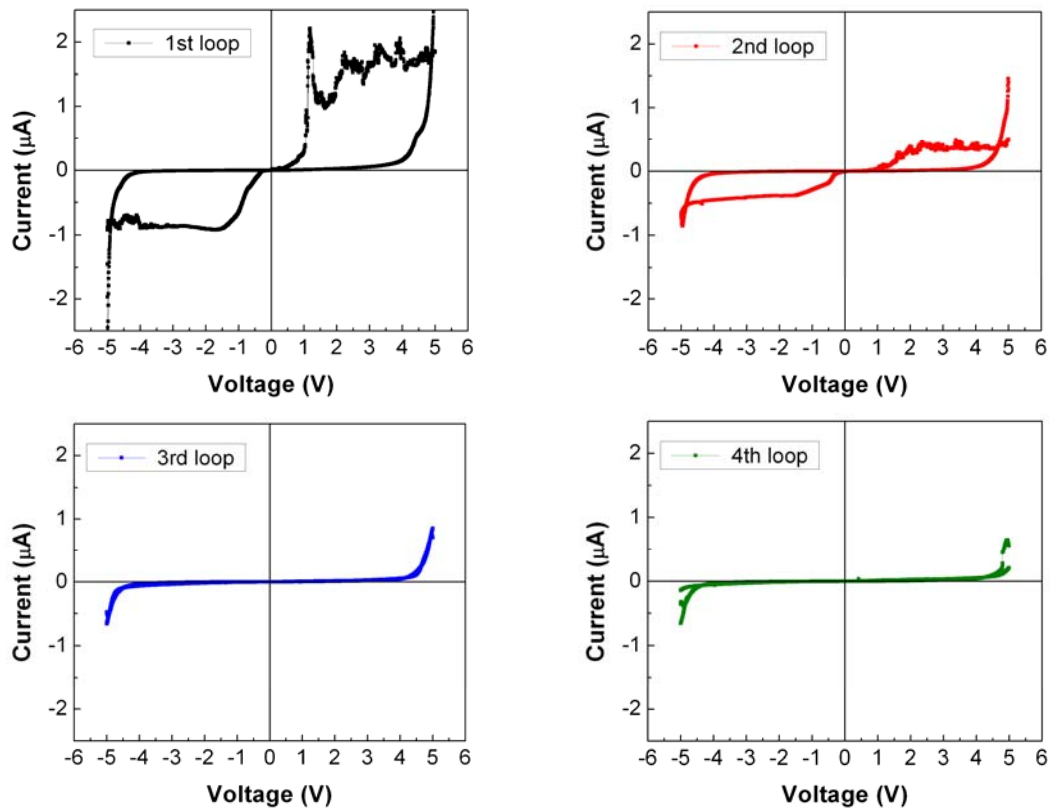


**Figure 4.6** The device with symmetric PAA polyelectrolyte gel exhibited hysteretic I-V curves initially. However, since the oxide skin grows at both electrodes under the pH environment of PAA, total resistance of the device continuously increases as the bias loop is repeated.

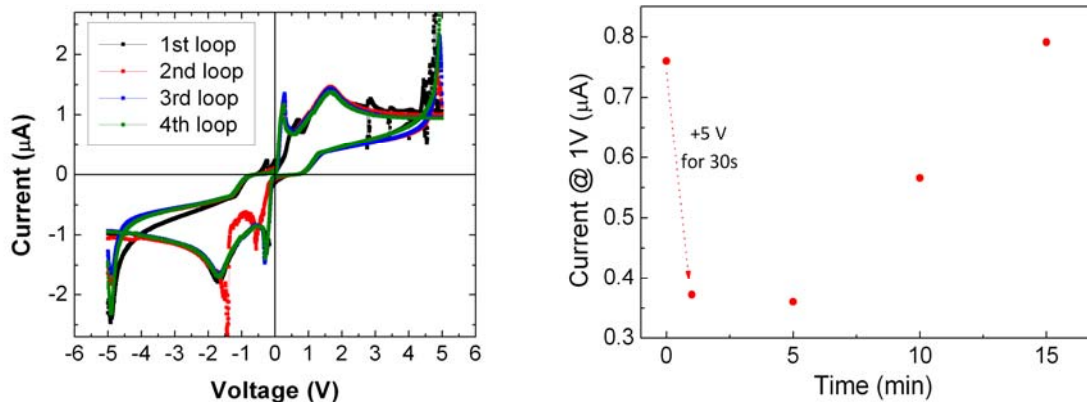


**Figure 4.7** Slight hysteresis occurs in the device with only PEI polyelectrolyte gel, which is maintained even in the consecutive bias cycles (left). However, the off-state resets spontaneously to the on-state after  $\sim 10$  min because the oxide skin is unstable and removed under the PEI environment (right).

A quantitative analysis on the effect of the bias history on the resistance of the device establishes the operational parameters of the soft matter memristor, including the switching and reading biases. Consecutive forward and backward bias sweeps of varying magnitudes up to 10 V applied to a pristine device resulted in the I-V traces shown in **Figure 4.8a**. First, sweeping the voltage forward and backward from 0 V to 1 V (black curves in first row) produced I-V traces with hysteresis in which the current is suppressed during the backward sweep. This result suggests that the thickness of the oxide layer increases during the forward sweep. The device remembers its processing history and "records" bias magnitude in the form of a highly resistive state that is maintained even after the bias is removed. The current remains suppressed initially in the subsequent sweep from 0 to 3 V (red curves in second row) and only increases after exceeding  $\sim 1$  V. Similarly, the I-V traces in the consecutive sweeps from 0 to 5 V and from 0 to 10 V (blue and green curves in third and fifth rows) exhibit rapid increase of the current at  $\sim 3$  V and  $\sim 5$  V, which are the

recorded maximum voltages during the previous sweeps (0 to 3 V and from 0 to 5 V, respectively). Thus, the maximum voltage of the pre-applied bias determines the range of bias in which the memristor maintains a high resistive state. The “stored” resistance can be read as long as the reading bias is lower than the switching bias. We selected  $\pm 5$  V as the switching bias to turn on and off the memristor and 1 V as the reading bias, which are similar in magnitude to solid state memristors.

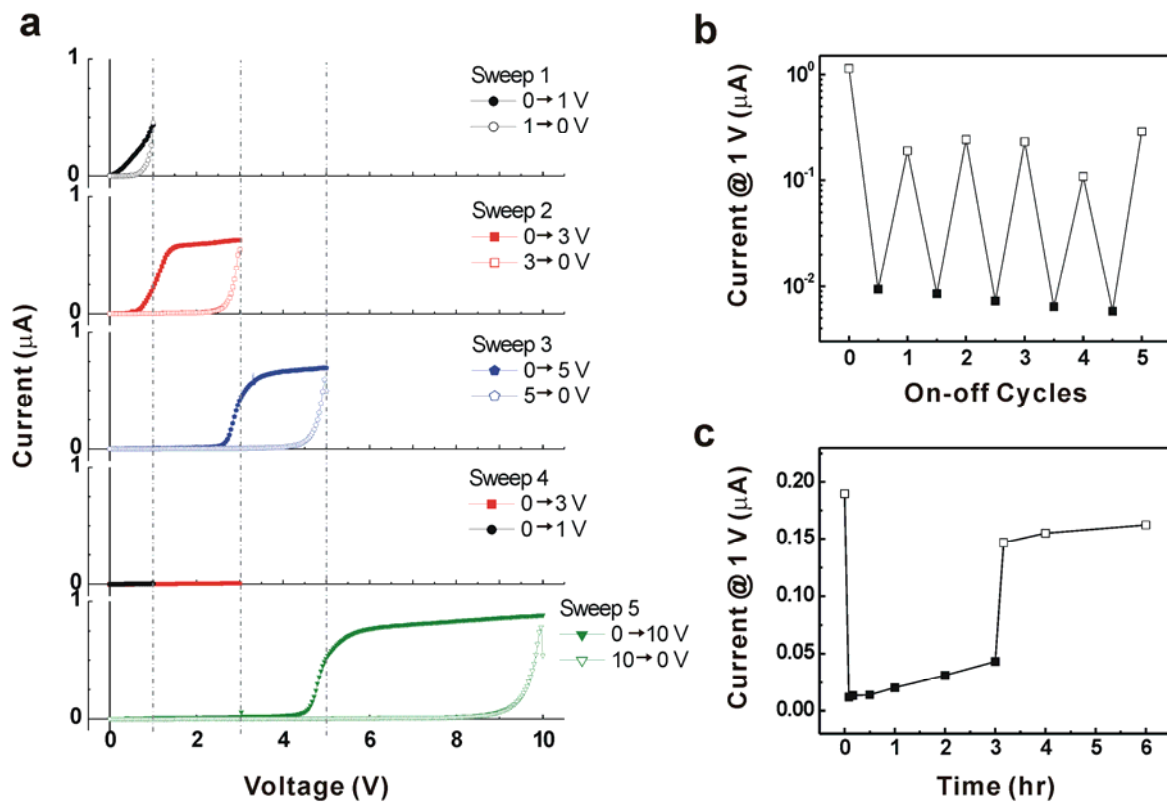


**Figure 4.8** Performance characteristics of the gel/liquid metal memristors. (a) Conductance through the device depends on the pre-applied bias history. The current is suppressed (off state) below the maximum pre-applied voltage. (b) Switching performance of the memristors. (c) Long-term stability of the stored information. The low-conductance, i. e. ‘off’ state, is restored to ‘on’ state after 3 hrs by applying the switching bias. A switching bias of  $\pm 5$  V was applied to the memristors for 3 sec for the experiments of b and c.

We assessed the reliability of the quasi-liquid memristor by performing on-off switching tests and evaluated the stability by observing how the recorded resistance changes with time. Figure 4.8b shows that these prototypes can be switched reversibly between high and low resistance states during multiple cycles. Figure 4.8c demonstrates the long-term stability of the recorded resistance, where for both on and off states, the device preserved the recorded resistance for more than 3 hours. Since the polyelectrolytes are molecularly entangled with the gel matrix and therefore immobilized,<sup>[15]</sup> each polyelectrolyte gel maintains the effective pH medium at the electrode interface contrary to hydrogels doped with small diffusive ions such as HCl and NaOH. There is no significant difference in current at the on and off states in terms of the duration of the applied switching bias over a range of 3 to 30 sec (**Figure 4.9**). Overall, the quasi-liquid prototype exhibits reliable switching behavior and reasonable long term stability considering the simplicity of the architecture.

We demonstrated that these memristor elements can be integrated into soft memory matrices by constructing a basic crossbar array in which the resistance at each node can be controlled independently. **Figure 4.10a** shows a prototype circuit fabricated by aligning perpendicularly two sets of liquid metal lines at the top and bottom of a stack of doped hydrogel layers. Figure 4.10b is a schematic of the circuit with the four memristive nodes. The circuit possesses  $2^4$  different binary information states for the on and off states at each node. We confirmed that each node can be operated independently without crosstalk in the integrated memristive circuit (Figure 4.10c). Switching node 1-B from on to off (or vice

versa) showed a decreased or recovered current (green filled or empty triangles) while the other nodes maintained their conductance. In the subsequent measurement, the node 2-A also showed similar switching behavior as the node 1-B, confirming independently controlled information state at each node.

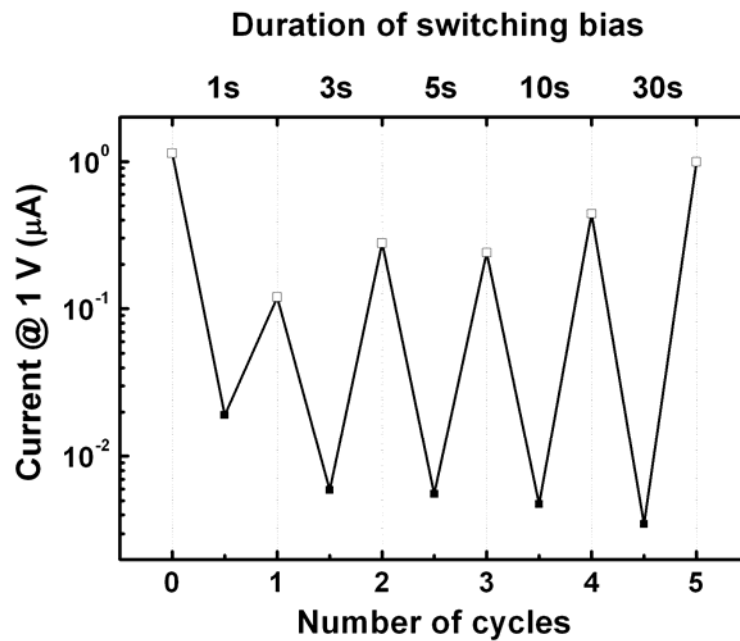


**Figure 4.9** Effect of the duration of switching bias on the on/off ratio of the memristor. The “on” state becomes slightly more conductive at longer switching times and the “off” state becomes slightly less conductive at longer switching times. Regardless, switching occurs after only 1 s of applying the switching bias.

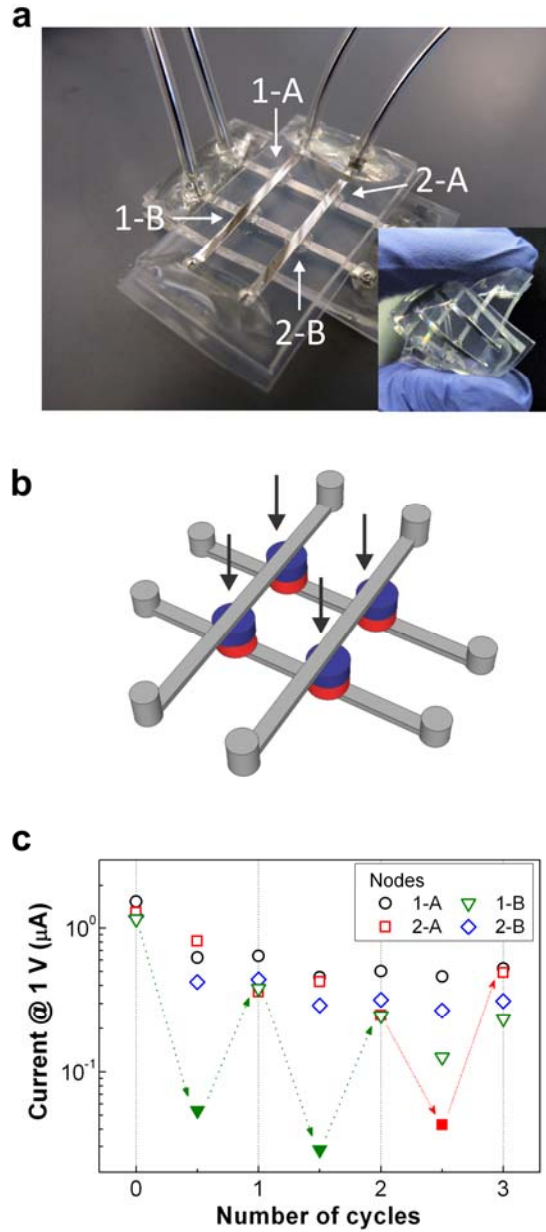


**Figure 4.10** A crossbar array of soft material-based memristors. (a) Photograph of a prototype of an integrated memristor circuit with a  $2 \times 2$  crossbar array. The device is flexible as shown in the inset image and compatible with water. (b) Schematic of the prototype in (a). The arrows point to the nodes. (c) Switching performance of the memristor circuit device. The switching bias to turn ‘off’ (+ 5 V) and ‘on’ (– 5 V) the nodes is applied to the 1-B node for the first and second cycles and to the 2-A node for the third cycle, respectively, as shown by the arrows. The filled symbols represent the nodes in the ‘off’ state. The switching bias was applied to each node for 1 sec to minimize the crosstalk.

#### 4.4 Conclusion

In conclusion, we present a new class of memristors that is based entirely on soft materials and operates on an ionic conductance mechanism. The devices are simple to fabricate using bench top methods and consist of hydrogels doped with polyelectrolytes sandwiched with liquid metal electrodes. The asymmetric configuration of the gels allows effective resistive switching by controlling the formation of the interfacial oxide layers by electric bias, while memorizing the last state of the system. The devices showed reliable switching behavior and stable long-term operation. A crossbar integrated memristive circuit demonstrates the scalability of this liquid based architecture. Since the operation of the memristor is based on ionic conductance in aqueous systems, such classes of devices could find potential applications in bioelectronic systems, such as artificial brain-mimicking or neuromorphic structures, and provide better understanding of the origin of primitive intelligence. The polysaccharide hydrogel core of these devices is biocompatible and they could be interfaced with live neural tissue and other biological systems. Further research on the optimization and improvement of the prototype memristors could enable fabrication of high density three-dimensional soft circuits and *in vivo* operation of such devices.

## 4.5 References

- [1] J. Borghetti, G. S. Snider, P. J. Kuekes, J. J. Yang, D. R. Stewart, R. S. Williams, *Nature* **2010**, 464, 873.
- [2] E. Linn, R. Rosezin, C. Kügeler, R. Waser, *Nature Mater.* **2010**, 9, 403.
- [3] K. Terabe, T. Hasegawa, T. Nakayama, M. Aono, *Nature* **2005**, 433, 47.
- [4] L. O. Chua, *IEEE Trans. on Circuit Theory* **1971**, CT18, 507.
- [5] A. Asamitsu, Y. Tomioka, H. Kuwahara, Y. Tokura, *Nature* **1997**, 388, 50.
- [6] F. A. Chudnovskii, L. L. Odynets, A. L. Pergament, G. B. Stefanovich, *J. Solid State Chem.* **1996**, 122, 95.
- [7] C. Yu, H. Wang, *Adv. Mater.* **2010**, 22, 966.
- [8] D. B. Strukov, G. S. Snider, D. R. Stewart, R. S. Williams, *Nature* **2008**, 453, 80.
- [9] R. Waser, R. Dittmann, G. Staikov, K. Szot, *Adv. Mater.* **2009**, 21, 2632.
- [10] J. J. Yang, M. D. Pickett, X. Li, D. A. A. Ohlberg, D. R. Stewart, R. S. Williams, *Nature Nanotechnol.* **2008**, 3, 429.
- [11] D. C. Kim, S. Seo, S. E. Ahn, D.-S. Suh, M. J. Lee, B.-H. Park, and I. K. Yoo, I. G. Baek, H.-J. Kim, E. K. Yim, J. E. Lee, S. O. Park, H. S. Kim, U-In Chung, J. T. Moon, B. I. Ryu, *Appl. Phys. Lett.* **2006**, 88, 202102.
- [12] J. Scott, L. Bozano, *Adv. Mater.* **2007**, 19, 1452.
- [13] H.-J. Koo, S. T. Chang, J. M. Slocik, R. R. Naik, O. D. Velev, *J. Mater. Chem.* **2011**, 21, 72.
- [14] C. J. Ferris, M. in het Panhuis, *Soft Matter* **2009**, 5, 3430.
- [15] O. J. Cayre, S. T. Chang, O. D. Velev, *J. Am. Chem. Soc.* **2007**, 129, 10801.
- [16] H. J. Koo, S. T. Chang, O. D. Velev, *Small* **2010**, 6, 1393.
- [17] S. H. Jo, T. Chang, I. Ebong, B. B. Bhadviya, P. Mazumder, W. Lu, *Nano Lett.* **2010**, 10, 1297.
- [18] Y. V. Pershin, S. La Fontaine, M. Di Ventra *Phys. Rev. E* **2009**, 80, 021926.
- [19] J. N. Koster *Cryst. Res. Technol.* **1999**, 34, 1129.

- [20] H. H. Tippins *Phys. Rev.* **1965**, 140, A316.
- [21] M. Pourbaix, *Atlas of electrochemical equilibria in aqueous solutions – gallium*, NACE, Houston, **1974**, 428.
- [22] R. Waser, M. Aono, *Nature Mater.* **2007**, 6, 833.
- [23] S. Darwish, M. W. Khalil, M. A. Abdel Rahim, I.A. Ammar, *Materialwiss. Werkstofftech.* **1989**, 20, 299.
- [24] A. W. Hassel, D. Diesing, *Thin Solid Films* **2002**, 414, 296.
- [25] J. N. Butler, M. L. Meehan, *J. Phys. Chem.* **1966**, 70, 3582.
- [26] A. Varadharaj, G. Prabhakara Rao, *J. Electroanal. Chem. Interfacial Electrochem.* **1982**, 138, 189.

# **Chapter 5. Inherently Aligned Microfluidic Electrodes Composed of Liquid Metal**

---

This chapter is partially based on J.-H. So, M. D. Dickey, *Lab Chip* 2011, *11*, 905.

## 5.1 Introduction

This chapter presents a simple technique for the fabrication of electrodes composed of a liquid metal that are inherently aligned with and in direct contact with microfluidic channels. Metallic microcomponents are essential for numerous microfluidic devices. They can be used as heaters,<sup>[1-4]</sup> magnets,<sup>[5-7]</sup> antennas,<sup>[8]</sup> electrochemical sensors,<sup>[9-12]</sup> electromechanical pumps and actuators.<sup>[13, 14]</sup> They can also be used as mixers,<sup>[15, 16]</sup> pumps,<sup>[17, 18]</sup> and sorters<sup>[19, 20]</sup> based on the principles of electrophoresis, dielectrophoresis, and electroosmosis. Injecting metals with low melting points, such as solder, into microchannels is a simple way to fabricate electrodes. Here, we show it is possible to fabricate electrodes that are in direct contact with a microfluidic channel (i.e., a channel that can be used for conventional microfluidic applications, such as fluid manipulation and analysis) by injecting liquid metal into specially designed microfluidic channels. All of the channels are patterned in the same lithographic step; the electrodes are therefore significantly simpler to fabricate than conventional approaches that involve multiple fabrication steps and registration (i.e., alignment of the electrodes with the microchannel). Injection of the liquid metal can be done by hand at room temperature and produces electrodes that vertically span the sidewalls of the channel, which is important for generating electric fields with non-diverging field lines throughout the microfluidic channel. This chapter discusses the formation, stability, and performance of these liquid metal electrodes.

Microfluidic channels are fabricated typically by sealing a substrate (e.g., polydimethylsiloxane (PDMS) or glass) featuring recessed channels to a flat substrate. A common way to incorporate metal microcomponents into these devices is to pattern thin

metallic features onto the flat substrate prior to sealing.<sup>[21-23]</sup> This approach involves depositing metal (e.g., thermal evaporation, e-beam evaporation, electro-deposition, sputtering) and patterning the metal (e.g., lithography), which both require specialized equipment. The resulting patterned microelectrodes must be aligned (i.e., registered) with the microchannels, which is challenging and often results in poor sealing because of the topography of the patterned electrodes. Another limitation of this conventional approach is that the thin metal electrodes are in the same plane and are effectively two-dimensional; because the electrodes do not span the top to bottom of the microchannel, all electric field lines between adjacent electrodes will diverge within the channel.<sup>[24]</sup> Diverging field lines may be desirable for certain applications (e.g., dielectrophoresis), but not for those that require uniform field lines.

Several approaches have been developed to provide alternative ways to fabricate metallic microcomponents in microchannels. For example, ion milling of metal coated structures,<sup>[25]</sup> depositing metal films or implanting metal ions at an angle can create electrodes on the side walls of microfluidic channels.<sup>[26, 27]</sup> This approach still requires physical alignment (of the microchannels with the deposition source) and the electrodes can easily crack when deposited onto soft materials such as PDMS. Electrodeposition can also be used to create electrodes that span the top to bottom of a microfluidic channel. For example, gold electrodes electrodeposited on the side walls of a microfluidic channel showed lateral electrical fields uniform along the vertical direction in the channel.<sup>[28]</sup> This approach, however, requires registration and multiples steps such as e-beam evaporation to define seed layers for plating. Polymer-based conducting composites smeared onto a sacrificial mold

have also been used to produce three-dimensional microelectrodes.<sup>[29-31]</sup> The fabrication process, however, is time consuming and requires multiple lithographic steps and alignment. Furthermore, the composite materials tend to have lower conductivity than pure metals.

Cofabrication is a strategy for fabricating multiple microsystems in a single step by injecting functional materials into pre-fabricated channels.<sup>[32]</sup> It generates correctly aligned micro-components in a fast and inexpensive way. For example, wires, microelectrodes,<sup>[33]</sup> micro-heaters<sup>[34]</sup> and electromagnets<sup>[35]</sup> can be formed by injecting solder or conducting liquid into channels. These components are adjacent to, but physically isolated from the fluidic channels (i.e., those used to manipulate fluids such as water) by the walls of the channels (typically PDMS). Here, we demonstrate an approach to co-fabricate microelectrodes by using specially designed channels that harness the unique rheological properties of certain fluid metals to achieve electrodes in direct contact with the fluids in microfluidic channels. The metal is injected into electrode channels (we define the term “electrode channel” to differentiate them from the “fluidic channel” used subsequently to manipulate fluids) formed during the same lithographic steps to make the fluidic channels. The resulting metal electrodes are inherently aligned with other components and the electrodes span the top to bottom of the channel. The ability to fabricate microelectrodes in direct contact with fluidic channels is necessary for various applications including electrophoresis, dielectrophoresis, electroosmosis, and electrochemistry. Bringing the electrodes closer to the fluidic channel also enhances the intensity of the applied electric field resulting in, for example, more effective sorting, mixing and amplified electric signals for sensing.

We focus primarily on eutectic gallium indium (EGaIn, Ga 75 % In 25 % by weight, m.p.  $\sim 15.7$  °C) for the liquid metal electrode because the metal is a low viscosity liquid (approximately twice the viscosity of water) at room temperature, and therefore, can be injected readily by hand into microfluidic channels to form electrodes without heating. We also demonstrate the possibility of injecting molten, low melting-point metals such as gallium (Ga, m.p.  $\sim 30$  °C) and an indium alloy (InBiSn, In 51 % Bi 32.5 % Sn 16.5 % by weight, m.p.  $\sim 60$  °C, Indium corp.), which are solid at room temperature. These low melting point metals have the appeal that they are solids at room temperature and are therefore more stable mechanically than liquids such as EGaIn. EGaIn is stabilized mechanically within the channels by a thin oxide skin. The oxide skin is a wide band-gap semiconductor, however, it is thin<sup>[36]</sup> enough for EGaIn with the skin to be utilized to measure charge transport through self-assembled monolayer (SAM).<sup>[37]</sup> The metal will flow into a channel as long as the applied pressure at the inlet exceeds the critical pressure required to rupture the skin.<sup>[36]</sup> The critical pressure scales inversely with the cross sectional dimensions of the channel (i.e., narrow channels require greater pressure than channels with wide cross sections). Controlling the geometry of the channels therefore provides a simple means of guiding where (and where not) the liquid will flow. Once the metal stops flowing, the skin reforms spontaneously and rapidly on the surface of the metal and restabilizes the metal such that the electrodes maintain their shape.<sup>[36]</sup> We harness this feature to force the metal to be adjacent to the fluidic channel without flowing into the fluidic channel (as shown in **Figure 5.1**). The liquid metal electrodes are stable and can generate electric fields in both non-aqueous and aqueous systems under DC and AC electric fields. Here, we demonstrate

and characterize the stability of these electrodes, and highlight their utility for an application involving electrohydrodynamic mixing, which requires large electric fields.

## **5.2 Fabrication and Characterization of the Liquid Metal Microelectrodes**

We fabricated microelectrodes in direct contact with a central fluidic channel by injecting liquid metal into PDMS microchannels that flank the fluidic channel, as shown in Figure 5.1. We chose this geometry because it enables the application of electric fields perpendicular to the direction of flow over long distances. To fabricate the electrodes, we first used photolithography to generate a “master” pattern of the electrodes and the fluidic channel on a silicon wafer using a negative photoresist (SU-8, Microchem). Curing a PDMS pre-polymer against this topographically patterned substrate (i.e., molding)<sup>[38]</sup> produced an inverse replica of the master. After brief exposure of the replica to oxygen plasma, we sealed it to a substrate (either glass or PDMS), producing simultaneously the fluidic channel and the electrode channels. We injected liquid metal into the electrode channels by hand using a syringe. A row of posts between the electrode channels and the central fluidic channel guided the liquid metal through the electrode channels during the filling process. The distance between two neighboring posts in Figure 5.1(b) is much smaller than the width of the electrode channels (50  $\mu\text{m}$  vs. 1000  $\mu\text{m}$ ), yet have the same height (50  $\mu\text{m}$ ). Thus, the critical pressure required to inject the metal through the electrode channels ( $\sim 13$  kPa) is almost half of that required to inject it between the posts ( $\sim 25$  kPa); the metal flows readily along the path of least resistance. The liquid metal can be injected into the electrode channels to form electrodes that align inherently with the central fluidic channel without

leaking through the posts. The electrodes span from top to bottom of the fluidic channel with a thickness exactly equal to the height of the channel. These electrodes would be challenging to fabricate with conventional deposition processes.

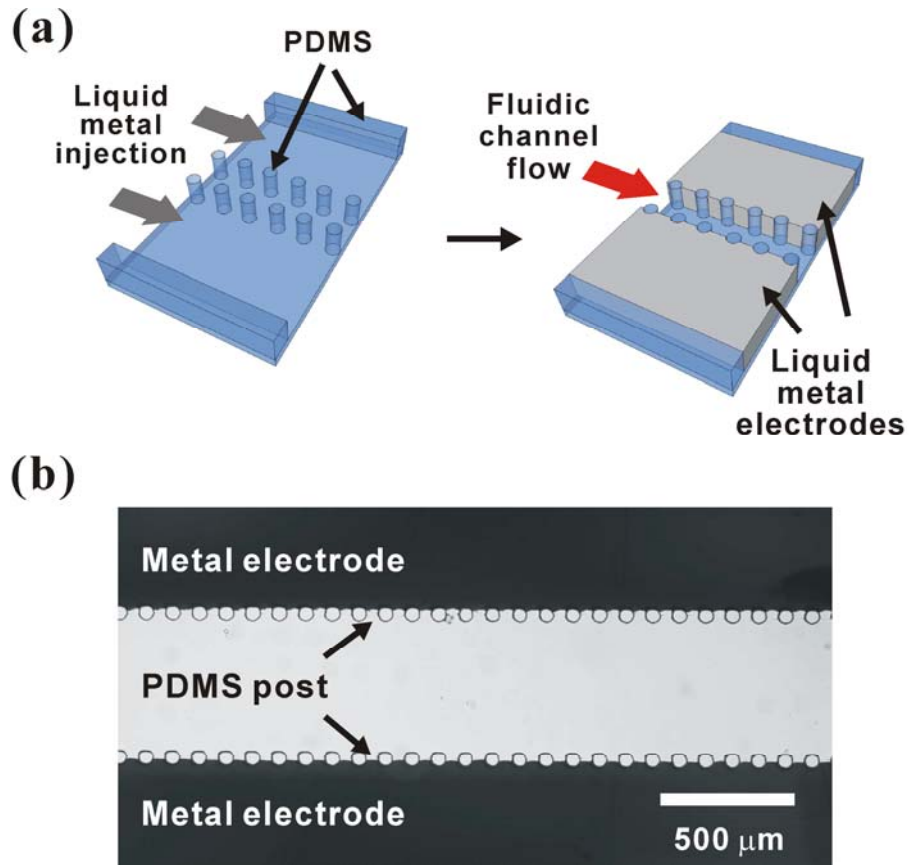


**Figure 5.1** (a) Cut-away depiction of the process used to fabricate liquid metal microelectrodes in contact with a central fluidic channel. Two parallel rows of posts separate the liquid metal electrodes from the fluidic channel. (Not shown: The channels are sealed on top by a flat slab of PDMS.) (b) Top-down, back-lit optical micrograph of the fluidic channel flanked by two liquid metal electrodes. The posts prevent the metal from entering the fluidic channel.

The shape and spacing of the microelectrodes dictates the spatial pattern of the electric field lines in the fluidic channel. We explored several different electrode geometries that may be useful depending on the desired application. Figure 5.1(b) is a representative micrograph of a portion of electrodes that extend the length of a channel (~ 3 cm long, the limit of our equipment). A potential limitation of this geometry is that the electrodes are interspersed with PDMS pillars that may affect the flow profile in the fluidic channel. **Figure 5.2** shows two additional ways to fabricate electrodes that are flush with a central fluidic channel. To achieve the geometry shown in Figure 5.2(a), we injected the metal from the two inlets at the left and right ends of the device (not shown) until it reached the intersection with the central fluidic channel. To achieve the geometry shown in Figure 5.2(b), we utilized the same principles used to form the electrodes in Figure 5.1; that is, we injected the metal into channels adjacent to the fluidic channel. The metal fills the electrode channels from the inlets to the outlets (left to right) without leaking through the narrow gap that defines the interface of the metal with the fluidic channel. The microelectrodes in Figure 5.2(b) are easier to form than those shown in 2(a) because it requires less control over the injection process.

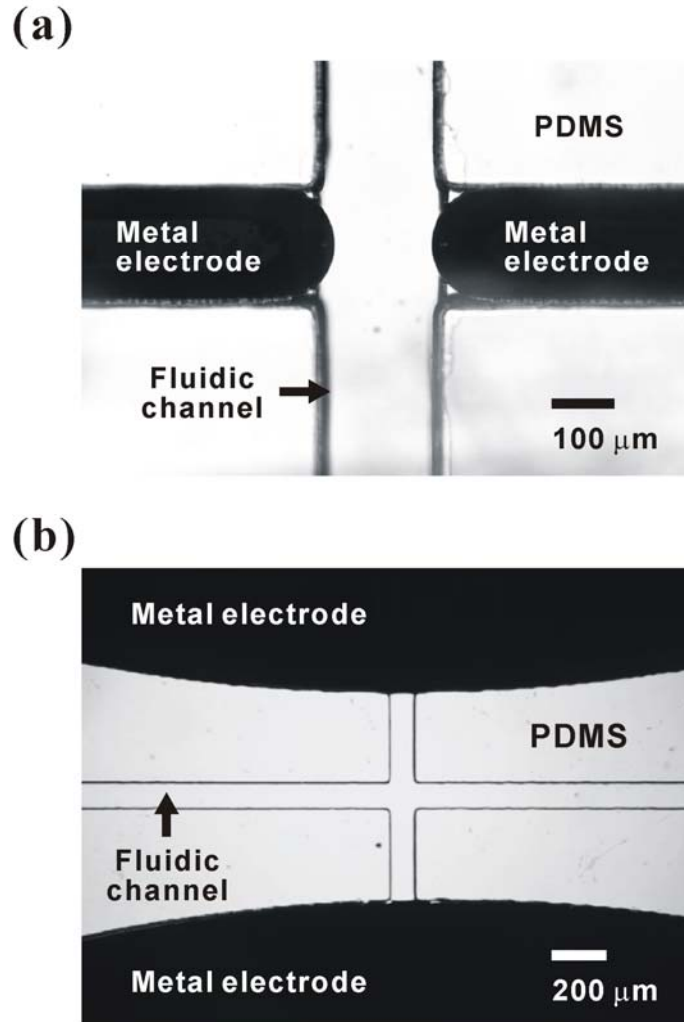


**Figure 5.2** Optical micrograph of microfluidic electrodes. (a) Electrodes flush with the central fluidic channel fabricated by injection. (b) Electrodes recessed from the channel.

We hypothesized that pressure and shear forces originating from flow of fluid within the central fluidic channel could destabilize the oxide skin that otherwise stabilizes the liquid metal. To study the mechanical stability of the metal, we used a microchannel  $\sim 25$  mm long,  $50 \mu\text{m}$  deep, and  $200 \mu\text{m}$  wide (see Figure 5.1) and increased the flow rate of water

until the electrodes failed mechanically. The metal electrodes maintained mechanical stability until the flow rate reached 180  $\mu\text{l}/\text{min}$  (30  $\text{cm}/\text{s}$ ), which is two orders of magnitude greater than the range of flow rate commonly used for microfluidic devices. The pressure in a microfluidic channel decreases from the inlet to the outlet along the length of the channel. The deformation of the electrodes initiates near the inlet of the channel, which supports the concept that pressure is the dominant deformation force. Assuming Poiseuille flow as a first order approximation, the pressure required to achieve this large flow rate is approximately 25 kPa, which corresponds to the critical stress of the metal<sup>[36]</sup> (i.e., the stress required to induce the metal to flow by rupturing the otherwise stabilizing skin that spans between the 50  $\mu\text{m}$  posts). This result suggests that the electrodes are stable provided that the critical pressure is not exceeded. The shear stress originating from the flow can, in principle, also contribute to the deformation of the electrodes. The shear stress at this flow rate is on the order of 1 Pa, which is four orders of magnitude lower than the pressure and is therefore negligible. The ratio between the shear stress and the pressure in a rectangular die has been proposed to depend on the dimensions of the channel in the equation of  $2L(H+W)(HW)^{-1}$  where L, H and W is the length, height and width of the channel, respectively.<sup>[39]</sup> The equation suggests that the shear stress becomes comparable with the pressure only when the length of the microfluidic channel is very short compared to the other dimensions, (e.g., 3  $\mu\text{m}$  long, 100  $\mu\text{m}$  deep, and 100  $\mu\text{m}$  wide, which is both impractical and outside the fully developed flow regime).

We studied the utility and stability of the electrodes in aqueous systems under DC and AC electric biases. We hypothesized that the fluid electrodes should become mechanically

unstable at conditions in which the oxide layer is removed (e.g., by reduction via electric bias). Without the oxide skin, the liquid metal is a high surface tension liquid that will change its shape spontaneously to minimize its surface free energy (i.e. the electrodes will become mechanically unstable). To test the stability, we first fabricated electrodes like those shown in Figure 5.1 and filled the fluidic channel with sodium chloride (NaCl) solutions at a flow rate of 10 ml/min (1.67 cm/s). This flow rate is similar to those used in practical microfluidic applications. We grounded one electrode and applied a bias to the opposing electrode while monitoring the mechanical stability. Most experiments used 0.1 M NaCl solution in the fluidic channel to mimic practical applications that use ionic conducting solutions, such as buffer solutions. The electrodes are stable in deionized water until a large bias ( $>30$  V) is exceeded since pure water is a poor conductor. The added salt ions increase the conductivity of the stream, and thus facilitate the redox reactions at the surfaces of the metal electrodes.

In principle, EGaIn electrodes in the presence of the salt solution should be stable until the applied DC bias exceeds the voltage required to reduce the oxide skin of the metal. According to the Pourbaix diagram, reduction occurs at  $\sim 1$  V relative to SHE at neutral pH (Note that electrolysis of water can also occur at similar operating conditions, which is a problem that limits all types of electrodes since electrolysis can produce bubbles. This problem can be minimized by using flow to carry away electrolysis products before they can nucleate into bubbles).<sup>[40]</sup> **Figure 5.3** (a) is representative of EGaIn electrodes destabilized by an applied relative bias of 2V (we did not use a reference electrode for all of experiments). The DC bias oxidizes the positive electrode and reduces the negative electrode (lower and

upper electrodes, respectively, in Figure 5.3 (a)); only the reduced electrode withdraws because of the absence of the oxide skin. Destabilization is most pronounced near the inlet, which is likely due to the relative large pressure of the salt water at the inlet. The deformation of the reduced electrode can be minimized by sealing the inlets and outlets so there is nowhere for the liquid metal to go, but there is still some withdrawal of the metal due to the flexibility of the walls of the PDMS channel. This problem, however, can be overcome easily by using metals with melting points above the operating temperature so that the electrodes are solid (i.e., frozen at room temperature) during operation. For example, pure gallium (Ga) has a slightly higher melting point (30 °C) than EGaIn (15.7 °C). Thus, it can be injected into microchannels after moderate heating (e.g., warming by hand is sufficient) and cooled down to room temperature where it is solidified to maintain its molded structure even under an electric bias (note: gallium can exist as a liquid in a supercooled state, so it is often necessary to cool it down to -10 °C to freeze it<sup>[41]</sup>). Another convenient alloy for electrodes is a commercially available indium alloy (InBiSn) that has even higher melting point (60 °C). We heated the metal above its melting point to liquefy it and injected it into the microchannels, followed by cooling to room temperature to solidify it again. Figure 5.3 (b) shows that the Ga electrodes are stable even after applying 2 V DC bias, which is in contrast to the EGaIn microelectrodes under the same conditions. InBiSn electrodes are also stable under DC bias.

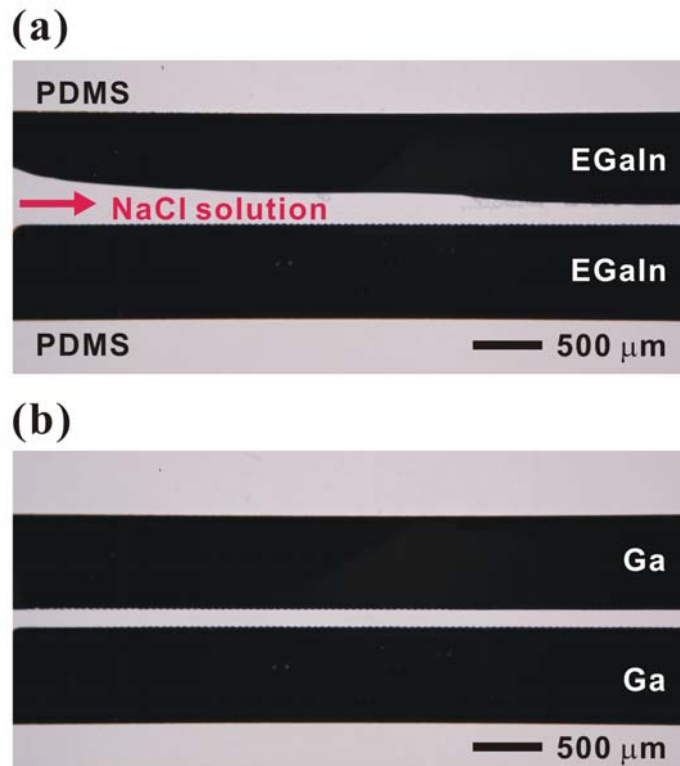


**Figure 5.3** Optical micrographs of the EGaln (a) and Ga (b) electrodes after applying 2 V DC bias for 10 sec. Ga electrodes are stable in the solid state while one EGaln electrode deforms as its thin oxide layer is reduced.

We hypothesized that AC electric fields would minimize the deformation of electrodes composed of EGaln operating at conditions above the threshold voltage since each electrode rapidly alternates between states of oxidation and reduction. The duration of reduction during a single cycle at high AC frequencies should not be sufficiently long to destabilize the metal via reduction of the oxide. **Figure 5.4** (a) and (b) demonstrate the importance of frequency on the stability of EGaln electrodes at 2 V, sinusoidal AC bias with

0.1 M NaCl solution flowing between the electrodes. At low frequencies (0.1 kHz) the electrodes are unstable (Figure 5.4b), whereas the electrodes are stable at higher frequencies (10 kHz) at the same conditions (Figure 5.4c). Whereas only one electrode deforms in the presence of a DC bias (e.g., Figure 5.3a), both of the electrodes (grounded and biased) show deformation in the case of the AC bias since it reduces the oxide layer on both electrodes at low frequency (e.g., Figure 5.4 (b)). The retraction of the metal under AC occurs slowly compared to the DC instability, presumably because the AC instability alternates between stable (oxidized) and unstable (reduced) states. We measured the AC frequency at which the electrode starts deforming as a function of the amplitude of the AC bias. Figure 5.4 (c) shows that the electrodes require higher frequencies to maintain stability as the voltage increases, suggesting that both the duration (i.e., frequency) and driving force (i.e., voltage) dictate the stability of the electrodes. For instance, 20 kHz is sufficient to keep the electrodes stable with 2 V, however it is not enough with 10 V. The voltage affects the rate at which current arrives at the electrodes and therefore the rate of oxidation / reduction. We speculated, therefore, that the stability of the electrodes would also depend on the conductivity of the electrolyte solution between the electrodes. Figure 5.4 (d) shows the effect of ionic concentration of the solution (spanning five orders of magnitude) on the deformation of the electrodes under 10 V AC bias. As expected, fluids with higher ionic concentration require higher frequencies to maintain the mechanical stability of the electrodes. Solid Ga and InBiSn electrodes are stable at room temperature under AC bias under all test conditions (0 to 30 V, 0 to 100 kHz,  $10^{-5}$  to  $10^{-1}$  M NaCl).

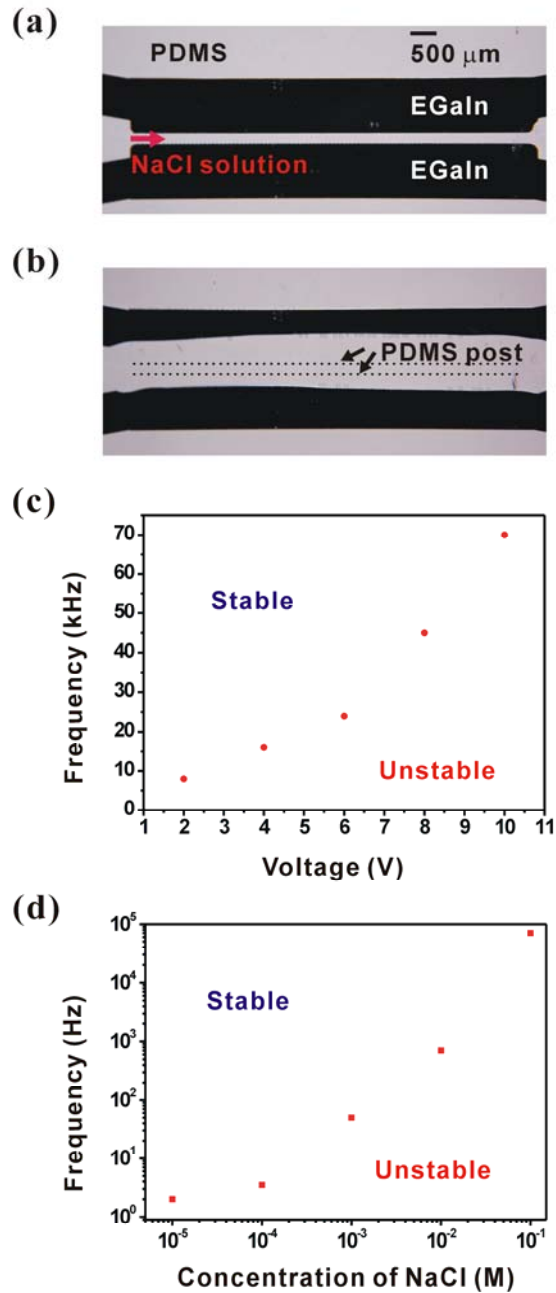


**Figure 5.4** Optical micrographs of EGaIn electrodes under AC sinusoidal electric bias at 2V with two different frequencies 10 kHz (a) and 0.1 kHz (b). The dotted lines in (b) represent the location of PDMS posts and where the metal interface placed before applying bias. The EGaIn electrodes show improved mechanical stability as (c) the AC frequency increases at constant ionic concentration (0.1 M NaCl) and (d) the ionic concentration decreases at constant electric bias (10 V).

We sought to demonstrate the utility of the liquid metal electrodes in an application that requires large electric fields: electrohydrodynamic mixing. Mixing strategies are important for microfluidics because the flow is inherently laminar due to the low Reynolds numbers in the channels. Electrohydrodynamic mixing relies on an interfacial instability that results from the destabilizing effects of electrostatic forces acting normal to the interface between fluids of different electrical properties, such as conductivity and permittivity. As two laminar streams of fluid flow between two parallel electrodes, the electrostatic force generated by applying an electric field between the electrodes induces a transversal flow across the interface between the fluids, causing them to mix. Planar microelectrodes have been used for electrohydrodynamic mixing of adjacent laminar streams in microfluidic channels.<sup>[42, 43]</sup> Injecting the liquid metal into microchannels enables fast and facile construction of the mixer with perfect alignment. As shown in **Figure 5.5** (a), the microfluidic mixer consists of two inherently aligned EGaIn liquid metal electrodes fabricated by injection with a central fluidic channel containing laminar streams of an electrically conducting and an insulating fluid. For the electrically conductive stream, we doped light mineral oil with Stadis 450, which is a commercially available conductivity enhancer and added a commercial dye, Oil Red O, for visualization. A pure light mineral oil comprised the electrically insulating stream. A syringe pump forced the two fluids into the channel at a flow rate of 2  $\mu\text{l}/\text{min}$  each (6.7 mm/s). In the absence of an applied electric field, the two streams assumed laminar flow. Applying 100 V ( $5 \times 10^5$  V/m) DC bias across the two electrodes caused the interface to become unstable, and thus the streams mix readily as shown in Figure 5.5 (b). Since the pure mineral oil is electrically insulating, the reduction

reaction of the metal electrode observed with aqueous solutions can not occur, and thus, the electrodes maintain their mechanical stability even with the high electric bias. The mixing proceeds and halts as the electric field is turned on and off, respectively. This transition happens so fast that it cannot be seen with the naked eye. Solid Ga and InBiSn electrodes showed same result without any deformation of the electrodes under the same electric bias, 100 V.

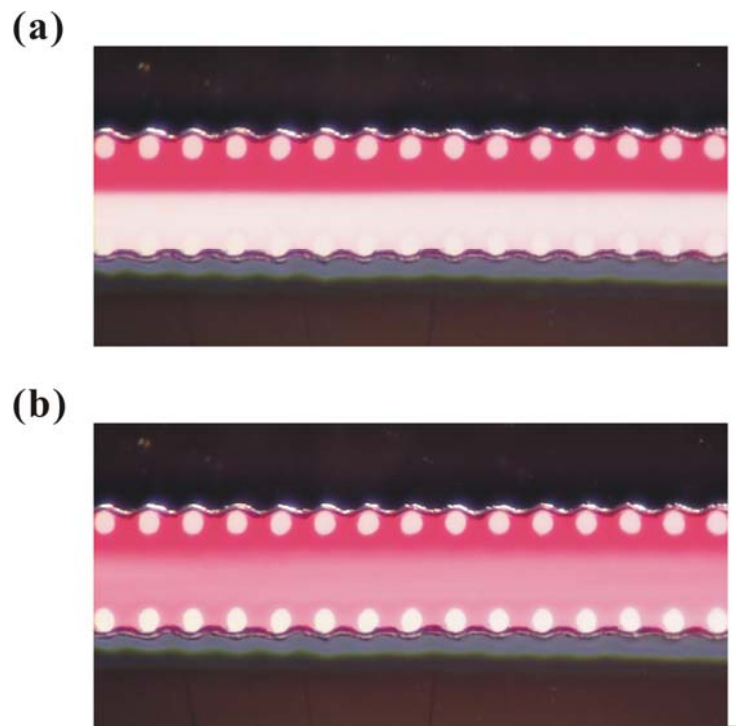


**Figure 5.5** Optical micrographs of EGaIn electrodes for a microfluidic mixer. (a) Two adjacent fluids undergo laminar flow with minimal mixing. The red colored oil is more conductive than the transparent oil. (Note: The PDMS posts are not visible adjacent to the bottom electrode due to index matching. Reflections from the surface of the metal appear as discoloration in these images) (b) The two fluids mix rapidly when 100 V DC bias is applied.

### 5.3 Advantages and Limitations

Injection of liquid metal into microchannels offers a simple method to integrate electrodes into microfluidic devices. Conventionally, external electrical components have to be aligned with microfluidic channels in a manner that is tedious and technically challenging. A distinct advantage of forming these components via fluid injection is that the structures are inherently aligned with other micro-components because all the microchannels are fabricated in a single lithographic step. The aligned liquid metal electrodes span from the top to bottom of the microfluidic channel, providing uniform electric fields to the subjected fluid throughout the height of the channel. The technique is extremely simple and can be accomplished in a single step by hand at room temperature. The metal can be in direct contact with the fluidic channel, which is important for many applications. External electrical contacts with the metal are created by simply touching the liquid with a wire and do not require any solder or special procedures.

The mechanical stability of the liquid electrodes is a limitation of this technique. The oxide layer of the liquid metal, which stabilizes the electrodes, can be ruptured under large pressures or can be reduced under certain pH and electric conditions. According to the Pourbaix diagram, pH value below  $\sim 3$  and above  $\sim 11$  reduce the oxide layer, thus the pH of sample fluids flowing in contact with the metal electrodes should be in the range of  $3 \sim 11$  to prevent the deformation of the electrode. We identified a wide range of operating conditions in which the liquid metal electrodes are stable using both DC and AC biases. Using fluids with low (or negligible) ionic concentration helps to enlarge the range of stable operating conditions. Furthermore, stability can be improved by using metals that can be injected as

liquids, but used during operation as solids (such as Ga or an In alloy). Gallium and indium in the liquid electrodes can form soluble complexes or insoluble salts during both DC and AC operation because of electrochemical reactions at the surface. Thus the liquid electrodes have limited applications in which these complexes or salts do not affect the control or analysis of sample fluids.

#### **5.4 Conclusions**

Injection of liquid metals into microchannels enables fast and facile fabrication of microelectrodes that are aligned with and in direct contact with other microfluidic channels. We found that EGaIn, a low viscosity liquid metal, forms mechanically stable electrodes after being injected into the channels defined in the same lithographic step as the microfluidic channels. The presence of an oxide skin stabilizes the electrodes mechanically despite being composed of a low viscosity liquid, although the rupture (by pressure, for example) or removal of this skin (by reduction, for example) will destabilize the electrodes. We established the range of stable conditions for EGaIn under DC and AC applied electric biases and showed that the metals with melting points above room temperature ensure mechanical stability at all operating conditions explored in this study. An electrohydrodynamic mixer formed using the EGaIn liquid metal electrodes generated an extremely high electric field ( $\sim 10^5 \text{ Vm}^{-1}$ ) sufficient to induce mixing between adjacent laminar streams. In addition to mixing these electrodes may be useful for pumping, sorting and heating; the EGaIn liquid metal does not change its phase in the range of temperature reached by Joule heating and has low vapor pressure.

The microelectrodes have a variety of possible geometries and applications beyond those demonstrated here. For example, placing two electrodes on the same side of a fluidic channel generates diverging electric fields, which can be utilized for dielectrophoresis along the side walls of the channel. The metal could also be extended into the channel to create narrow gaps between the electrodes. Here, we demonstrated microelectrodes in PDMS because it is commonly used for microfluidics, but the liquid metal electrodes could be incorporated into different substrates, such as glass, depending on the desired applications and operating conditions.

## 5.5 References

- [1] K. H. Chung, S. H. Park, Y. H. Choi, *Lab Chip* **2010**, *10*, 202.
- [2] N. Privorotskaya, Y.-S. Liu, J. Lee, H. Zeng, J. A. Carlisle, A. Radadia, L. Millet, R. Bashir, W. P. King, *Lab Chip* **2010**, *10*, 1135.
- [3] B. Selva, P. Mary, M.-C. Jullien, *Microfluid. Nanofluid.* **2010**, *8*, 755.
- [4] D. Vigolo, R. Rusconi, R. Piazza, H. A. Stone, *Lab Chip* **2010**, *10*, 795.
- [5] A. Csordas, A. E. Gerdon, J. D. Adams, J. Qian, S. S. Oh, Y. Xiao, H. T. Soh, *Angew. Chem. Int. Ed.* **2010**, *49*, 355.
- [6] A. Ranzoni, X. J. A. Janssen, M. Ovsyanko, I. L. J. van, M. W. J. Prins, *Lab Chip* **2010**, *10*, 179.
- [7] Y. Yamanishi, S. Sakuma, K. Onda, F. Arai, *Biomed. Microdevices* **2010**, *12*, 745.
- [8] J.-H. So, J. Thelen, A. Qusba, G. J. Hayes, G. Lazzi, M. D. Dickey, *Adv. Func. Mater.* **2009**, *19*, 3632.
- [9] W. Cha, Y.-C. Tung, M. E. Meyerhoff, S. Takayama, *Anal. Chem.* **2010**, *82*, 3300.
- [10] S.-P. Chen, J. Wu, X.-D. Yu, J.-J. Xu, H.-Y. Chen, *Anal. Chim. Acta* **2010**, *665*, 152.
- [11] W. Cheng, N. Klauke, G. Smith, J. M. Cooper, *Electrophoresis* **2010**, *31*, 1405.
- [12] Z. Nie, C. A. Nijhuis, J. Gong, X. Chen, A. Kumachev, A. W. Martinez, M. Narovlyansky, G. M. Whitesides, *Lab Chip* **2010**, *10*, 477.
- [13] D. Chatterjee, H. Shepherd, R. L. Garrell, *Lab Chip* **2009**, *9*, 1219.
- [14] N. Kumari, V. Bahadur, S. V. Garimella, *J. Micromech. Microeng.* **2008**, *18*, 105015/1.
- [15] N. Sasaki, T. Kitamori, H.-B. Kim, *Lab Chip* **2006**, *6*, 550.
- [16] S.-C. Wang, H.-P. Chen, C.-Y. Lee, C.-C. Yu, H.-C. Chang, *Biosens. Bioelectron.* **2006**, *22*, 563.
- [17] S. Debesset, C. J. Hayden, C. Dalton, J. C. T. Eijkel, A. Manz, *Lab Chip* **2004**, *4*, 396.
- [18] F.-Q. Nie, M. Macka, B. Paull, *Lab Chip* **2007**, *7*, 1597.

- [19] B. G. Hawkins, A. E. Smith, Y. A. Syed, B. J. Kirby, *Anal. Chem.* **2007**, *79*, 7291.
- [20] M. Wiklund, C. Gunther, R. Lemor, M. Jager, G. Fuhr, H. M. Hertz, *Lab Chip* **2006**, *6*, 1537.
- [21] P. F. Gavin, A. G. Ewing, *J. Am. Chem. Soc.* **1996**, *118*, 8932.
- [22] M. P. Nagale, I. Fritsch, *Anal. Chem.* **1998**, *70*, 2902.
- [23] O. Ordeig, N. Godino, J. del Campo, F. X. Munoz, F. Nikolajeff, L. Nyholm, *Anal. Chem.* **2008**, *80*, 3622.
- [24] L. Wang, L. A. Flanagan, N. L. Jeon, E. Monuki, A. P. Lee, *Lab Chip* **2007**, *7*, 1114.
- [25] C. K. Harnett, J. Templeton, K. A. Dunphy-Guzman, Y. M. Senousy, M. P. Kanouff, *Lab on a Chip* **2008**, *8*, 565.
- [26] J.-W. Choi, S. Rosset, M. Niklaus, J. R. Adleman, H. Shea, D. Psaltis, *Lab Chip* **2010**, *10*, 783.
- [27] G. H. Kang, K. Y. No, G. M. Kim, *Int. J. Mod. Phys. B* **2006**, *20*, 4493.
- [28] L. Wang, L. Flanagan, A. P. Lee, *J. Microelectromech. Syst.* **2007**, *16*, 454.
- [29] X. Gong, W. Wen, *Biomicrofluidics* **2009**, *3*, 012007.
- [30] N. Lewpiriyawong, C. Yang, Y. C. Lam, *Electrophoresis* **2010**, *31*, 2622.
- [31] X. Z. Niu, S. L. Peng, L. Y. Liu, W. J. Wen, P. Sheng, *Adv. Mater.* **2007**, *19*, 2682.
- [32] A. C. Siegel, S. K. Y. Tang, C. A. Nijhuis, M. Hashimoto, S. T. Phillips, M. D. Dickey, G. M. Whitesides, *Acc. Chem. Res.* **2010**, *43*, 518.
- [33] H. Shafiee, J. Caldwell, M. Sano, R. Davalos, *Biomed. Microdevices* **2009**, *11*, 997.
- [34] A. C. Siegel, D. A. Bruzewicz, D. B. Weibel, G. M. Whitesides, *Adv. Mater.* **2007**, *19*, 727.
- [35] A. C. Siegel, S. S. Shevkoplyas, D. B. Weibel, D. A. Bruzewicz, A. W. Martinez, G. M. Whitesides, *Angew. Chem., Int. Ed.* **2006**, *45*, 6877.
- [36] M. D. Dickey, R. C. Chiechi, R. J. Larsen, E. A. Weiss, D. A. Weitz, G. M. Whitesides, *Adv. Funct. Mater.* **2008**, *18*, 1097.
- [37] R. C. Chiechi, E. A. Weiss, M. D. Dickey, G. M. Whitesides, *Angew. Chem., Int. Ed.* **2008**, *47*, 142.

- [38] Y. Xia, G. M. Whitesides, *Angew. Chem., Int. Ed.* **1998**, 37, 550.
- [39] Y. Son, *Polymer* **2007**, 48, 632.
- [40] M. Pourbaix, *Atlas of Electrochemical Equilibria in Aqueous Solutions - Gallium*, Vol. 16.1, National Association of Corrosion Engineers, Houston, Texas, USA **1974**.
- [41] L. J. Briggs, *J. Chem. Phys.* **1957**, 26, 784.
- [42] H. Lin, *Mech. Res. Commun.* **2009**, 36, 33.
- [43] A. O. El Moctar, N. Aubry, J. Batton, *Lab Chip* **2003**, 3, 273.

## **Chapter 6. Three-dimensional Printing of Free Standing Liquid Metal Microstructures**

## 6.1 Introduction

Interfacial tension limits the ability to pattern liquids into arbitrary shapes both in and out of plane. For example, liquid cylinders with aspect ratios greater than  $\pi$  undergo Rayleigh instabilities that break the liquid into droplets.<sup>[1, 2]</sup> Here, we show it is possible to print a low viscosity liquid metal at room temperature into a variety of stable free-standing 3D microstructures (cylinders with aspect ratios significantly beyond the Rayleigh stability limit, 3D droplet arrays, out of plane arches, wires). A thin ( $\sim 1$  nm thick), passivating oxide skin forms rapidly on the surface of a gallium indium alloy and stabilizes the microstructures despite the low viscosity and large surface energy of the liquid. The ability to directly print liquids with metallic conductivity is important for soft, stretchable, and shape reconfigurable analogs to wires, electrical interconnects, electrodes, antennas, meta-materials, and optical materials.

Arbitrarily controlling the shape of liquids on the microscale is challenging. In the absence of external forces, interfacial tension dominates the behavior of liquids when the capillary number is greater than 1. The interfacial tension dictates the shape and has a number of destabilizing effects on liquids out of mechanical equilibrium. For example, it can cause smaller droplets to coalesce into larger droplets,<sup>[3-5]</sup> jets of liquid to break up into droplets,<sup>[6-11]</sup> and thin films of liquid to destabilize.<sup>[12, 13]</sup> Several techniques have been developed to stabilize the fluids into desirable shapes despite the destabilizing influence of surface tension. The most prevalent approach is to trap the liquid in a non-equilibrium shape by phase transformation of the liquid into solid using, for example, temperature, evaporation, or in the case of polymers crosslinking molecular chains. In general, with the exception of

thermoplastics, the resulting structures are permanently changed and cannot be easily returned to their liquid-like state. Likewise, liquid droplets can be stabilized against coalescence by the inclusion of solid particles, macromolecules, or surfactants on their surface. However, these structures which include, liquid marbles,<sup>[14, 15]</sup> microcapsules,<sup>[16, 17]</sup> colloidosome,<sup>[18, 19]</sup> polymersome and emulsions<sup>[20-22]</sup> typically adopt spherical or semi-spherical shapes. In this chapter we demonstrate a method to pattern a highly conductive liquid anisotropically out of plane in spite of the destabilizing effects of surface tension.

Low-cost and simple methods to produce well-defined 3-D both electrically conductive and insulating microstructures are important for printed electronics on flexible substrates,<sup>[23]</sup> microfluidic networks,<sup>[24-26]</sup> tissue engineering scaffolds<sup>[27, 28]</sup> and photonic band gap structures.<sup>[29, 30]</sup> There are several strategies to pattern 3-D microstructures including standard and soft lithography,<sup>[30-32]</sup> laser based polymerization,<sup>[33]</sup> colloidal or epitaxial assembly<sup>[34, 35]</sup> and direct-write techniques<sup>[24, 26, 28, 36-42]</sup> depending on the comprising substances and their applications. Most work has focused on the patterning of insulating structures, but recently, there has been great interest in new methods to pattern 3-D microstructures of metal.<sup>[36-38, 43]</sup> Direct writing of conductive materials offers an additive method to fabricate conductive 3-D patterns with fine resolution that are useful for electronic devices such as antennas,<sup>[36, 37]</sup> flexible displays<sup>[44-46]</sup> and wire bonds<sup>[38, 43]</sup> and other electronic interconnects in flexible materials that undergo large strains.

Conductive polymers<sup>[47, 48]</sup> or inks containing metal particles extruded through a nozzle or electrodeposited from a conductive tip<sup>[38, 43]</sup> can form solid 3-D micro or nano structures with self-supporting features. However the conductivity of the polymers is

typically much lower than metallic materials, and also, in the case of polymer nanocomposites, the resulting structures exhibit large, sometimes nonlinear changes in their conductivity when stretched. The metal wires formed by extrusion or electrodeposition are often not elastic. For most applications it is desirable to have a higher conductivity than can be provided by particle composite materials or conductive polymers and have predictable resistance changes under strain with minimum of hysteresis.

Previously, microfluidics proved to be a useful method to shape low melting temperature metals for reconfigurable wires and antennas,<sup>[49-53]</sup> interconnects,<sup>[54]</sup> and elements for microfluidics.<sup>[55]</sup> Here, we present a new method to direct-write 3-D, free standing, conductive microstructures comprising the liquid metal, which is a low viscosity and high surface tension liquid at room temperature.

We envision using these liquid metal structures with high conductivity that remain liquid-like at room temperature and can flow in response to stress will be useful for soft, stretchable, or shape reconfigurable electronics. Like injecting metallic liquids into molded microfluidic structures, free standing metal structures can be encased in various types of materials such as elastomers, polymers, or ceramics with different mechanical and electrical properties depending on the desired applications. Since the metal microstructures support themselves without any encapsulation, they can be embedded afterwards. This ability allows the fabrication of 3D complex microstructures inside different castable materials which would be difficult with conventional methods, for example, fabrication of microchannels followed by injection of functional fluids. The encasing material can also be chosen to

determine the mechanical properties of the resulting devices since the liquid metal inside it flows readily in response to strain.

The binary eutectic alloy of gallium and indium (EGaIn, 75% Ga 25% In by weight) is liquid at room temperature (m.p.  $\sim 15.7$  °C<sup>2</sup>) with metallic conductivity.<sup>[56, 57]</sup> The liquid metal exhibits a negligible vapor pressure and low toxicity that allows for safe handling in open air environments.<sup>[58]</sup> Upon exposure to air, EGaIn forms a thin ( $\sim 1$  nm) passivating “skin” composed of gallium oxide which is commonly observed behavior among group III elements and other alloys based on gallium.<sup>[56, 59]</sup> In the presence of the oxide skin, the metal only flows when the critical yield stress is exceeded. Despite the significant mechanical contributions of the oxide skin, electrical resistance seems to remain largely unaffected due to the skin being thin.<sup>[60]</sup> In addition, the liquid metal sticks to most surfaces and alloys with many metals.

The oxide stabilizes the metal mechanically in microchannels despite the large surface tension of the metal.<sup>[59]</sup> Using microfluidics to shape the metal is limited because the channels are in a single plane, whereas many applications (e.g., interconnects, meta-materials, optical materials) require out of plane or 3-D architectures. In addition, the necessity of inlet and outlet ports makes it difficult to pattern arrays of small, discrete structures of the metal via microfluidic injection. Here, we present free standing liquid metal structures such as wires, fibers, interconnects, and stacks and arrays of droplets using four separate methods: (1) Injection into microchannels followed by dissolution of the channel walls, (2) Simultaneously extruding the metal on a substrate while manipulating the position of a supporting stage, (3) Stacking droplets, and (4) Rapidly ejecting the metal from a syringe

to form a continuous liquid metal fiber. We characterize the conditions under which these structures may be formed, elucidate the strength of the extruded wires, and present a working proof-of-concept flexible circuit using liquid metal wire bonds.

## 6.2 Result and Discussion

**Figure 6.1** depicts the general approach to printing liquid metal structures. A free standing straight wire of liquid metal is extruded through a needle connected to a syringe filled with the liquid metal while the substrate is lowered by a motorized translation stage. The syringe is not connected to a pump and the liquid metal flows under hydrostatic pressure due to gravity which is approximately 2 kPa. The metal forms continuous straight wires as the substrate moves away from the syringe at a rate of 50 – 200  $\mu\text{m}/\text{sec}$ . Typically the wires featured a footprint with a diameter larger than the wire diameter, as shown at the base Figure 6.1. The length of these wires can be several cm long and was limited by the travel of the translation stage. The wires, however, can be terminated at any time by apply negative pressure to the syringe (c.f., Figure 6.1). The wires can also be terminated by increasing the vertical rate of displacement of the substrate. Thus a variety of motive forces, i.e. hydrostatic pressure, pneumatic pressure, and volume displacement pumps may be used to control the flow of the metal and lengths of the wire. Once detached from the syringe, the wires maintain their shape.

The maximum draw rate at which the liquid metal forms mechanically stable and continuous wires depends on the diameter of the wire, but slower draw rates proved to be easier to control using the limits of our apparatus. The diameter of the wire is directly

proportional to the diameter of the nozzle. Thinner wires are capable of supporting higher maximum aspect ratio (height to diameter) structures since the ratio of surface area to volume increases as the wire becomes thinner. The diameter of the wires is typically larger than the inner diameter of the needle but smaller than the outer diameter of the needle.



**Figure 6.1.** A series of sequential images in which a syringe needle extrudes liquid metal to form a straight wire on a withdrawn substrate (from left to right). The oxide skin on the surface of the metal stabilizes the liquid metal wire against gravity. The outer diameter of the hollow needle and the extruded wire is 500 and 270  $\mu\text{m}$ , respectively. The length of the final wire shown is 8 mm before it was intentionally ended by applying vacuum to the syringe.

The mechanical stability of the straight wires gives insight into the physical contribution of the oxide skin on the liquid structure and dictates their robustness in practical applications. We prepared different dimensions of straight wires on a glass substrate and observed the tilt angle at which they toppled (we define an angle of zero to occur when the wires are aligned parallel to gravity). As expected, the angle at which the wires collapse

decreases as the height of the wires increases. For example, a wire 3 mm tall and 100  $\mu\text{m}$  in diameter did not collapse even at  $90^\circ$  and remained stable when the substrate was upside down. In contrast, wires of 4.5 mm and 5 mm in height with the same diameter collapsed at  $22^\circ$  and  $8^\circ$ , respectively. The diameter of the wires also affects their mechanical stability since thicker wires have a bigger footprint on the substrate. We compared mechanical stability of the wires of 100  $\mu\text{m}$  and 230  $\mu\text{m}$  in diameter with the same height (5 mm). The thicker one collapsed at an angle twice as large as the thinner wire since it has bigger footprint at the base of the wire. In addition to slowly expelling the metal while it is in contact with a substrate, it is possible to form free standing liquid metal microstructures in at least three additional methods: (1) Rapidly expelling the metal to form a liquid metal filament, (2) Expelling droplets from the syringe and stacking them sequentially and (3) Injecting the metal into microchannels and subsequently removing the channels. The structures in **Figure 6.2a** and **2b** rely on rapidly expelling the metal from the syringe using bursts of pressure. The resulting structures are fibers composed of liquid metal that are tens of micrometers in diameter, which form in milliseconds. In **Figure 6.2a**, the fiber spans from a microsyringe to the substrate and in **Figure 6.2b**, the resulting fiber is strong enough to span across a large gap without support. The fibers in **Figure 6.2a** naturally form a bead upon hitting the surface, which may be useful for forming contact pads.

**Figure 6.2c** relies on extruding the metal from a syringe in a slow and controlled manner while simultaneously increasing the distance between the syringe and the substrates. This process can fabricate 3-D microstructures of the liquid metal such as wires, arches, and bridges. The structure in **Figure 6.2c** forms in a manner identical to those in **Figure 6.1**, but is

bent mechanically to form an arch using the motion of the stage. Without optimization, these fibers have a nearly uniform diameter (with some observed beading). Figures 2d and 2e involve forming liquid metal droplets and assembling them into 3-D microstructures by stacking them individually. Figure 6.2d is a tower of 17 metal droplets and Figure 6.2(e) shows a  $3 \times 3 \times 3$  array of droplets of approximately  $500 \mu\text{m}$  in diameter. When the droplets touch each other, they do not merge into one bigger droplet but form a physical and electrical contact by breaking only in a portion of their oxide skin.

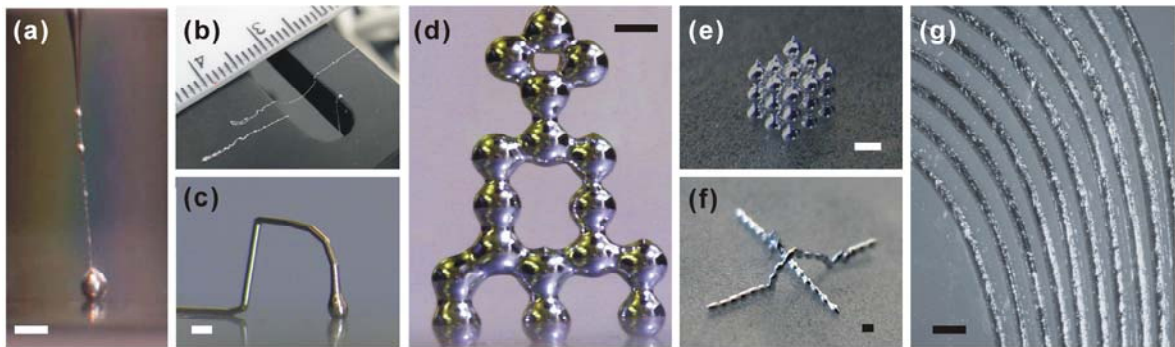


**Figure 6.2.** Photographs of the diverse free standing, liquid metal microstructures. (a) Liquid metal spouted rapidly from a glass capillary forms a thin wire. (b) Suspended liquid metal fibers formed by rapidly extruding the metal from a syringe. The fiber is strong enough to suspend over a gap. (c) A free standing liquid metal arch structure spanning  $\sim 3$  mm. (d) Tower, (e)  $3 \times 3 \times 3$  cube array and (f) crossover lines composed of liquid metal droplets. The droplets act as building blocks and form continuous physical and electrical junctions. (g) An array of in-plane lines of free standing liquid metal fabricated by filling a microchannel with the metal and removing the mold. Scale bars represent  $500 \mu\text{m}$ .

Removing microfluidic molds after injection of the liquid metal offers another way of fabricating free standing 3-D microstructures. We injected the liquid metal into a 10-turn, coil-shaped PDMS microchannel that is  $200 \mu\text{m}$  in width and height, and then dissolved the PDMS mold in 1.0 M tetrabutylammonium fluoride (TBAF) / dimethylformamide (DMF)

solution (Figure 6.2 (f)). The patterned metal lines maintain their mechanical stability due to the oxide skin even after removing completely the polymer casing.

Characterizing the mechanical properties of the liquid microstructures with various extrusion processes allows for the assessment of the feasibility and scope of possible practical applications of the structures as well as better understanding of the mechanics of the extrusion process. Since the free standing structures consist of liquid covered with a thin oxide skin, their mechanical stability solely depends on the surface oxide skin. Thus, the mechanical properties of the structures can be correlated with the mechanical properties of the surface oxide of the metal. The surface oxide has been reported to undergo sudden failure at a certain critical stress.<sup>[59]</sup> We modeled the oxide layer of an extruded wire as a thin, radially symmetric shell with uniform thickness. When tension is applied to the structure, the stress within the oxide shell can be approximated using the equation (1), where  $F$  is the applied force,  $r$  is the minimum radius of the extruded wire, and  $\sigma$  is the tensile stress.

$$F = 2\pi r\sigma \quad (1)$$

We measured the tensile force required to neck the wire structures using a 32 gauge needle as a cantilever. We calibrated the force by measuring the deflection imposed by various sizes of droplets at the end of the needle and then measured the deflection of the needle while stretching wires composed of liquid metal. **Figure 6.3** shows the force as a function of minimum circumference of the wire for a number of samples. The slope of the fitted line is 0.77 N/m which is close to the previously reported value of critical stress of the oxide ( $\sim 0.5$  N/m) measured using a rheometer in shear mode.<sup>[59]</sup> Correcting for differences in geometry, these values are nearly identical.

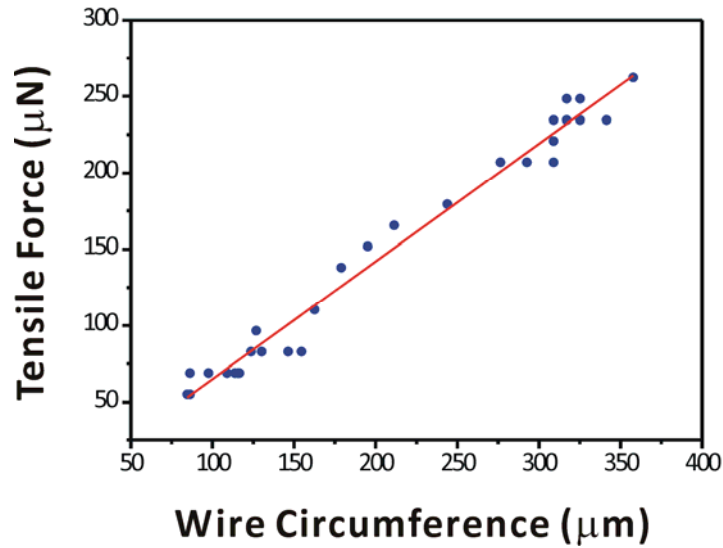


**Figure 6.3.** Observed (dot) and fitted (line) tensile force as a function of the minimum circumference of the extruded wire. The slope of the graph represents the stress required to yield the surface oxide skin during the extrusion process, which is  $\sim 0.77$  N/m

We believe the tensile forces of the moving stage cause the metal wire to elongate. Because the liquid forms a skin, the capillary forces do not act to collapse the fiber. Thus, as long as the internal pressure is sufficient to force the metal into the extruded tube, it maintains stability. However, the pressure inside the wire must be small enough to prevent it from expanding radially to form beads. Studies on the experimental conditions where stable wires forms without bulging or necking are underway.

Encasing the free standing liquid metal structures with other materials such as polymers, elastomers and ceramics may be desirable due to ease of handling, device durability, as well as tuning the mechanical properties depending on the applications. Since the metallic conducting part is liquid, the encasing material dictates the mechanical properties of the resulting devices. To demonstrate an application of liquid metal wires for

stretchable electronics (i.e., electronics that function while being elongated), we embedded the wires in polydimethylsiloxane (PDMS) (**Figure 6.4**). A micrograph of the wire in PDMS (Figure 6.4(a), inset) shows a wire bond composed of liquid metal droplets connecting two surface mounted LEDs which are  $\sim 5$  mm away from each other. The liquid metal bridge connecting the LEDs functioned up to the strain limit of PDMS (Figure 6.4(b),  $\sim 35\%$  strain) and while being flexed (Figure 6.4(c), (d)) without losing its electrical continuity.

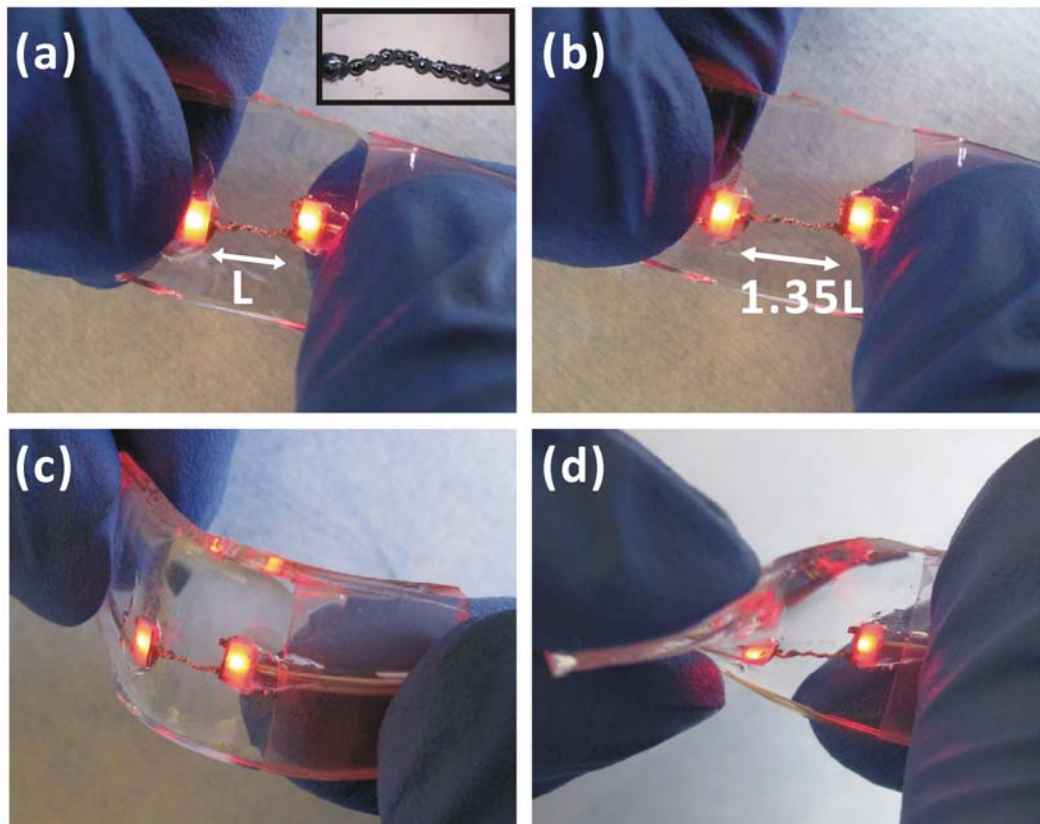


**Figure 6.4.** (a) A prototype device composed of two LEDs and stretchable wire bonds connecting them in PDMS (Inset: Micrograph of the liquid metal wire bonds). (b-d) The fluidic property of the metal wire in the elastomer allows stretchability (b) and flexibility (c, d) of the device and keeps its electrical continuity.

### **6.3 Conclusion**

In summary, we described a method to direct write 3-D, free standing, liquid metal microstructures by four different methods including extruding the liquid metal through a capillary or removing mold after injection of the metal into microchannels. Although the liquid metal microstructures are not as robust as solid structures, the thin oxide layer on the surface of the metal allows for the formation of mechanically stable structures strong enough to stand against gravity and the larger surface tension of the liquid. We demonstrated the feasibility of the microstructures to form stretchable wire bonds where the fluidic properties of the metal facilitate deformation without losing electrical continuity. We expect that other types of encasing materials such as castable plastics, ceramics, resins and gels could provide new functionalities with the liquid metal microstructures. We also believe skin forming liquids represent a new method to pattern liquids into shapes previously prohibited by the destabilizing effects of surface tension. Here, we patterned free standing liquid wires in and out of plane with aspect ratios more than 100 times greater than the Rayleigh stability limit.

## 6.4 References

- [1] L. Rayleigh, *P. R. Soc. London* **1879**, 29, 71.
- [2] L. Rayleigh, *Philos. Mag. Series 5* **1892**, 34, 145.
- [3] D. J. Chen, R. Cardinaels, P. Moldenaers, *Langmuir* **2009**, 25, 12885.
- [4] B. M. Jose, T. Cubaud, *Microfluid. Nanofluid.* **2012**, 12, 687.
- [5] L. Mazutis, A. D. Griffiths, *Lab Chip* **2012**, 12, 1800.
- [6] Y. Christanti, L. M. Walker, *J. Non-Newton. Fluid* **2001**, 100, 9.
- [7] J. Eggers, *Rev. Mod. Phys.* **1997**, 69, 865.
- [8] J. Eggers, E. Villermaux, *Rep. Prog. Phys.* **2008**, 71.
- [9] E. F. Goedde, M. C. Yuen, *J. Fluid Mech.* **1970**, 40, 495.
- [10] S. P. Lin, R. D. Reitz, *Annu. Rev. Fluid Mech.* **1998**, 30, 85.
- [11] D. T. Papageorgiou, *Phys. Fluids* **1995**, 7, 1529.
- [12] D. A. Edwards, A. Oron, *J. Fluid Mech.* **1995**, 298, 287.
- [13] S. Kumar, O. K. Matar, *J. Colloid Interf. Sci.* **2004**, 273, 581.
- [14] P. Aussillous, D. Quere, *Nature* **2001**, 411, 924.
- [15] A. Mitchinson, *Nature* **2010**, 464, 497.
- [16] J. Zhang, R. J. Coulston, S. T. Jones, J. Geng, O. A. Scherman, C. Abell, *Science* **2012**, 335, 690.
- [17] H. Liu, C. Wang, Q. Gao, Z. Tong, *Prog. Chem.* **2008**, 20, 1044.
- [18] O. J. Cayre, J. Hitchcock, M. S. Manga, S. Fincham, A. Simoes, R. A. Williams, S. Biggs, *Soft Matter* **2012**, 8, 4717.
- [19] J. W. O. Salari, G. T. Jemwa, H. M. Wyss, B. Klumperman, *Soft Matter* **2011**, 7, 2033.
- [20] R. Aveyard, B. P. Binks, J. H. Clint, *Adv. Colloid Interfac.* **2003**, 100, 503.
- [21] R. Aveyard, J. H. Clint, T. S. Horozov, *Phys. Chem. Chem. Phys.* **2003**, 5, 2398.

- [22] Y. Nonomura, N. Kobayashi, N. Nakagawa, *Langmuir* **2011**, *27*, 4557.
- [23] V. Subramanian, J. M. J. Frechet, P. C. Chang, D. C. Huang, J. B. Lee, S. E. Molesa, A. R. Murphy, D. R. Redinger, *P. IEEE* **2005**, *93*, 1330.
- [24] W. Wu, A. DeConinck, J. A. Lewis, *Adv. Mater.* **2011**, *23*, H178.
- [25] A. P. Esser-Kahn, P. R. Thakre, H. Dong, J. F. Patrick, V. K. Vlasko-Vlasov, N. R. Sottos, J. S. Moore, S. R. White, *Adv. Mater.* **2011**, *23*, 3654.
- [26] K. S. Toohey, N. R. Sottos, J. A. Lewis, J. S. Moore, S. R. White, *Nat. Mater.* **2007**, *6*, 581.
- [27] D. W. Hutmacher, *Biomaterials* **2000**, *21*, 2529.
- [28] J. N. H. Shepherd, S. T. Parker, R. F. Shepherd, M. U. Gillette, J. A. Lewis, R. G. Nuzzo, *Adv. Funct. Mater.* **2011**, *21*, 47.
- [29] A. Blanco, E. Chomski, S. Grabtchak, M. Ibisate, S. John, S. W. Leonard, C. Lopez, F. Meseguer, H. Miguez, J. P. Mondia, G. A. Ozin, O. Toader, H. M. van Driel, *Nature* **2000**, *405*, 437.
- [30] M. Campbell, D. N. Sharp, M. T. Harrison, R. G. Denning, A. J. Turberfield, *Nature* **2000**, *404*, 53.
- [31] J. R. Anderson, D. T. Chiu, R. J. Jackman, O. Cherniavskaya, J. C. McDonald, H. K. Wu, S. H. Whitesides, G. M. Whitesides, *Anal. Chem.* **2000**, *72*, 3158.
- [32] M. Geissler, Y. Xia, *Advanced Materials* 2004, *16*, 1249.
- [33] B. H. Cumpston, S. P. Ananthavel, S. Barlow, D. L. Dyer, J. E. Ehrlich, L. L. Erskine, A. A. Heikal, S. M. Kuebler, I. Y. S. Lee, D. McCord-Maughon, J. Q. Qin, H. Rockel, M. Rumi, X. L. Wu, S. R. Marder, J. W. Perry, *Nature* **1999**, *398*, 51.
- [34] S. O. Kim, H. H. Solak, M. P. Stoykovich, N. J. Ferrier, J. J. de Pablo, P. F. Nealey, *Nature* **2003**, *424*, 411.
- [35] L. J. Lauhon, M. S. Gudiksen, C. L. Wang, C. M. Lieber, *Nature* **2002**, *420*, 57.
- [36] J. J. Adams, E. B. Duoss, T. F. Malkowski, M. J. Motala, B. Y. Ahn, R. G. Nuzzo, J. T. Bernhard, J. A. Lewis, *Adv. Mater.* **2011**, *23*, 1335.
- [37] J. J. Adams, S. C. Slimmer, T. F. Malkowski, E. B. Duoss, J. A. Lewis, J. T. Bernhard, *IEEE Antenn. Wirel. Pr.* **2011**, *10*, 1425.

- [38] B. Y. Ahn, E. B. Duoss, M. J. Motala, X. Guo, S.-I. Park, Y. Xiong, J. Yoon, R. G. Nuzzo, J. A. Rogers, J. A. Lewis, *Science* **2009**, *323*, 1590.
- [39] B. Y. Ahn, D. J. Lorang, E. B. Duoss, J. A. Lewis, *Chem. Comm.* **2010**, *46*, 7118.
- [40] B. Y. Ahn, D. Shoji, C. J. Hansen, E. Hong, D. C. Dunand, J. A. Lewis, *Adv. Mater.* **2010**, *22*, 2251.
- [41] S. T. Parker, P. Domachuk, J. Amsden, J. Bressner, J. A. Lewis, D. L. Kaplan, F. G. Omenetto, *Adv. Mater.* **2009**, *21*, 2411.
- [42] D. Therriault, S. R. White, J. A. Lewis, *Nat. Mater.* **2003**, *2*, 265.
- [43] J. Hu, M.-F. Yu, *Science* **2010**, *329*, 313.
- [44] G. H. Gelinck, H. E. A. Huitema, E. Van Veenendaal, E. Cantatore, L. Schrijnemakers, J. Van der Putten, T. C. T. Geuns, M. Beenhakkers, J. B. Giesbers, B. H. Huisman, E. J. Meijer, E. M. Benito, F. J. Touwslager, A. W. Marsman, B. J. E. Van Rens, D. M. De Leeuw, *Nat. Mater.* **2004**, *3*, 106.
- [45] J. A. Rogers, Z. Bao, K. Baldwin, A. Dodabalapur, B. Crone, V. R. Raju, V. Kuck, H. Katz, K. Amundson, J. Ewing, P. Drzaic, *P. Natl. Acad. Sci. USA* **2001**, *98*, 4835.
- [46] C. D. Sheraw, L. Zhou, J. R. Huang, D. J. Gundlach, T. N. Jackson, M. G. Kane, I. G. Hill, M. S. Hammond, J. Campi, B. K. Greening, J. Francl, J. West, *Appl. Phys. Lett.* **2002**, *80*, 1088.
- [47] J. T. Kim, J. Pyo, J. Rho, J.-H. Ahn, J. H. Je, G. Margaritondo, *ACS Macro Lett.* **2012**, *1*, 375.
- [48] J. T. Kim, S. K. Seol, J. Pyo, J. S. Lee, J. H. Je, G. Margaritondo, *Adv. Mater.* **2011**, *23*, 1968.
- [49] G. J. Hayes, J. H. So, A. Qusba, M. D. Dickey, G. Lazzi, *IEEE T. Antenn. Propag.* **2012**, *60*, 2151.
- [50] M. R. Khan, G. J. Hayes, J. H. So, G. Lazzi, M. D. Dickey, *Appl. Phys. Lett.* **2011**, *99*.
- [51] M. Kubo, X. Li, C. Kim, M. Hashimoto, B. J. Wiley, D. Ham, G. M. Whitesides, *Adv. Mater.* **2010**, *22*, 2749.
- [52] J.-H. So, J. Thelen, A. Qusba, G. J. Hayes, G. Lazzi, M. D. Dickey, *Adv. Funct. Mater.* **2009**, *19*, 3632.

- [53] S. Cheng, A. Rydberg, K. Hjort, Z. Wu, *Appl. Phys. Lett.* **2009**, *94*, 144103.
- [54] H.-J. Kim, C. Son, B. Ziaie, *Appl. Phys. Lett.* **2008**, *92*, 011904/1.
- [55] J.-H. So, M. D. Dickey, *Lab Chip* **2011**, *11*, 905.
- [56] S. J. French, D. J. Saunders, G. W. Ingle, *J. Phys. Chem.* **1938**, *42*, 265.
- [57] D. Zrnica, D. S. Swatik, *J. Less-Common Met.* **1969**, *18*, 67.
- [58] D. R. Lide, *CRC Handbook of Chemistry and Physics*, Taylor and Francis, FL, Boca Raton, **2007**.
- [59] M. D. Dickey, R. C. Chiechi, R. J. Larsen, E. A. Weiss, D. A. Weitz, G. M. Whitesides, *Adv. Funct. Mater.* **2008**, *18*, 1097.
- [60] L. Cademartiri, M. M. Thuo, C. A. Nijhuis, W. F. Reus, S. Tricard, J. R. Barber, R. N. S. Sodhi, P. Brodersen, C. Kim, R. C. Chiechi, G. M. Whitesides, *J. Phys. Chem. C* **2012**, *116*, 10848.

# **Chapter 7. Tuning the Interfacial Rheological Properties of Eutectic Gallium Indium**

## 7.1 Introduction

This chapter characterizes the mechanical properties of a thin oxide skin that forms on a gallium-based liquid metal alloy<sup>[1, 2]</sup> and the significant changes to these properties in response to changes in the chemical environment surrounding the metal. The metal, eutectic gallium indium (EGaIn) is a liquid at room temperature and forms an oxide skin rapidly under atmospheric conditions.<sup>[2, 3]</sup> This thin oxide skin allows the liquid metal to be micromolded into stable, non-spherical shapes and structures.<sup>[4]</sup> The ability to shape this liquid metal into useful structures holds great promise for forming stretchable and reconfigurable antennas,<sup>[5-8]</sup> microelectrodes,<sup>[9]</sup> interconnects,<sup>[10]</sup> tunneling junctions with self assembled monolayers.<sup>[4, 11]</sup>

Previous rheological measurements confirm the elastic nature of the skin below a critical yield stress (i.e., the stress that causes the skin to rupture and the metal to flow).<sup>[12]</sup> The ability to shape or re-shape the metal relies on the ability to rupture the skin to allow the metal to flow in a controlled manner. This property is particularly important for applications in which the metal is designed to change shape on demand for stimuli responsive devices.<sup>[7, 8]</sup> In this chapter, we describe how to control and modify the mechanical properties of the skin (i.e., the elastic modulus and the critical yield stress).

We manipulate and measure the mechanical properties of the oxide skin by exposing the metal to different chemical environments using a magnetic bearing rheometer with a parallel plate geometry. Rheological analysis is typically used to characterize bulk properties of fluids. In our current study, all the unusual properties arise from the thin solid skin on the liquid metal surface. Here, the bulk liquid is of low viscosity (two times that of water)<sup>[13]</sup>, so

the oxide skin dominates the mechanical properties. The oxide is known to be elastic below a critical yield stress, above which, the metal flows readily.

We aim to modify the yield properties of the liquid metal under different chemical environments and characterize them in a set of small amplitude oscillatory shear experiments. Initially, we compare the properties of EGaIn in air, aqueous, and acidic environments. We show that water and acid both weaken the oxide skin, but it can recover its properties upon drying.

## 7.2 Mathematical relationships<sup>[14, 15]</sup>

In a typical small amplitude oscillatory shear experiment, the top plate is rotated with a strain defined as,

$$\gamma = \gamma_0 \sin \omega t \dots\dots\dots(1)$$

The resulting oscillating stress from this strain is given by,

$$\sigma = \sigma_0 \sin(\omega t + \delta) \dots\dots\dots(2)$$

Here,  $\gamma_0$  and  $\sigma_0$  are the strain and stress amplitude,  $\omega$  is the frequency of oscillation and  $\delta$  is the phase difference between the strain and stress. The resulting stress has two components and is related with the elastic modulus and viscous modulus as,

$$\text{Elastic modulus, } G' = \left(\frac{\sigma_0}{\gamma_0}\right) \cos \delta \dots\dots\dots(3)$$

$$\text{Viscous modulus, } G'' = \left(\frac{\sigma_0}{\gamma_0}\right) \sin \delta \dots\dots\dots(4)$$

The elastic modulus is in phase with the strain and the viscous modulus is out of phase with the strain. In a period of oscillation, the elastic modulus represents the stored energy in the material while the viscous modulus represents the dissipated energy of the material. For a perfectly elastic material, strain and stress are in phase (i.e., no phase lag) and the elastic modulus has some finite value with no viscous component. For a purely viscous material, stress is leading by a 90° phase angle and the viscous modulus has a finite value with no elastic component. Most materials share properties of these two extreme materials and are known as viscoelastic.

In a typical rheological experiment (i.e., oscillatory stress sweep in this study) equation (2)-(4) represents the bulk properties of a material. In our study, however, all the rheological properties arise from the surface of liquid metal rather than from bulk metal, which is of low viscosity liquid. The rheometer assumes it is measuring a bulk property and converts torque and strain to bulk stress and modulus. It also assumes that the sample (i.e., the metal) fills completely to the outer diameter of the top plate. Thus, we have to develop relationships to convert bulk stress and modulus for an assumed 40 mm plate to that of a surface stress and modulus using 20 mm of material. All the bulk properties (stress, modulus) of the metal can be converted to surface properties by using the following correlations.

$$\text{Surface stress, } \sigma_s = K \times C \times \sigma_B \dots\dots\dots(5)$$

Here, K is the plate correction factor, which arises due to differences between the actual diameter of the sample and the diameter of the top plate. Typically, we use a 40 mm (diameter) top plate loaded only up to 20 mm (diameter) due to the expense of the metal.

This constant is equal to  $\left[ \frac{\text{Plate Dia}}{\text{Sample Dia}} \right]^3$ . If the sample is loaded perfectly inside the 40 mm plate then this factor is equal to 1. C is a conversion factor that converts bulk properties into surface properties. It is equal to (D/8), in which D (m) is the diameter of the sample.  $\sigma_B$  is the bulk stress (Pa) value calculated by the instrument.

The bulk moduli (G' and G'') can be converted to surface moduli using the following correlation,

$$G'_s = \left( \frac{R_{plate}}{8} \right) \times G'_B \dots\dots\dots(6)$$

here  $G'_s$  is the surface elastic modulus,  $G''_B$  is the bulk elastic modulus and  $R_{plate}$  is the radius of the top plate in meters. The viscous modulus (G'') can be converted using the same scaling. We derive the correlation for stress by equating the surface torque of the metal to the bulk torque. We derive the correlations for modulus using,

$$\text{Stress, } \sigma = G' \gamma + (G'' / \omega) \cdot \dot{\gamma} \dots\dots\dots(7)$$

where,  $\gamma = \text{Strain} = \frac{\text{Radius} \times \text{angular Displacement}}{\text{Gap between top and bottom Plate}}$ , and

$$\dot{\gamma} = \text{Strain rate} = \frac{\text{angular velocity} \times \text{Radius}}{\text{Gap between top and bottom Plate}}$$

### 7.3 Experimental Section

We used an AR-G2 rheometer (TA Instruments) with a parallel plate geometry for all of the experiments. The bottom plate, which contains a Peltier element for temperature control, is stationary and the top plate can rotate with an angular frequency set by the low friction

bearing motor of the stress controlled rheometer. The two plates sandwich the sample (in this case, EGaIn), which undergoes shear flow due to the movement of the top plate. All the measurements use EGaIn (99.99%, from MMM). **Figure 7.1** provides a schematic of the rheometer setup. A custom-made acrylic reservoir provides a vessel into which liquids may be added in intimate contact with the liquid metal.

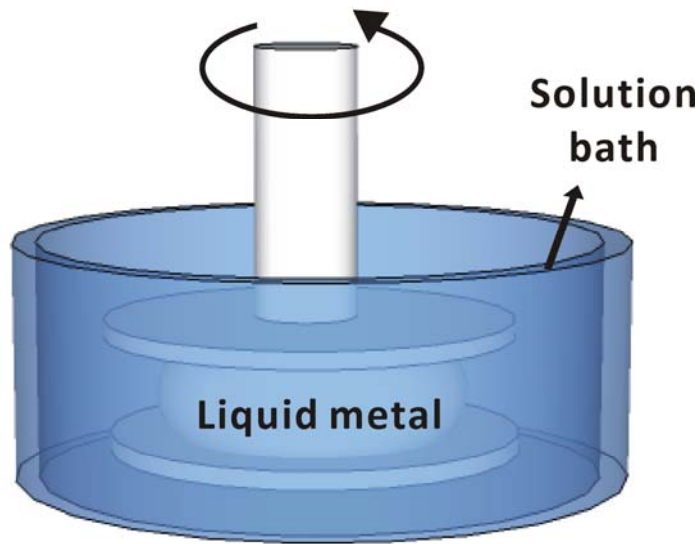


**Figure 7.1** A schematic of the experimental setup. EGaIn is sandwiched between an oscillating top plate and a stationary bottom plate. All the resistance to top plate movement is generated by the skin on EGaIn and the instrument measures the strain ( $\gamma$ ) while controlling stress ( $\sigma$ , Pa). To test EGaIn in different chemical environments, an acrylic reservoir fits firmly with the dummy bottom plate. The reservoir is filled with different liquids, which we call the “surrounding liquids”, to quantify their effect on the mechanical properties of the skin on EGaIn.

In a typical experiment, we sandwich 1 ml of EGaIn between the plastic top plate which is 40 mm in diameter and dummy bottom plate and set the gap as 1500  $\mu\text{m}$ . Since all the rheological properties in this case arise from the surface of the liquid metal rather than

from the bulk metal, all the bulk fluid rheological data are converted to interface rheological data (i.e., modulus and stress (N/m) instead of bulk modulus and stress (Pa)). The conversion process is described in the previous section (Chapter 7.2). In an oscillatory stress sweep test, we scanned the sample from an oscillating stress (bulk) ( $\sim 10^{-3}$  Pa) to a high value (15 - 30 Pa) at an angular frequency of 1 rad/s without any pre-shearing in log mode (10 points per decade) at room temperature. Before each experiment, we calibrated the instrument to account for the inertia of the plate and bearing and zeroed the gap between the top and bottom plates.

#### 7.4 Results and Discussion

We hypothesized that the surface modulus and yield stress of the oxide skin on EGaIn would change in different chemical environment as the oxide skin changes its thickness and/or composition. Before testing our hypothesis, we sought to establish our experimental techniques by first repeating rheological measurements of the metal in air from the literature. **Figure 7.2** shows a representative plot of the rheological behavior of EGaIn in air which is in a good agreement with the literature<sup>[2]</sup>. We measured the modulus after filling the acrylic reservoir with deionized water (DI water) while maintaining the same experimental conditions and geometry as that used in air. Since, the metal squirts out between the plates at higher oscillating bulk stresses ( $\sim 30$  Pa), we limited the stress between 0.001 to 15 Pa without any pre-shearing of the sample. The elastic modulus decreases by an order of magnitude ( $\sim 1$  N/m) relative to that measured in air ( $\sim 10$  N/m). The yield stress of the metal also shifts to a lower value in water compared to that in air. In air, it yields at  $\sim 0.54$  N/m but

it drops down to  $\sim 0.1$  N/m in water. This result suggests the oxide skin is either changing its composition, or getting thinner in water compared to that in air. According to studies of gallium as a dental filling, gallium forms a gelatinous complex of gallium oxide monohydroxides ( $\text{GaOOH}$ ) in water<sup>[16]</sup>, which suggests that the oxide changes its composition in the presence of water. This result is very promising since it suggests that modulus of the skin can be lowered by an order of magnitude and also the yield stress by a factor of 5, simply by exposing it to water.

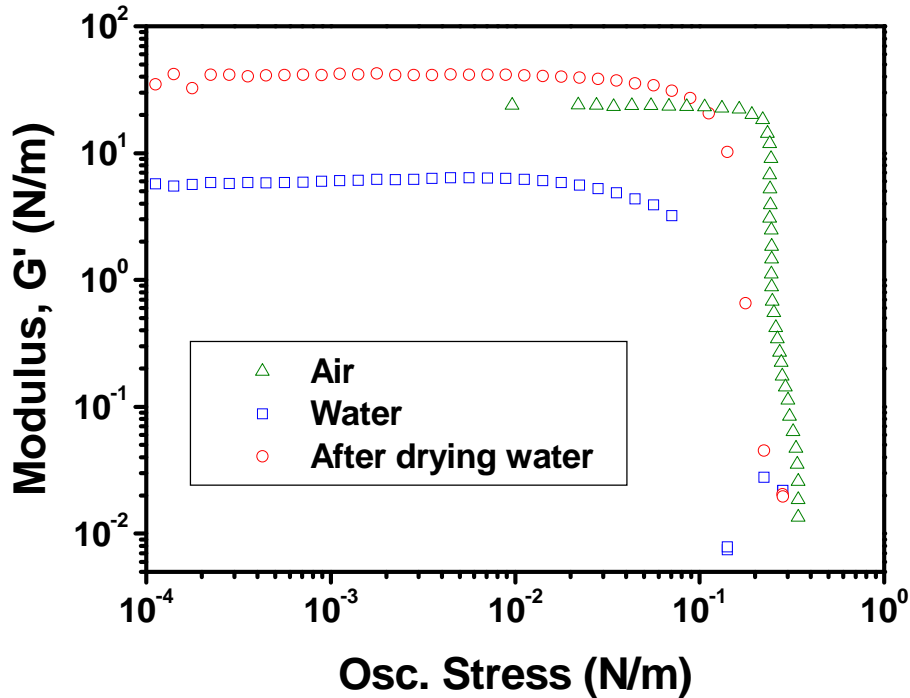


**Figure 7.2** Oscillatory stress sweep of EGaIn in air, water and after drying. All the reported values are for surface modulus. The elastic modulus plateaus before the liquid metal yields beyond a critical stress. The elastic modulus decreases by an order of magnitude in water. The yield stress is also reduced by approximately a factor of three. The elastic modulus and yield stress of the dried metal is higher than the elastic modulus of the metal in water.

We sought to understand what happens to the mechanical properties of the skin that forms on EGaIn when it returns to a dry state after being submerged in water. We allowed the water to evaporate (waiting more than 96 hours) at room temperature. EGaIn exhibits a slightly higher elastic modulus ( $\sim 20$  N/m) than in air ( $\sim 10$  N/m) or water ( $\sim 1$  N/m). The elastic modulus increases by 2 times that in air and 20 times that in water. The oxidation product of gallium oxide monohydroxides in air may be contributing to this increase in elastic modulus. The yield stress decreased significantly in water relative to that in air. In contrast, the fully dried sample showed negligible change in yield stress relative to that in air.

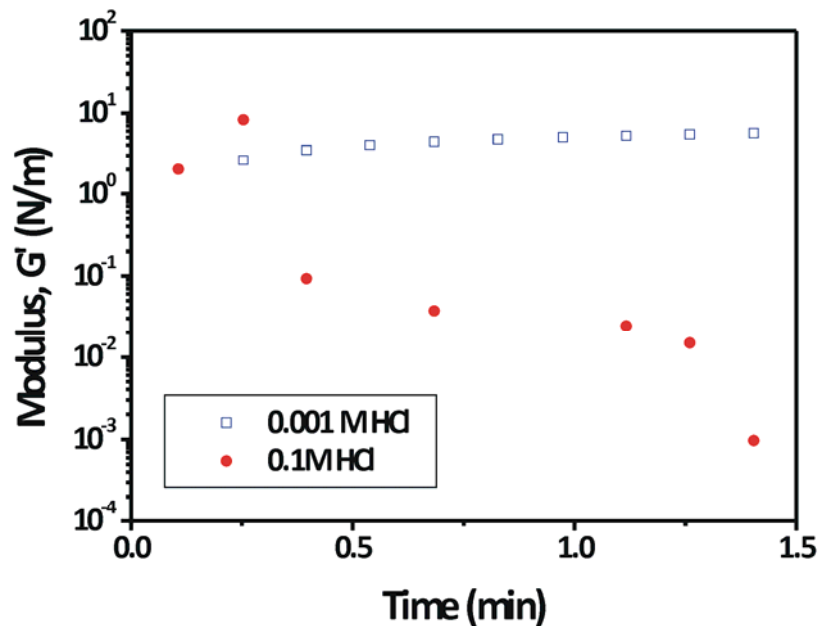


**Figure 7.3.** Removal of the oxide skin using acid causes the modulus of the skin to decrease significantly with time. The mechanical modulus in 0.1 M HCl solution drops down continuously over time whereas the metal in 0.001M HCl solution shows similar value of the metal in water. We suspect that the skin is thinning with time in 0.1 M HCl solution as indicated by the continuous decrease in elastic modulus.

The Pourbaix diagram suggests that the oxide skin of EGaIn can be removed by acid (with  $\text{pH} < 3$ )<sup>[17]</sup>. As soon as the acid removes the oxide skin, the metal beads up to be a spherical shape due to its high surface energy. We hypothesized that the presence of acid would lower the modulus and eventually remove the skin entirely so that the elastic effects would disappear. We repeated the time sweep of the metal in two different concentrations of HCl solutions (0.1 M and 0.001 M) to investigate the kinetics of dissolution process of the oxide skin. **Figure 7.3** shows that the elastic modulus decreases with time in the 0.1 M HCl ( $\text{pH} = 1$ ) solution whereas the modulus of metal in the 0.001 M HCl ( $\text{pH} = 3$ ) solution does not change, showing similar value with what in DI water. We also observed the stability of spread metal on a glass slide after dropping the two concentrations of the acid solutions on the metal. The metal covered with 0.1 M HCl solution beads up suddenly after a few seconds while the metal with 0.001 M HCl solution shows no change in shape. It implies that the  $\text{pH}$  of the 0.001M acid solution is not low enough to remove the oxide skin which is in a good agreement with Pourbaix diagram.<sup>[17]</sup> This result is expected and proved to be consistent with reported observations of the instability of EGaIn in the presence of acid in microfluidic channels<sup>[2]</sup>.

## 7.5 Conclusion

We demonstrated methods to decrease the modulus and yield properties of the oxide skin. In an aqueous environment, the elastic modulus of the metal decreases by an order of magnitude and the yield stress decreases by a factor of two; this result provides a simple approach to reduce the yield stress of the metal. The modulus increases upon drying, but the yield stress

returns to the original value measured in air. Tuning the yield properties of the metal is important for defining the stability of the metal in microscale. Thus such findings can be applied to control the physical behavior of the liquid metal in microchannels.

## 7.6 References

- [1] M. J. Regan, P. S. Pershan, O. M. Magnussen, B. M. Ocko, M. Deutsch, L. E. Berman, *Phys. Rev. B* 1997, *55*, 15874.
- [2] M. D. Dickey, R. C. Chiechi, R. J. Larsen, E. A. Weiss, D. A. Weitz, G. M. Whitesides, *Advanced Functional Materials* 2008, *18*, 1097.
- [3] D. Zrnica, D. S. Swatik, *J. Less-Common Metals* 1969, *18*, 67.
- [4] R. C. Chiechi, E. A. Weiss, M. D. Dickey, G. M. Whitesides, *Angew. Chem., Int. Ed.* 2008, *47*, 142.
- [5] S. Cheng, A. Rydberg, K. Hjort, Z. Wu, *Appl. Phys. Lett.* 2009, *94*, 144103.
- [6] M. Kubo, X. Li, C. Kim, M. Hashimoto, B. J. Wiley, D. Ham, G. M. Whitesides, *Advanced Materials* 2010, *22*, 2749.
- [7] J.-H. So, J. Thelen, A. Qusba, G. J. Hayes, G. Lazzi, M. D. Dickey, *Advanced Functional Materials* 2009, *19*, 3632.
- [8] M. R. Khan, G. J. Hayes, J. H. So, G. Lazzi, M. D. Dickey, *Appl. Phys. Lett.* 2011, *99*.
- [9] J.-H. So, M. D. Dickey, *Lab Chip* 2011, *11*, 905.
- [10] H.-J. Kim, C. Son, B. Ziaie, *Appl. Phys. Lett.* 2008, *92*, 011904/1.
- [11] M. M. Thuo, W. F. Reus, C. A. Nijhuis, J. R. Barber, C. Kim, M. D. Schulz, G. M. Whitesides, *J. Am. Chem. Soc.* 2011, *133*, 2962.
- [12] R. J. Larsen, M. D. Dickey, G. M. Whitesides, D. A. Weitz, *Journal of Rheology* 2009, *53*, 1305.
- [13] J. N. Koster, *Cryst. Res. Technol.* 1999, *34*, 1129.
- [14] C. W. Macosko, *Rheology: principles, measurements, and applications*, Wiley-VCH, New York 1994.
- [15] T. G. Mezger, *The Rheology Handbook*, Vincentz Network GmbH & Co KG, Hannover 2006.
- [16] N. Horasawa, S. Takahashi, M. Marek, *Journal of Dental Research* 1997, *76*, 1481.

[17] M. Pourbaix, *Atlas of Electrochemical Equilibria in Aqueous Solutions - Gallium*, Vol. 16.1, National Association of Corrosion Engineers, Houston, Texas, USA 1974.

## **Chapter 8. Summary and Outlook**

## 8.1 Summary

Injecting low melting point metals, such as eutectic gallium indium (EGaIn), into microchannels offers a simple way to fabricate metallic components including electrodes, reconfigurable and reversibly deformable antennas, and soft electronics. A thin oxide skin that forms rapidly and spontaneously on the surface of the metal stabilizes mechanically the otherwise low viscosity, high surface tension fluid within the channel. We fabricated dipole and patch antennas by injecting the liquid metal into PDMS elastomeric microchannels. The fluidic dipole radiates with  $\sim 90\%$  efficiency over a broad frequency range, which is equivalent to the expected efficiency for a similar dipole with solid metallic elements such as copper. Periodic posts embedded in microstrip patch antennas allow the liquid metal fill uniformly the volume for conducting elements that have high aspect ratio, and keep the PDMS channels from collapsing. The shape and thus, the function of the dipole and patch antennas, are mechanically tunable.

Using similar principles, we fabricated highly stretchable elastomeric fibers with metallic conductivity. The core-shell structure resembles a conventional wire with metal in the core and polymer (SEBS) on the outside, but the present work is distinguished by the unique electrical and mechanical properties enabled by the liquid metal. The fiber has EGaIn in its core and the ability of the metal to flow during deformation of the SEBS elastomeric shell ensures electrical continuity. Because the conductive element of the wire is a fluid, the mechanical properties are defined by the SEBS gel, which shows tremendous stretchability (as high as 900-1000 % strain at break). We demonstrated the stretchable conductive wires as a charger for an iPod and earphones to play music while applying a strain.

We utilized the electrical properties of the oxide skin of the liquid metal, which can be controlled in thickness by applying electric bias, to realize a new class of memristors based entirely on soft and liquid-based matter. The devices consist of liquid metal electrodes interfaced with water-based gel doped with polyelectrolytes. They memorize the last state of bias polarization on the basis of the asymmetric conductance of the hydrogel-oxide-liquid metal stack. In addition to operating in conditions that are considered harsh toward conventional electronics (e.g., water, base, acid), such devices may find application in the interface between circuits and live tissue, soft robotics, and neuromorphic systems.

We also described the fabrication and characterization of microelectrodes that are inherently aligned with microfluidic channels and in direct contact with the fluid in the channels. The distinguishing characteristic of this work is that the electrodes are inherently aligned and in direct contact with the fluid in the microfluidic channel, which is useful for a number of applications such as electrophoresis. Moreover, the injected electrodes vertically span the sidewalls of the channel, which allows for the application of uniform electric field lines throughout the height of the channel. The electrodes are mechanically stable over operating conditions commonly used in microfluidic applications and are formed in a single processing step, which represents a tremendous improvement over conventional fab-based methods. As a demonstration of their utility, the fluidic electrodes are used for electrohydrodynamic mixing, which requires extremely high electric fields.

Interfacial tension limits the ability to pattern liquids into arbitrary shapes both in and out of plane. However, we show it is possible to print a low viscosity liquid metal at room temperature into a variety of stable free-standing 3D microstructures. The oxide skin that

forms rapidly on the surface of EGaIn stabilizes the microstructures despite the low viscosity and large surface energy of the liquid. We measured the tensile strength of the wires which showed a good agreement with the mechanical strength of the oxide skin. We also demonstrated the feasibility of the microstructures to form stretchable wire bonds where the fluidic properties of the metal facilitate deformation without losing electrical continuity.

The oxide skin governs the electrical, mechanical, and chemical properties of the surface of the metal. Thus, understanding and controlling the oxide skin is essential for applications described in Chapter 2 to 6 as well as new possibilities. We measured the mechanical properties of the liquid metal in different chemical environments (i.e., air, water and acid) and observed that the modulus and the yield stress of the oxide skin are greatly affected by the environments showing more than two orders of magnitude of changes.

## **8.2 Future Outlook**

This dissertation describes several electronic and microfluidic applications of eutectic gallium indium and a novel technique to pattern the liquid metal by utilizing its mechanical and electrical properties that are mainly attributed from the thin layer of surface oxide. We believe that the conclusions reached in this thesis will extend to other gallium-based alloys. A number of emerging applications that use these metals in addition to those presented here rely on a dynamic system where both of the liquid metal and its solid oxide skin play a role, yet few studies have been carried out to fully elucidate the combined mechanical and rheological properties of the system. Thus, the next studies could focus on understanding fundamentally the surface and interfacial properties of the liquid metal and its oxide skin

which is important for manipulating, modifying, and tuning it to form soft, flexible and functional electronic, microscale components.

In many electronic applications of the liquid metal including those presented in this dissertation, the liquid metal has been injected into microchannels. The liquid metal forms a thin oxide skin in the presence of oxygen. It is unclear, however, if the skin exists at the interface between the metal and an oxygen impermeable substrate of a microchannel. During the filling process, the leading interface of the liquid metal is in contact with air and should therefore be covered with an oxide skin. As this plug of metal is pushed through the channel, it is unclear whether the skin “slips or if it sticks to the walls and continuously regenerates itself as the leading oxide skin is “pulled” onto the channel walls. Clarifying this filling mechanism will help prove if microfluidics can be used to form metallic contacts with surfaces under ambient conditions. The ability to form metallic contacts at room temperature is important for electrically addressing “soft” materials. We can further study the importance of surface chemistry, wetting property and roughness on the morphology and composition of the interface.

The rheological studies on the liquid metal could offer a new way to analyze the tunable mechanical properties of the liquid metal. We described certain chemical environment (i.e., water and acid) weaken the mechanical strength of the oxide skin. It is also possible to strengthen the oxide skin by coating the metal with different materials such as metals, polymers and surfactants. The resulting structure is effectively a free-standing thin-film that is supported by a low-viscosity liquid. Thus it can be applied to study kinetics and mechanics of surface adhesion of molecules, for example, self assembled monolayers

(SAMs). It is possible to examine the morphology of the surface film using scanning electron microscopy (SEM) before and after deposition and characterize the composition of the skin by spectroscopy (e.g., Energy Dispersive X-Ray Spectroscopy (EDS), X-ray Photoelectron Spectroscopy (XPS), and/or Auger Spectroscopy). Also, the changes in the mechanical properties can be characterized by using the rheometer described in Chapter 7.

Anodization offers another possible way to tune the mechanical properties of oxide skin by controlling its thickness. As shown in Chapter 4, the oxide skin can be oxidized further or reduced depending on the applied bias and/or the pH of surrounding solution. Combined with rheological studies on the liquid metal, anodization process could be analyzed qualitatively and quantitatively. For example, we could measure the mechanical modulus of the skin with time while applying the oxidative potential and calculate the relative amount of grown oxide skin as a function of duration and strength of the applied bias. Repeating oxidizing and reducing biases (i.e., AC) would provide information on reducing process and any hysteresis. The findings from these experiments could be applied in microfluidic and electric devices by controlling the critical pressure to flow the liquid metal and enable new functionalities.